

UC Berkeley

UC Berkeley Electronic Theses and Dissertations

Title

A Study on Formation and Thermal Stability of Nano-sized Oxide Clusters in Mechanically Alloyed NiAl for High Temperature Applications

Permalink

<https://escholarship.org/uc/item/9g42k9js>

Author

KIM, YONG-DEOG

Publication Date

2012

Peer reviewed|Thesis/dissertation

**A Study on Formation and Thermal Stability of Nano-sized Oxide Clusters
in Mechanically Alloyed NiAl for High Temperature Applications**

by

Yong-Deog Kim

A dissertation submitted in partial satisfaction of the

requirements for the degree of

Doctor of Philosophy

in

Engineering – Nuclear Engineering

in the

Graduate Division

of the

University of California, Berkeley

Committee in charge:

Professor Brian D. Wirth, Chair
Professor Joonhong Ahn
Professor Ka-Ngo Leung
Professor Ronald Gronsky

Spring 2012

Abstract

A Study on Formation and Thermal Stability of Nano-sized Oxide Clusters in Mechanically Alloyed NiAl for High Temperature Applications

by

Yong-Deog Kim

Doctor of Philosophy in Engineering – Nuclear Engineering

University of California, Berkeley

Professor Brian D. Wirth, Chair

The intermetallic compound, B2 NiAl, is a promising material for high temperature structural applications such as in aviation jet engines or gas turbines, provided that its high temperature mechanical properties can be improved. Although extensive efforts over the last several decades have been devoted toward enhancing ductility through alloying design and reducing impurities, as well as improving high temperature creep strength through precipitation and dispersion strengthening, these efforts have relied on traditional approaches, a combination of large grain size to limit diffusional creep and precipitation/dispersion (50 ~ 100 nm size) strengthening to limit dislocation creep, for high temperature strengthening. While traditional approaches have shown a good improvement from a relatively high temperature strengthening point of view, the size and number density of dispersoids were not able to provide sufficient strength in the high temperature creep regime. Furthermore, details of the interaction mechanism between dislocations and dispersoids are not yet well understood.

This study focuses on designing and developing advanced oxide dispersion strengthened (ODS) NiAl intermetallics with improved high temperature creep strength by incorporating a high number density ($\sim 10^{24} \text{ m}^{-3}$) of very thermally stable Y-Ti-O nano-clusters, akin to those recently observed to improve creep strength and radiation resistance in nano-structured ferritic alloys.

Advanced ODS NiAl alloys have been produced by mechanical alloying of pre-alloyed Ni-50at%Al with Y_2O_3 and Ti elemental powders. The milled powders were subsequently consolidated by spark plasma sintering, with the objective of producing very high number densities of nano-sized Y-Ti-O precipitates, along with fine grain size. Advanced experimental characterization techniques, combined with microhardness strength measurement, were used to investigate the material microstructure and strength following processing and to evaluate the thermal stability during an extensive matrix of long-term thermal annealing. In particular, the size, number density and composition of nano-clusters were assessed.

While improvements in strength were obtained in the advanced NiAl ODS alloys, and the higher strength persisted through thermal annealing for 100 hrs at 1723K, characterization revealed the presence of Al in the oxide precipitate phases. The Al incorporation is believed detrimental to the formation of a high density of thermally stable Y-Ti-O nanoscale precipitates.

To Jihyun and Yuna

Contents

List of Figures	iv
List of Tables	vii
1 Introduction	1
1.1 Potential high-temperature intermetallic alloy systems	3
1.2 Previous work	5
1.3 Research objectives and approach	6
1.4 Dissertation Overview	7
2 Materials Processing	9
2.1 Mechanical alloying	9
2.1.1 Mechanical alloying of NiAl alloys	10
2.1.2 Mechanical alloying of Fe-Cr based 14YWT	11
2.1.3 Nitrogen contamination problem during ball milling	14
2.1.4 Modification of milling procedure for N contamination	16
2.1.4.1 Modification for NiAl alloys	16
2.1.4.2 Modification for Fe-Cr based 14YWT	16
2.2 Spark Plasma Sintering (SPS) for NiAl alloys	20
2.2.1 Consolidation of ODS NiAl alloys powder by SPS	21
2.3 Hot Extrusion and Hot Isostatic Pressing (HIP) for Fe-Cr based 14YWT	22
3 Experimental Characterization Techniques	23
3.1 X-ray diffractometry	23
3.2 Scanning electron microscopy and Energy dispersive X-ray spectroscopy	25
3.3 Transmission electron microscopy	25
3.4 Atom probe tomography	26
3.5 Microhardness	28
3.6 Chemistry analysis	28
4 Results of Microstructural Characterization in As-milled and Consolidated Conditions	30
4.1 14YWT alloys	30
4.1.1 Results of ball milling	31
4.1.2 Discussion	34

4.2	NiAl alloys	37
4.2.1	As-milled powder characterization	37
4.2.1.1	X-ray diffractometry	37
4.2.1.2	Scanning electron microscopy	37
4.2.1.3	Energy dispersive X-ray spectroscopy	42
4.2.1.4	Discussion	42
4.2.2	Consolidated specimen characterization	45
4.2.2.1	Density	45
4.2.2.2	Microhardness	45
4.2.2.3	Energy dispersive X-ray spectroscopy	48
4.2.2.4	Transmission electron microscopy	50
4.2.2.5	Atom probe tomography	55
4.2.2.6	The relationship between the microhardness and microstructure	55
4.3	Summary and discussion	58
5	Thermal Stability of Nano Oxide Precipitates and Grain Growth Kinetics	60
5.1	Thermal annealing	60
5.2	Microstructure evolution during thermal annealing	61
5.3	Variation of microhardness with annealing conditions	71
5.4	Orowan strengthening effect on NiAl-Y ₂ O ₃ -Ti alloy	76
5.5	Hall-Petch strengthening effect on NiAl-Y ₂ O ₃ -Ti alloy	80
5.6	Discussion strengthening mechanisms on NiAl-Y ₂ O ₃ -Ti alloy	82
5.7	Grain growth kinetics	85
5.8	Summary and discussion	85
6	Conclusions and Future Work	90
6.1	Conclusions	90
6.1.1	Materials processing	90
6.1.2	Experimental characterization	90
6.1.3	Thermal stability and grain growth kinetics for ODS NiAl	91
6.2	Future work	91
	Bibliography	93

List of Figures

1-1. Elemental Cr, Y, Ti, and O maps in 12YWT obtained by atom probe tomography as reproduced from Ref [39]	3
1-2. The Ni-Al binary phase diagram as reproduced from Ref [59].....	4
1-3. Dislocation and particle interaction as reproduced from Ref [12]	5
1-4. Schematic diagram of research approach involving alloy development, characterization, and atomic simulation	7
2-1. Simoloyer CM-01 high energy attrition mill.....	10
2-2. Initial mechanical alloying procedure	10
2-3. Milling speed and process temperature variations during the ball milling	12
2-4. Preliminary experimental attritor milling procedure.....	13
2-5. O and N content in L2311 milled powder as a function of milling time (hr)...	14
2-6. Standard atom maps of 40hr as-milled L2311 powder showing TiN and WN atoms	15
2-7. Powder characterization result of 40hr as-milled L2314 (a) SEM morphology and (b) EDS scan	15
2-8. Modified mechanical alloying procedure	16
2-9. Modified experimental attritor milling procedure.....	17
2-10. (a) SEM morphology and (b) EDS scan result of 40hr as-milled L2314 powder	18
2-11. X-ray diffraction peak for L2314 powder, before and after milling for 40 hrs	19
2-12. Basic mechanism of SPS as reproduced from Ref [86]	20
2-13. Schematic configuration of SPS facility as reproduced from Ref [86]	21
2-14. Heating profile during the SPS.....	21
3-1. Full Width at Half Maximum (FWHM) determination from XRD peak (schematic) as reproduced from Ref [92]	24
3-2. Schematic diagram of a 3D atom probe as reproduced from Ref [106].....	27
3-3. Typical APT specimen of the NiAl-Y ₂ O ₃ -Ti alloy (FIB milled).....	27
3-4. Typical Vickers hardness indentation image of the NiAl alloy	28
4-1. EPMA analysis of ball milled powder (a) after 20hr of milling (b) after 40hr of milling	31
4-2. Typical SEM images of 14YWT (L2311) powder (a) after 20 hr milling (b) after 40hr milling	32

4-3.	X-ray elemental (Fe, Cr, Ti, Y, W) mapping of the 14YWT powder after 40hr ball milling	32
4-4.	EPMA analysis showing the Y and Ti distribution in hot extruded 14YWT (L2311) alloy that were prepared from (a) 5 h and (b) 40 h ball milled powder	33
4-5.	Typical conventional TEM images of 40 hr milled and HIPed at 1150°C at 200 MPa	33
4-6.	20 nm thick Atom maps with Cr ions and Y-Ti-O isoconcentration surfaces for	34
4-7.	Vickers microhardness, H_v , versus O content as reproduced from Ref [107] ..	35
4-8.	The alloy H_v versus the square root of the NCs volume fraction (\sqrt{f}) as reproduced from Ref [107]	36
4-9.	XRD patterns of the mechanically alloyed powders as a function of milling time (a) NiAl (b) NiAl-1wt%Y ₂ O ₃ (c) NiAl-1wt%Y ₂ O ₃ -1wt%Ti	38
4-10.	Calculated grain size and strain of the mechanically alloyed powders as a function of milling time (3 alloys averaged)	39
4-11.	Calculated dislocation density of the mechanically alloyed powders as a function of milling time (3 alloys averaged)	40
4-12.	SEM micrographs of NiAl-1wt.%Y ₂ O ₃ -1wt.%Ti powder as a function of milling time;	41
4-13.	X-ray elemental (Ni, Al, Y, O, Ti) mapping of the NiAl-1wt%Y ₂ O ₃ -1wt%Ti powder,	43
4-14.	X-ray elemental (Ni, Al, Y, O, Ti) mapping from the identified region in Figure 4-13(b).	44
4-15.	Relative density measurement results of the SPSed specimens as a function of the milling time	46
4-16.	Vickers microhardness test results of the consolidated NiAl specimens as a function of milling time	47
4-17.	X-ray elemental (Ni, Al, Y, O, Ti) mapping of the consolidated NiAl-1wt%Y ₂ O ₃ -1wt%Ti specimen, (a) before milling (b) 5 hr milled (c) 10 hr milled	49
4-18.	TEM micrographs of the as-consolidated NiAl alloys, (a) NiAl (b) NiAl-1wt%Y ₂ O ₃ (c) NiAl-1wt%Y ₂ O ₃ -1wt%Ti	51
4-19.	TEM bright image and compositions of the precipitates from the as-consolidated NiAl-1wt%Y ₂ O ₃ alloy (a)-(c); EDS spectra from the precipitates marked by the arrows (d)	52
4-20.	TEM bright image and compositions of the precipitates from the as-consolidated NiAl-1wt%Y ₂ O ₃ -1wt%Ti alloy (a)-(c); EDS spectra from the precipitates marked by the arrows (d)	53
4-21.	TEM image of the various precipitates from the as-consolidated NiAl-1wt%Y ₂ O ₃ -1wt%Ti alloy (a); accumulated percent of compositions in the precipitates marked by the numbers (b)	54
4-22.	Atom probe tomography images of Al, Ni, Fe, Y, Ti, and O that were observed in the as-consolidated NiAl-1wt%Y ₂ O ₃ -1wt%Ti alloy	56
5-1.	Microstructure evolution in (a, b) NiAl and (c, d) NiAl-Y ₂ O ₃ -Ti, as-	

consolidated, after 20 hr at 1626K, respectively, showing grains and oxide particle	64
5-2. Microstructure evolution in NiAl-Y ₂ O ₃ -Ti (a) after 20 hr (b) after 200 hr at 1433K	65
5-3. Microstructure evolution in NiAl-Y ₂ O ₃ -Ti after 100 hr, 200 hr, and 500 hr at 1626K (a)-(c); after 100 hr at 1723K (d).....	66
5-4. A plot between grain size and particle size in NiAl-Y ₂ O ₃ -Ti.....	67
5-5. Evolution of: (a) grain size and (b) particle size in NiAl-Y ₂ O ₃ -Ti as a function of annealing time at 1626K	68
5-6. TEM image of the precipitates from NiAl-Y ₂ O ₃ -Ti alloy after 20 hr at 1433K (a); accumulated percent of compositions in the precipitates marked by the numbers (b).....	69
5-7. Elements (O, Y, Ti, Fe, Al) mapping of the NiAl-Y ₂ O ₃ -Ti alloy after 20 hr at 1433K by STEM EELS characterization	70
5-8. Evolution of microhardness with annealing time at 1433K	72
5-9. Evolution of microhardness with annealing time at 1626K	73
5-10. Evolution of microhardness with annealing time at 1723K	74
5-11. Evolution of: microhardness as a function of (a) grain size and (b) particle size in NiAl-Y ₂ O ₃ -Ti at 1626K.....	75
5-12. Evolution of $\sqrt{n}D$ and microhardness in NiAl-Y ₂ O ₃ -Ti as a function of annealing time at 1626K.....	78
5-13. Evolution of microhardness as a function of $\sqrt{n}D$ in NiAl-Y ₂ O ₃ -Ti at 1626K ..	79
5-14. Variation in microhardness with $d^{-1/2}$ for NiAl-Y ₂ O ₃ -Ti and NiAl alloys. Source: Ref [81, 116].....	81
5-15. Evolution of microhardness, Orowan strength, and Hall-Petch strength as a function of annealing time in NiAl-Y ₂ O ₃ -Ti annealed at 1626K	84
5-16. Schematic representation of grain growth by atomic diffusion as reproduced from Ref [118]	87
5-17. The grain size evolutions of the ODS NiAl alloys as a function of annealing time at 1433 and 1626K	88
5-18. Semi-logarithmic plot of $(d^2-d_0^2)$ versus $1/T$ for NiAl-Y ₂ O ₃ -Ti.....	89

List of Tables

2-1. Compositions of initial batch heats of 14YWT powders (wt% bal Fe)	11
2-2. Compositional analysis results of the NiAl-1wt%Y ₂ O ₃ -1wt%Ti after ball milling for 15 hrs	14
2-3. Compositional analysis results of the NiAl-1wt%Y ₂ O ₃ -1wt%Ti after ball milling for 15 hrs	16
2-4. Compositions of 14YWT (L2314) after milling for 40 hr	18
4-1. Summary of the characteristics measured in the NiAl alloys	51
4-2. The summary of strengthening components and the microhardness value assessment	58
5-1. Temperatures and times for annealing study	61
5-2. Evolution of average particle size and grain size as a function of annealing temperature and time	63
5-3. Evolution of average particle size, particle number density, \sqrt{nD} , and microhardness value during the annealing	77
5-4. The details of strengthening components and the microhardness value assessment for NiAl alloys	84

Acknowledgments

I'd like to express my deep gratitude to all who contribute and support my doctoral dissertation and graduate student life in University of California at Berkeley.

First of all, it was a great privilege to have worked under the supervision of my advisor, Professor Brian Wirth. I could accomplish my research work and I was granted a PhD degree from his insightful advice, persistent encouragement, and constant support. I'd like to express my earnest respect to his academic enthusiasm and passion.

I also want to pay my sincere respect to Professors at UC Berkeley, Ronald Gronsky, Joonhong Ahn, and Ka-Ngo Leung, who had not only given precious lectures to me during my graduate coursework but also offered great advice during my qualifying exam. Special thanks to Professor Zuhair Munir at UC Davis for letting me have a chance to use a Spark Plasma Sintering facility for my research. I also specially give my appreciation to Dr. Jeremy Busby who has hosted and supported me to work at Oak Ridge National Laboratory (ORNL), Dr. Lizhen Tan who has collaborated in TEM work at ORNL, and Nick Cunningham who has collaborated on 14YWT alloy development at UCSB.

In addition, I would like to thank my current and past colleagues in my group: Hyon-Jee Lee, Donghua Xu, Kurt Terrani, Thibault Faney, Karl Hammond, Najeb Abdul-Jabbar, Nathan Capps, Xunxiang Hu, Niklas Juslin, Aaron Kohnert, Faiza Sefta, Gui-Yang Huang, Tuan Hoang, Aude Simar, and all others.

I would like to thank to the KEPCO and KHNP Scholarship for its generous support during my PhD study.

Finally, I take this opportunity to express my deepest love to my wife, Jihyun, for her consistent support, dedication, and encouragement and my dear daughter, Yuna, for giving me feeling of precious love and happiness in family life. I'd like to express my sincerest gratitude to my parents and parents-in-law, for their endless love, support, and encouragement throughout my life. Thanks to all.

Chapter 1

Introduction

The invention and discovery of new high temperature structural materials used in aviation jet engines, gas turbines, pressure vessel, and power plant pipe materials is one of the truly challenging tasks in materials science and engineering. During the last fifty years, there have been remarkable achievements in materials development for high temperature applications [1-7]. As a few examples, turbine inlet temperature in Ni based jet engines have increased nearly 410°C in 50 years [7] from 700°C, and super heater steam temperatures in Ferritic steel based super critical power plants have increased from 370 to 650°C in 40 years [4, 5]. Those thermal performance improvements have derived from alloy optimization and particle strengthening, in addition to applications of new oxide thermal barrier coatings [6, 8]. But the continual push towards improved performance and thermodynamic system efficiency in both jet engines and power plants requires further revolutionary improvements in high temperature materials. For example, current Ni based superalloys have the ability to operate for thousands of hours under loads on the order of 140 MPa at temperatures of 1100°C [3], which is about 85% of their melting point, but have already reached the “Uppermost Limit.” Therefore, completely new and different classes of high temperature materials must be developed to meet the ever-increasing temperature demands for improved performance and thermodynamic system efficiencies.

Traditional approaches for improving high temperature creep resistance have relied on a combination of large grain size to limit diffusional creep, and solid solution and dispersion or particle strengthening to limit dislocation creep [9-12]. For high temperature strengthening, dispersion strengthening is a classical mechanism, which relies on the dispersion of nearly insoluble particles which are non-shearable and impede plastic deformation [13]. Dispersion strengthened, or more appropriately, oxide dispersion strengthened (ODS) alloys can achieve good strengths at high temperatures, approaching 90% of the melting point, in polycrystalline metallic and intermetallic alloys [14, 15]. Ytria (Y_2O_3), garnet ($\text{Y}_3\text{Al}_5\text{O}_{12}$ or YAG), Zirconia (ZrO_2), titania (TiO_2), or alumina (Al_2O_3) are typically used as ODS particles in the size range of 50 ± 25 nm and volume fractions of about 2% [16-20]. These dispersoids, which are incoherent with the matrix, are relatively stable up to high homologous temperature and impede dislocation motion through an Orowan looping mechanism at low temperatures. At higher

temperatures, creep behavior is much more complex but believed to depend on the detachment mechanism of dislocations that initially experience an attractive interaction to the particles [13, 14, 17, 21]. Arzt and co-workers have shown promising high temperature creep behavior in ODS strengthened B2 intermetallic NiAl through mechanical alloying with Y_2O_3 [15, 21-23], although the dislocation interaction and detachment mechanisms are not well understood.

An alternative and complementary strategy for high temperature strengthening is the incorporation of a very high number density ($\sim 10^{24} \text{ m}^{-3}$) of highly stable, but much smaller, nanometer scale coherent transition phases, which have emerged in the recent large-effort development of nanostructured ferritic alloys (NFAs) [24-36]. NFA development initially began with the production of ODS Fe-Cr alloys for nuclear power plants in the early 1980's when the International Nickel Company (INCO) produced the alloys MA956 and MA957 [37]. These materials, first extensively researched by Ukai and co-workers at Nuclear Fuel Development Corporation in collaboration with Kobe Steel Ltd. in Japan [28], have significantly improved creep strength compared to conventional ferritic martensitic steels or ODS ferritic alloys. For example, Ukai et al. report a 650 °C biaxial creep rupture strength of about 250 MPa for an Fe-13Cr-3W-0.5Ti-0.5Y₂O₃ (nominal wt%) mechanically alloyed ferritic steel, compared to about 95 MPa for an Fe-13Cr-3W-0.5Ti ferritic steel without yttria and about 160 MPa for a more conventional ODS alloy, Fe-13Cr-3W-0.5 Y₂O₃ without Ti [24]. Later, Ukai and researchers at Kobe Steel Ltd. discovered dramatic improvements in the uniaxial and biaxial creep rupture properties at 650 °C for a mechanically alloyed and hot extruded Fe-13Cr-3W-0.5Ti-0.5Y₂O₃ ferritic alloy compared to Fe-13Cr- 3W-0.5Ti ferritic steel without yttria. Improvements in the creep rupture strength from about 150 to 400 MPa and from 95 to 250 MPa were obtained in uniaxial and biaxial testing, respectively, for the steel containing both yttria and titanium [38].

Subsequent work in Japan, the U.S. and Europe has revealed that the improved creep strength results from the formation of an ultra-high number density of Y-Ti-O nanometer sized clusters [25, 27-29, 31-33, 35, 36]. Atom probe tomography, performed at ORNL by Miller, revealed the presence of a high number density ($\sim 10^{24} \text{ m}^{-3}$) of ultra-fine Y-Ti-O nanoclusters in both 12YWT and in MA957, as shown in the atom map in Figure 1-1 [39]. Extensive studies, in particular at UCSB by Alinger and Odette [25, 32, 33, 35], have shown that the yttrium from Y₂O₃ powders dissolves during mechanical alloying and subsequently precipitates during thermal mechanical processing in the form of the Y-Ti-O nanoclusters [33, 35, 39]. Alinger and Odette further studied the thermal stability of the nanoclusters in mechanically alloyed MA957 and found remarkable high temperature stability, with very limited nanocluster growth and coarsening following annealing for 480 hours at 1200°C and 9 hours at 1400°C with an effective activation energy of $890 \pm 150 \text{ kJ/mol}$ (9.2 eV/atom) controlling coarsening [33]. The detailed factors controlling the precipitation kinetics, morphology and thermal stability of the nanoclusters in NFAs are not yet understood, nor are the detailed mechanisms of their structural evolution. However, it is likely that the strategy of employing a very high number density of Y-Ti-O nanoclusters will also strengthen advanced NiAl intermetallic and other FCC alloys for high temperature applications.

With this research motivation, the objective of this study includes both the design and development of advanced ODS NiAl alloys as well as fundamental insight into the

thermodynamics and kinetics of NC formation and thermal stability.

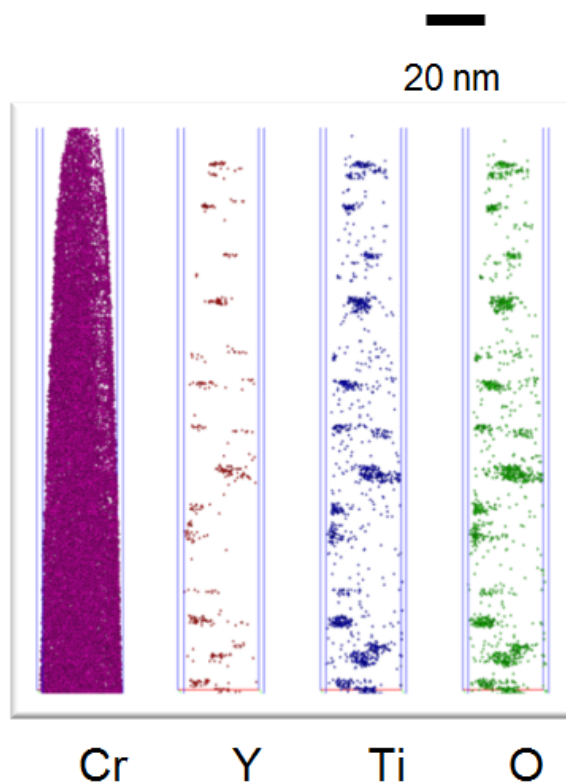


Figure 1-1. Elemental Cr, Y, Ti, and O maps in 12YWT obtained by atom probe tomography as reproduced from Ref [39]

1.1 Potential high-temperature intermetallic alloy systems

The B2 NiAl intermetallic alloy has been extensively studied as a structural material due to a combination of interesting properties, such as high mechanical strength, low density (5.95 g/cm^3), high thermal conductivity ($70 \text{ W/m}\cdot\text{K}$), excellent oxidation resistance [40-59], and high melting point ($\sim 1640^\circ\text{C}$) as shown in Figure 1-2. However, like many intermetallics, B2 NiAl is brittle at low temperatures and has inadequate high temperature strength and creep resistance. It is usually considered that significant improvements in high temperature strength and ductility at room temperature are needed before this material finds its way into practical applications [40]. The majority of recent research has focused on enhancing ductility through alloying (Cr, Ce, Mo, Ga and Zr) [60-63] and reducing impurities [64]. As well, research has studied refining grain sizes below a critical size [65], and improving high temperature strength through precipitation and dispersion strengthening [17, 23, 61, 66, 67]. As pointed out in an article by Arzt and co-workers [10], dispersion strengthening is a classic technique to improve the high temperature creep strength of metallic materials. Typically, oxide particles are dispersed

within the matrix and act as impenetrable obstacles to dislocation motion (Figure 1-3) up to temperatures approaching 90% of the melting point. The critical resolved shear stress increase (over that for a material with no dispersed barriers), $\Delta\tau_{CRSS}$, for dislocation motion in an array of dispersed particles is defined by:

$$\Delta\tau_{CRSS} = \frac{\alpha G b}{\lambda} \quad (1.1)$$

$$\frac{1}{\lambda} = \sqrt{n \cdot d} \quad (1.2),$$

where α is a barrier strength coefficient, G is the shear modulus, b is the magnitude of the Burgers vector, λ is interparticle spacing, and n is particle number density [68]. When the barriers are impenetrable, α approaches 1 and this is known as Orowan strengthening. It can be seen from Equation 1.1 that the strength increase is inversely proportional to the interparticle spacing. A decrease in λ (particle refinement for a constant volume fraction from Equation 1.2), results in an increase in the strengthening. The most common processing route to form oxide dispersion strengthened alloys involves mechanical alloying, as first developed by Benjamin [69], and provides a relatively homogeneous distribution of dispersoids.

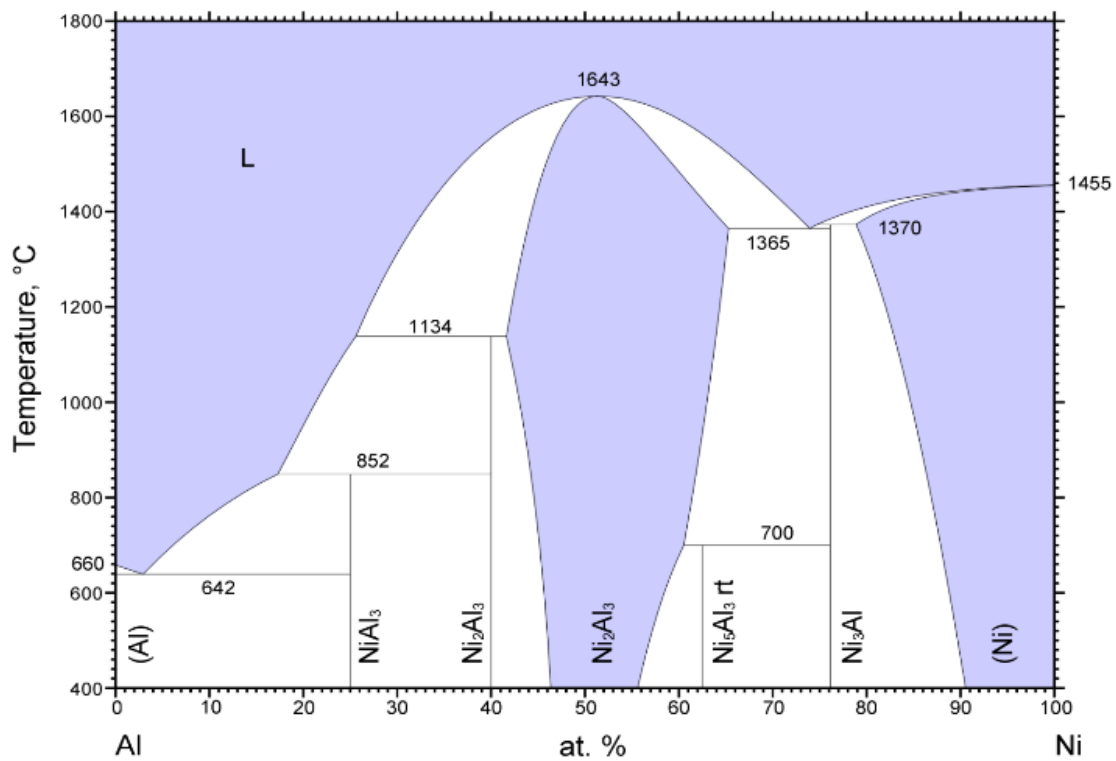


Figure 1-2. The Ni-Al binary phase diagram as reproduced from Ref [59]

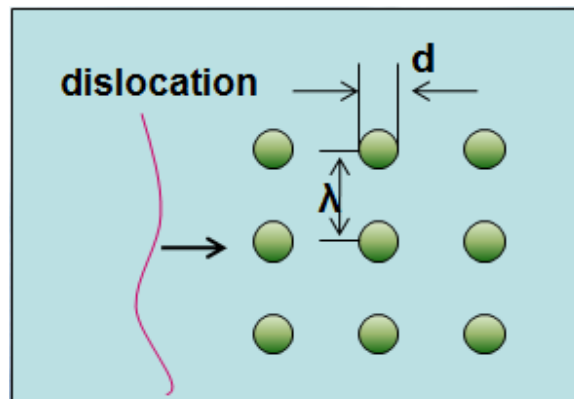


Figure 1-3. Dislocation and particle interaction as reproduced from Ref [12]

1.2 Previous work

Grahle and Arzt have performed the most extensive studies on the dispersion strengthening of B2 NiAl through mechanical alloying with Y_2O_3 followed by secondary recrystallization [15]. Other authors have investigated the use of Al_2O_3 [18, 67] and ZrO_2 [18] dispersoids. Grahle and Arzt mechanically alloyed Y_2O_3 agglomerates with Ni_2Al_3 and NiAl_3 powders to obtain a Ni-50wt%Al matrix containing about 2 volume % yttria using a centrifugal vibratory ball mill and then used hot isostatic pressing (HIP) at 1100°C and 200 MPa for consolidation to a fully dense material with a grain size of about 0.9 micron [15]. Notably, they state that, “neither TEM imaging, electron diffraction nor X-ray diffractometry revealed the presence of crystalline oxides or any other second phases in the mechanically alloyed powders. On the other hand, EDX measurements indicated that the expected quantity of yttrium was dissolved in the powder particles.” Similarly, other researchers have noticed the dissolution of alumina (Al_2O_3) during mechanical alloying with NiAl [67] and dissolution of yttria during mechanical alloying of the NFAs [25, 33] discussed in the prior section.

Grahle and Arzt observed dispersoids with a mean diameter of 2 nm in the grain interiors, with coarser dispersoids were observed at the grain boundaries following HIP [15]. Thermal annealing at temperatures of about 1500°C resulted in a bimodal grain size distribution, with a vast majority (> 90%) of coarse grains in addition to “islands” of unrecrystallized areas [15]. Dispersoids within the coarse grains were significantly larger than those within the small grains, indicating a connection between coarsening of the dispersoids and grain growth [15], also consistent with the NFAs discussed previously [25, 33]. Grahle and Arzt then searched for a thermomechanical treatment to produce the dispersoids within a desired large grain microstructure, settling on a combination of hot deformation and annealing to produce a uniform microstructure consisting of a grain size of approximately 100 microns with 50 nm diameter dispersoids [15]. Following the

thermal mechanical treatment, the dispersoids were clearly identifiable as $\text{Y}_3\text{Al}_5\text{O}_{12}$ [15] as opposed to the initial Y_2O_3 powders, with a spacing of approximately 250 nm. Arzt and Grahle [17] report the results of compression creep experiments performed on these materials in the “as-HIPed” (fine-grained ODS) and thermomechanically treated state (coarse-grained ODS), in addition to dispersoid free NiAl with a grain size between 20 and 170 microns [17]. The creep behavior of the fine-grained as-HIPed specimen significantly exceeded that of the dispersoid-free NiAl at 1200K, but became weaker by 1473K. Whereas the thermomechanically treated ODS-NiAl exhibited “exceptional creep properties up to about 1700K” [17]. The coarse-grained ODS alloy showed high creep stress values and high stress sensitivities consistent with the dislocation detachment controlled creep models developed by Arzt [10, 11] and other researchers [70, 71]. More recently, Rosler and Arzt [22] developed a creep model for detachment-controlled creep based on an attractive dislocation – dispersoid interaction followed by thermally activated dislocation detachment. However, the relaxation factor in the model for the coarse grained ODS-NiAl had to be set to an “unusually high value, which signifies a weak attractive interaction between dislocations and dispersoids” [17] and demonstrates the need for additional studies to understand dislocation – particle detachment mechanisms in dispersoid strengthened alloys. Arzt and Grahle also noted quite surprising creep properties for the fine-grained ODS alloy. While the creep strength reduced below that of the coarser-grained, dispersoid free NiAl around 1473K, they note that diffusional “Coble creep is suppressed or at least retarded by the dispersoid particles” [17] in the as-HIPed ODS alloy. The apparent creep activation energy was also much higher than anticipated [17]. Other researchers have also observed surprisingly good creep behavior in fine-grained dispersion strengthened materials [22]. As described by Arzt and Grahle [17], a possible explanation for the retardation of diffusional creep in the fine-grained ODS alloy is the pinning of grain boundary dislocations by very fine dispersed particles, thereby impeding the point defect sink/source action of grain boundaries. Arzt and Grahle further develop a model “in the form of detachment-controlled behavior of grain boundary dislocations and Coble creep” which accurately reproduces the observed creep behavior [17].

1.3 Research objectives and approach

The objective of this research is to investigate the potential for improved high temperature creep strength of B2 NiAl intermetallics by incorporating a high number density of very thermally stable Y-Ti-O nanoclusters, akin to the nanostructured ferritic alloy development strategy. Atomic simulation study has been performing in tandem with H.J.Lee at UCB. Although the atomic simulation is not described in this dissertation since it has not completed yet, the research approach involves computational modeling, including electronic structure calculations, atomistic lattice Monte Carlo simulations with Kawasaki diffusion to investigate the structure and composition of the nanoclusters in B2 NiAl alloys. Figure 1-4 shows a schematic diagram of research approach. The goal of the computational modeling is to provide insight into oxide precipitate cluster composition that could eventually provide a framework to optimize alloy compositions containing the

largest number density of nanoclusters with the highest thermal stability.

Small, approximately 100-gram batches of the B2 NiAl intermetallics alloys have been prepared by mechanical alloying and then consolidated by spark plasma sintering process. Advanced experimental characterization techniques, combined with microhardness strength measurements, have been used to investigate the material microstructure following processing and to evaluate thermal stability during extensive long-term thermal annealing. In particular, the size, number density and composition of the nanoclusters have been assessed.

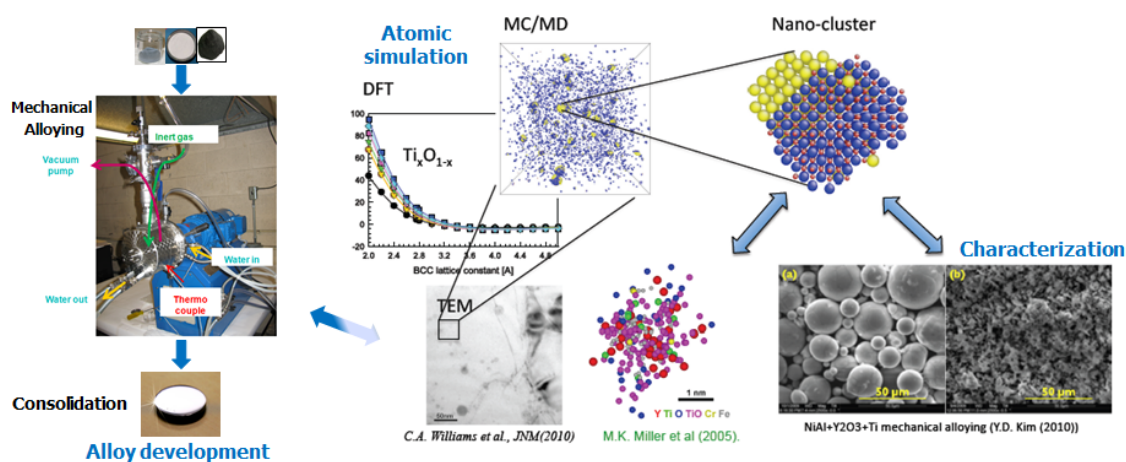


Figure 1-4. Schematic diagram of research approach involving alloy development, characterization, and atomic simulation

1.4 Dissertation Overview

The chapters of this dissertation are organized as follows:

[Chapter 2: MATERIALS PROCESSING]

This chapter describes the details of the materials processing that were performed during fabrication of ODS NiAl and ferritic 14YWT alloys. Processing improvement for reducing nitrogen contamination is also discussed in this chapter.

[Chapter 3: EXPERIMENTAL CHARACTERIZATION TECHNIQUES]

This chapter focuses on describing the details of the experimental characterization techniques used in this study. Various experimental characterization techniques, scanning electron microscopy, X-ray diffraction, energy dispersive spectroscopy, transmission electron microscopy, atom probe tomography, and electron probe micro-analyzer, are used to investigate the material microstructure. As well, Vickers microhardness measurement is used to assess the basic mechanical property of the alloys.

[Chapter 4: RESULTS OF MICROSTRUCTURAL CHARACTERIZATION IN AS-MILLED AND CONSOLIDATED CONDITIONS]

The microstructural characterization results of as-milled and as-consolidated NiAl and ferritic 14YWT alloys to assess the optimal milling time are discussed in this chapter. Besides, the effort has gone into rationalizing the relationship between the strength and the microstructure of the ODS NiAl alloys.

[Chapter 5: THERMAL STABILITY OF NANO OXIDE PRECIPITATES AND GRAIN GROWTH KINETICS]

This chapter presents a systematic study on the thermal stability of the ODS NiAl alloys following high temperature isothermal annealing. The nanosize precipitates, grain size, and microhardness of the ODS NiAl alloys have been assessed in terms of the annealing temperature and time. Finally, Orowan and Hall-Petch strengthening effects as well as grain growth kinetics for the ODS NiAl alloys have been studied.

[Chapter 6: CONCLUSIONS AND FUTURE WORK]

This chapter summarizes the important scientific findings of this research and the ongoing activities are discussed as future work.

Chapter 2

Materials Processing

Materials processing and fabrication are very important considerations in the materials development path and the number of potential alloying and processing variables is vast. The aim of this research is to combine insight gained in previous studies of ODS alloys with basic metallurgical and materials processing principles, to develop advanced ODS NiAl intermetallic and Fe-Cr based 14YWT alloys with improved high temperature strength resulting from a high number density of nm-scale precipitates with high thermal stability. In doing so, an important aspect is to establish a matrix of materials with minimized variable differences. This approach enabled the optimization of the processing to create a high number density of nm-scale clusters (NCs). In addition, fundamental insight was gained regarding the kinetics and thermodynamics behind NCs formation and evolution. This chapter describes and justifies the materials processing methods employed.

2.1 Mechanical alloying

Mechanical alloying is defined as a high energy ball milling process that can be used to produce composite materials from a blend of elemental or alloy powders [69]. The fundamental process in mechanical alloying to produce metal powders with controlled microstructures is the repeated cold-welding, fracturing, and rewelding of a mixture of powder particles under a dry, highly energetic ball charge. Mechanical alloying process, which has the advantages of precise control composition and microstructure, has been suggested to be a prospective approach to synthesize the NiAl intermetallics [14, 17, 40-42, 44-47, 50, 56, 57, 72-79] and nanostructured ferritic alloys [24-38].

The high energy milling machine, Simoloyer-CM01 was installed in the laboratory at University of California Berkeley (UCB). Figure 2-1 shows a high energy attrition mill, Simoloyer CM-01, and schematic gas and water flow.

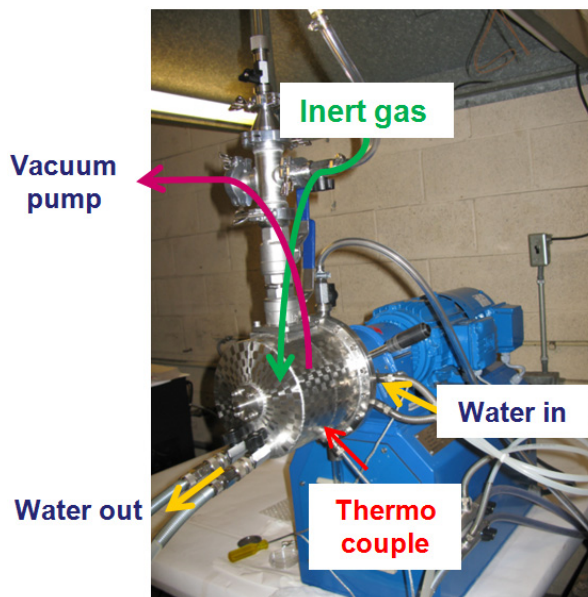


Figure 2-1. Simoloyer CM-01 high energy attrition mill

2.1.1 Mechanical alloying of NiAl alloys

In this study, ODS NiAl raw matrix materials were prepared from prealloyed, gas-atomized Ni-50at% Al powders supplied by Crucible Industries LLC. Y_2O_3 and Ti particles were added as dispersoid elements. All three powders have the same particle size of -325 mesh and purity of 99.99%. NiAl, Y_2O_3 , and Ti powders were weighed to have final compositions of NiAl, NiAl-1wt%(1.8vol%) Y_2O_3 , and NiAl-1wt%(1.9vol%) Y_2O_3 -1wt%(1.8vol%)Ti respectively. Mechanical alloying was performed for these three compositions with 100Cr6 steel ball media under Ar gas sealed environment. The milling speed was set to 1200 rpm (linear speed of 11 m/sec) and the milling times to investigate

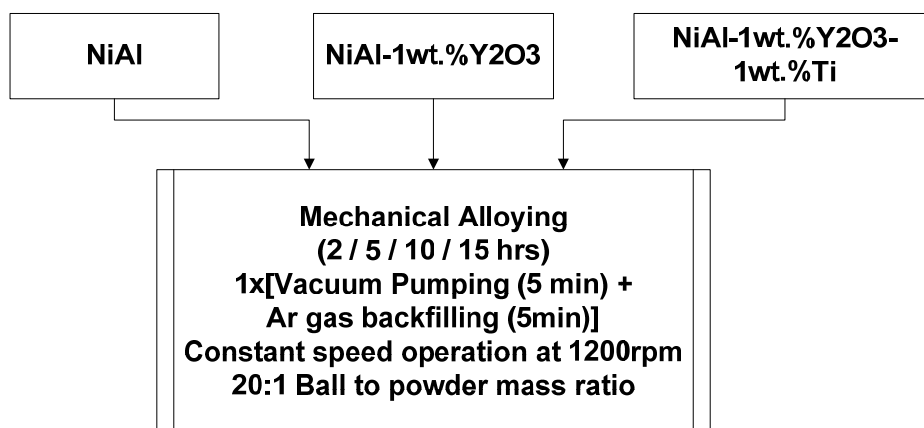


Figure 2-2. Initial mechanical alloying procedure

an optimum powder alloying condition were 2, 5, 10, and 15 hrs respectively. The weight ratio of ball media to powder was 20:1 and mechanical alloying process temperature was controlled to $\sim 20^{\circ}\text{C}$ by circulating cooling water. The test profiles such as milling speed and process temperature were recorded into log files by computer controller. The initial mechanical alloying procedure involved evacuating the milling chamber for ten minutes and then backfilling with Ar as illustrated in Figure 2-2. The mechanically alloyed NiAl alloy powders were characterized by scanning electron microscopy, X-ray diffraction, energy dispersive spectroscopy.

2.1.2 Mechanical alloying of Fe-Cr based 14YWT

The objective of this study is to develop new and improved processing paths for the production of nanostructured ferritic alloys (NFAs). NFAs have successfully demonstrated a favorable combination of outstanding high temperature strength and remarkable irradiation tolerance by trapping irradiation induced point defects and causing their eventual recombination [25, 31, 35]. These outstanding characteristics derive from the presence of an ultrahigh number density of Y-Ti-O rich nano-size clusters (NCs). 14YWT NFA is typically processed by ball milling pre-alloyed Fe-14Cr-3W-0.4Ti (nominal wt%) powder with 0.25 to 0.3wt% yttria (Y_2O_3) powder [31, 33, 35]. In particular, proper ball milling effectively dissolves the solute elements, Y, Ti, and O, which are expected to be precipitated during hot consolidation [25, 29, 33, 35, 36]. However, this advanced alloy is in an early development stage and many studies on processing parameters are still required. The focus of this work is on investigating the optimal milling time which can produce alloys with more homogeneous distributions of NCs and more uniform fine grain size distributions. The foundation of this research performed in close collaboration between UCB and University of California Santa Barbara (UCSB) is characterization of powders and alloys through each processing step: powder ball milling; following hot consolidation by hot isostatic pressing (HIP) or hot extrusion. The characterization studies of a preliminary batch of powders described here include: powder chemistry, atom probe tomography (APT), X-ray Diffraction (XRD), electron probe microanalysis (EPMA), and scanning electron microscopy (SEM) along with Energy Dispersive X-ray Spectroscopy (EDS).

Ball milling was conducted for L2311 and L2314 alloy compositions with 100g batch powder and $\phi 4$ -mm hardened 100Cr6 steel balls at ball to powder mass ratio of 10:1 by Simoloyer CM-01 attritor. The corresponding compositions of the L2311 and L2314 are summarized in Table 2-1.

Table 2-1. Compositions of initial batch heats of 14YWT powders (wt% bal Fe)

Heat	Cr	W	Ti	Y	Al	Si	O	N	C	S
L2311	14.0	3.0	0.35	0.21	0.016	0.029	0.0085	0.0015	0.002	0.003
L2314	14.0	3.0	0.35	0.21	0.016	0.029	0.0235	0.008	0.0060	0.0055

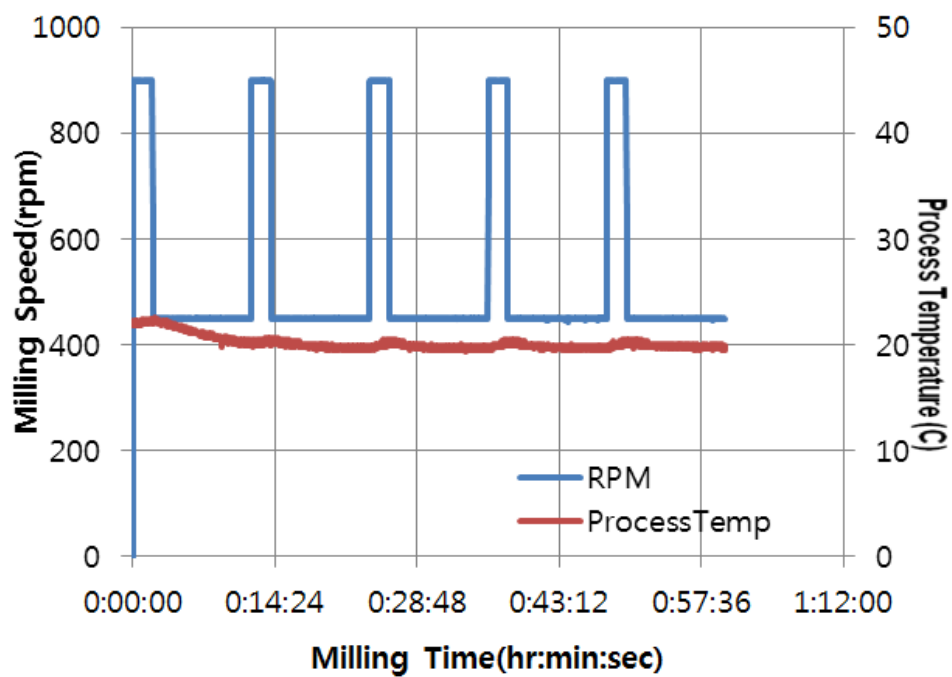


Figure 2-3. Milling speed and process temperature variations during the ball milling

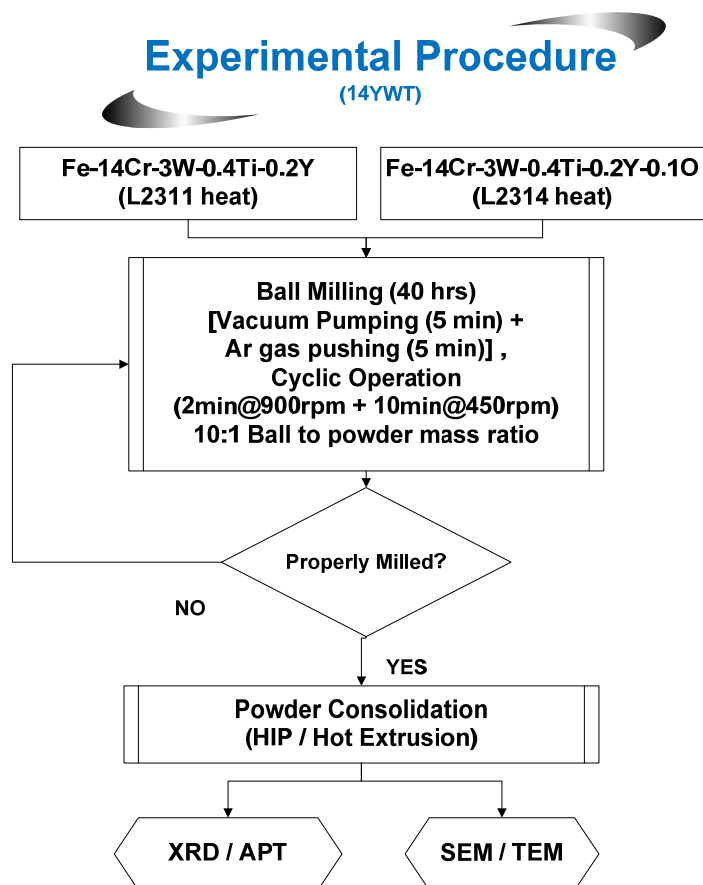


Figure 2-4. Preliminary experimental attritor milling procedure

The milling speed alternated between 900 (2 minutes) and 450 rpm (9 minutes) and the process temperature was maintained to 20°C by circulating cooling water as illustrated in Figure 2-3. The milling times were 1, 5, 20, and 40 hrs respectively. The preliminary CM-01 procedure involved evacuating the milling chamber for five minutes and then backfilling with Ar (Figure 2-4).

2.1.3 Nitrogen contamination problem during ball milling

It was found that mechanically alloyed powders picked up a significant amount of contaminant nitrogen (N) during the milling of both NiAl and 14YWT alloys. Chemical analysis of the NiAl-1wt%Y₂O₃-1wt%Ti milled powders showed an increase in N, O, and Fe contents before and after the ball milling as represented in Table 2-2. The N and O impurity pickup was very likely due to ingress of air into the milling chambers during the initial phase of ball milling studies. For example, if the milling chamber or evacuating system has a leak, it would allow air to enter and thus contaminate the Ar cover gas. This contamination problem was resolved by better sealing between chamber and evacuating system in addition to process modification, which will be discussed in the following section. Besides, it was found that more than 10% of iron from milling media was picked up during the ball milling. The effects of iron impurity on the mechanical and physical properties of NiAl have been investigated by others [80-82]. According to T. CHEN et al., the presence of Fe in NiAl intermetallic is expected to contribute to the strengthening of NiAl, due to solution strengthening [81].

Table 2-2. Compositional analysis results of the NiAl-1wt%Y₂O₃-1wt%Ti after ball milling for 15 hrs

	Before milling (wt%)	After 15hr milled (wt%)
Nitrogen	0.002	0.13
Oxygen	0.28	1.17
Iron	0.015	11.3

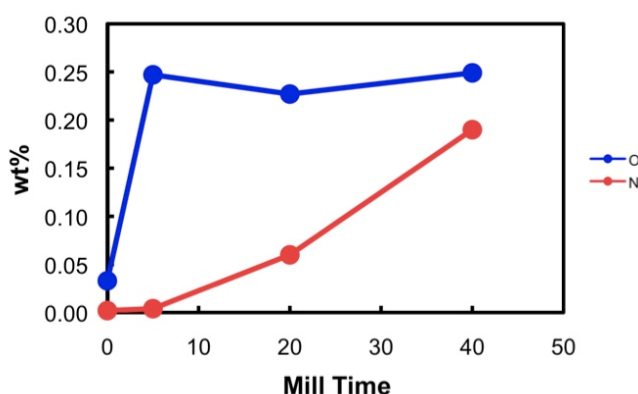


Figure 2-5. O and N content in L2311 milled powder as a function of milling time (hr)

For the 14YWT, chemical analysis of the L3211 milled powder showed an increase in O and N contents during the milling time as shown in Figure 2-5. The N systematically increased from 0.002 wt% in the milled powder to 0.190 wt% after attritor milling for 40 hrs. The O initially increases rapidly, reaching 0.25 wt% plateau after only 5 hrs.

Atom probe tomography and energy dispersive X-ray spectroscopy were also performed on the 40 hr milled L2311 powder to check the N contamination and other solute distributions. As shown in the atom probe tomography result in Figure 2-6, nitrides of either TiN or WN were found and associated with N contamination. The observed nitride precipitates had an inhomogeneous distribution. The typical morphology and EDS scanning result of 14YWT (L2314) powder after 40 hr milled is shown in Figure 2-7(a). The milled powders are flake shaped with a large range of sizes from 25 to 150 μm . Nitrogen contamination in the milled powders was also detected by EDS scanning as shown in Figure 2-7(b).

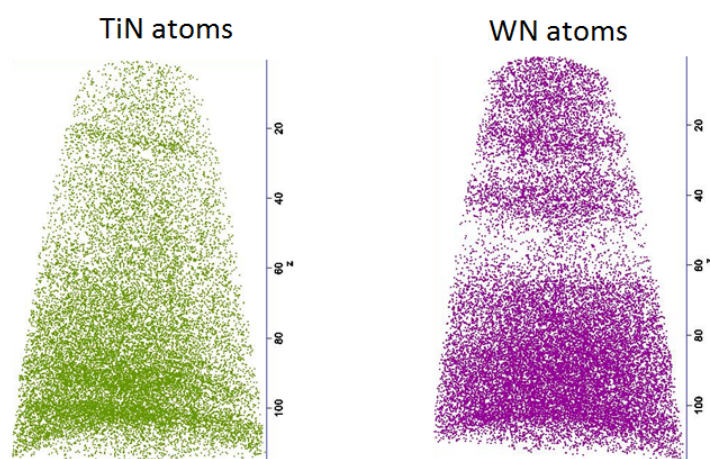


Figure 2-6. Standard atom maps of 40hr as-milled L2311 powder showing TiN and WN atoms

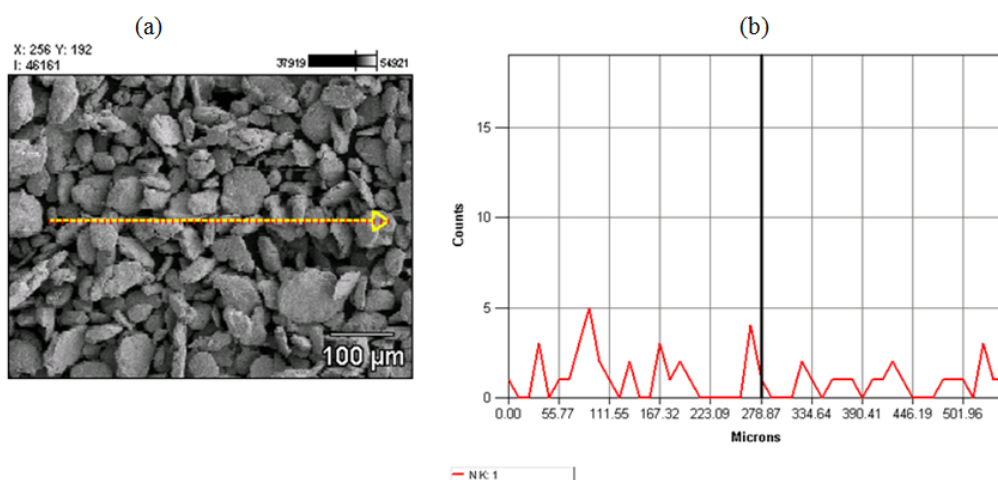


Figure 2-7. Powder characterization result of 40hr as-milled L2314 (a) SEM morphology and (b) EDS scan

2.1.4 Modification of milling procedure for N contamination

2.1.4.1 Modification for NiAl alloys

In order to reduce the N contamination discussed in Section 2.1.3, the operating procedure of the Simoloyer CM-01 was modified for milling. Cycles of repeated vacuum (10 min) and Ar purges (5 min) were performed three times while a positive pressure of Ar was maintained throughout the milling period. The milling speed alternated between 1200 (50 minutes) and 600 rpm (10 minutes). Moreover, a gate valve was installed at the vacuum pump side to prevent air leak. The modified milling procedure is illustrated in Figure 2-8. The modified attritor milling procedure for the ODS NiAl reduced N contamination approximately more than 50% that of the initial procedure and oxygen level also decreased from 1.17 to 0.34% as represented in Table 2-3.

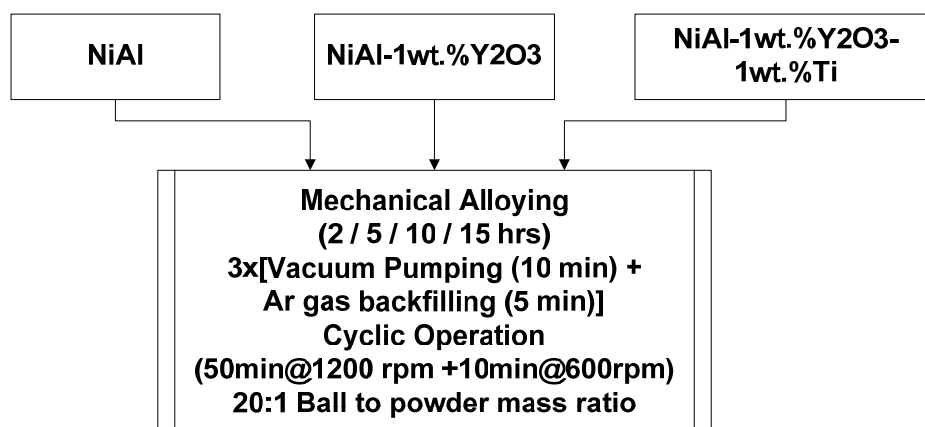


Figure 2-8. Modified mechanical alloying procedure

Table 2-3. Compositional analysis results of the NiAl-1wt%Y₂O₃-1wt%Ti after ball milling for 15 hrs

	Initial Procedure Weight (%)	Modified Procedure Weight (%)
Nitrogen	0.13	0.064
Oxygen	1.17	0.34
Iron	11.3	10.7

2.1.4.2 Modification for Fe-Cr based 14YWT

For 14YWT, cycles of the vacuum (10 min) and Ar purges (5 min) were repeated three times and a positive pressure of Ar was maintained throughout the milling period. The

modified milling procedure is illustrated in Figure 2-9.

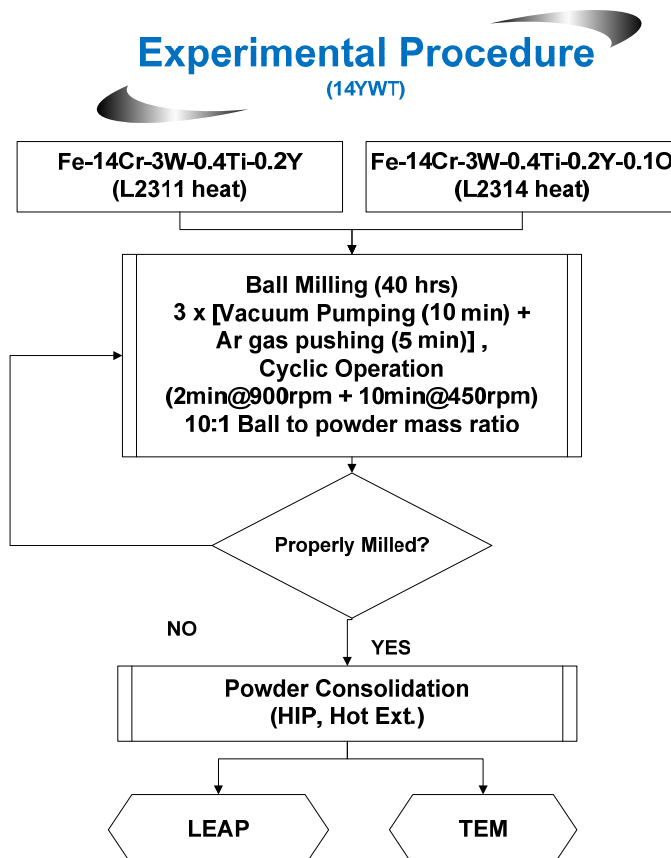


Figure 2-9. Modified experimental attritor milling procedure.

The compositional analysis of the L2314 milled powder presented in Table 2-4 shows that the modified attritor milling procedure successfully reduced N and other impurities contamination. The weight percent of N, O, and C in the milled powder sample by the preliminary attritor milling procedure was 0.016, 0.065, and 0.023 respectively. The N levels are down about a factor of 7-8 from prior measurement (Table 2-4). Improved milling procedures applied to these powders led to the effective elimination of the impurity N, however, it also resulted in lower O content, which will be discussed in Section 2.4. SEM EDS result also shows that N contamination was not observed in the 40 hr milled powder processed by the modified procedure as shown in Figure 2-10. Figure 2-11 shows the X-ray diffraction pattern of the L2314 powder for before and after milling for 40 hrs. After 40 hrs of milling, the peaks of Fe-Cr broadened and the intensity of the peaks decreased.

Table 2-4. Compositions of 14YWT (L2314) after milling for 40 hr

	Preliminary Procedure (wt%)	Modified Procedure (wt%)
Nitrogen	0.110	0.016
Oxygen	0.102	0.065
Carbon	0.035	0.023

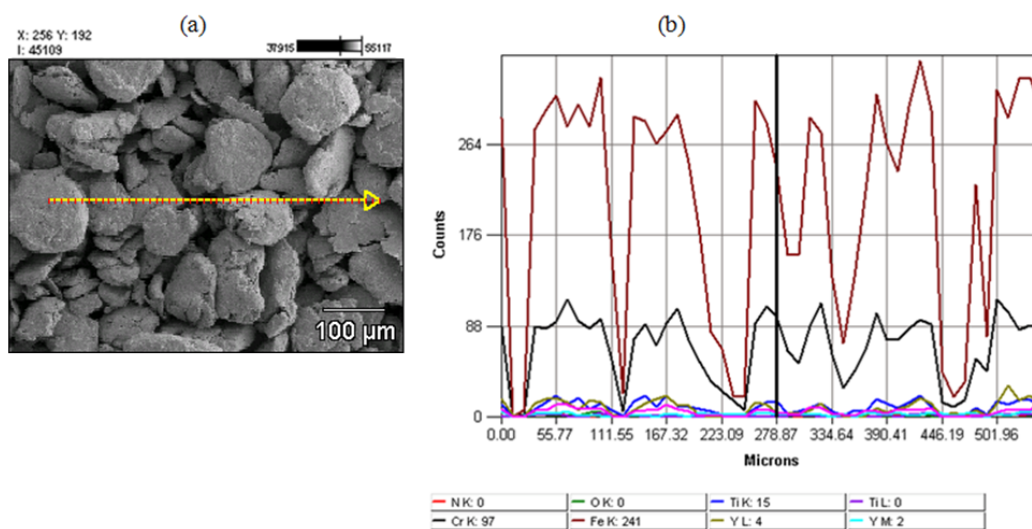


Figure 2-10. (a) SEM morphology and (b) EDS scan result of 40hr as-milled L2314 powder

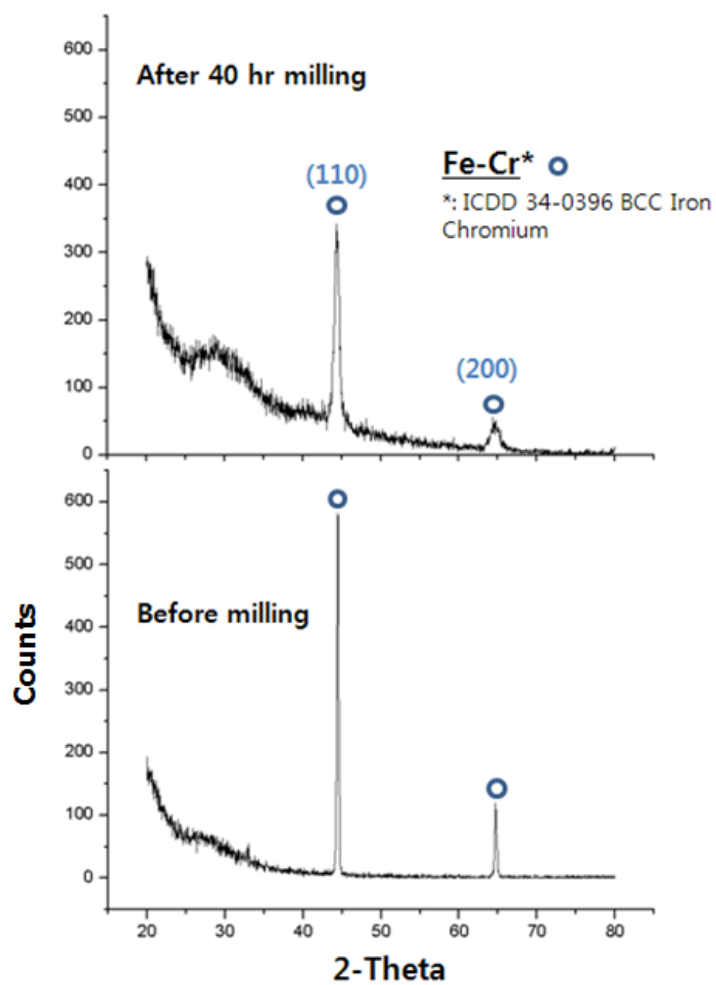


Figure 2-11. X-ray diffraction peak for L2314 powder, before and after milling for 40 hrs

2.2 Spark Plasma Sintering (SPS) for NiAl alloys

The SPS process [83] is a combination of conventional electric-current sintering and hot-pressing based on high temperature plasma instantly generated in the gaps between powders by electrical discharge current. Figure 2-12 shows an overview of the SPS process. Electric current is applied to a specimen in repeated ON-OFF DC pulse-form and the specimen is heated both by resistance heating of the specimen itself and the conductive die of a graphite mold. The spark discharge point and the Joule heating point are transferred and dispersed to the overall specimen homogeneously by repeated electric current pulse, which result in efficient sintering at low power consumption [83]. This SPS method has been employed in powder metallurgy to get advantages from faster heating and cooling rates and to achieve higher pressure during the sintering procedure [83-88], which allows obtaining high strength products in short periods of time, approximately 5 to 20 minutes, including temperature rise and holding times [89]. At the same time, bulk fabrication of particles with nano-crystallization formation is also possible without changing their characteristics [83]. As well, according to Kim [20] and Kitaoka [18], almost full density have been achieved in Ni-Al material systems via SPS. In this study, SPS method was utilized to consolidate the ODS NiAl alloys with improved high temperature strength. Figure 2-13 shows the basic configuration of a typical SPS facility. Densification behavior, microstructure and mechanical properties of the consolidated alloy specimens will be discussed in Chapter 3.

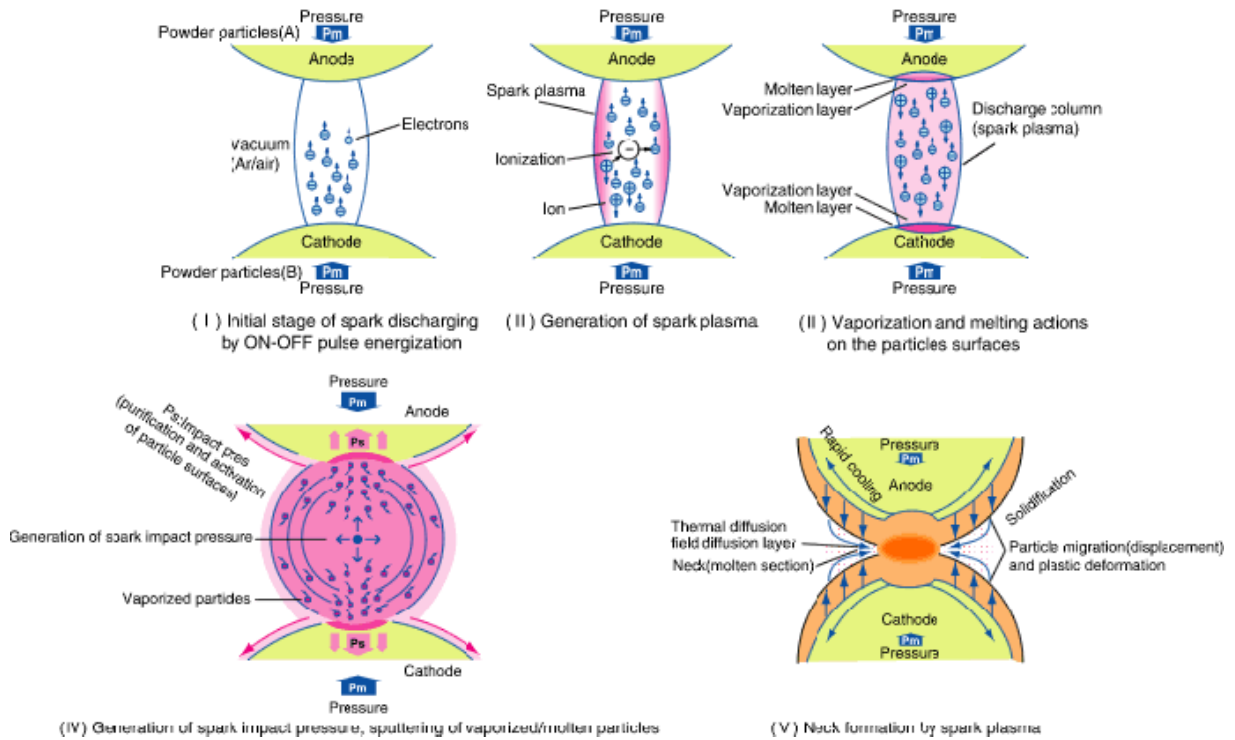


Figure 2-12. Basic mechanism of SPS as reproduced from Ref [83]

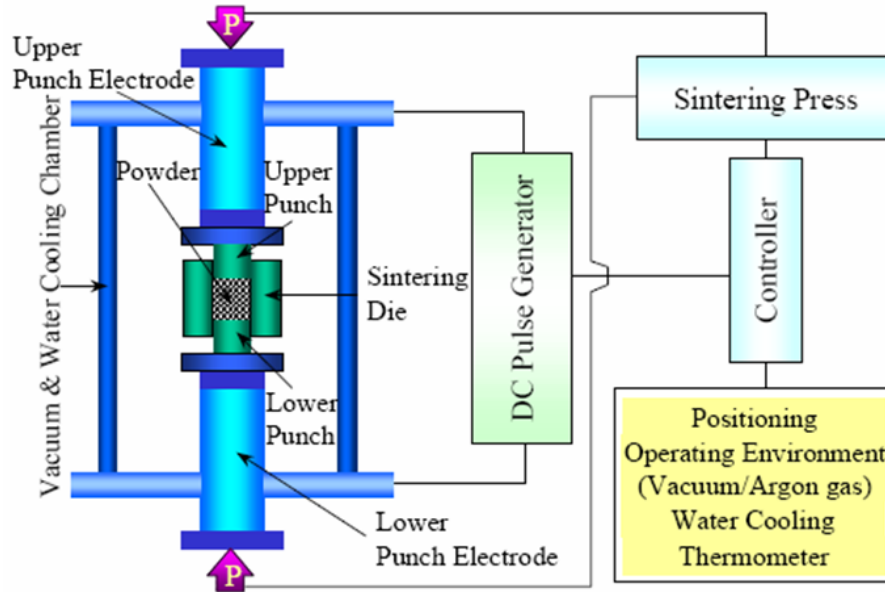


Figure 2-13. Schematic configuration of SPS facility as reproduced from Ref [83]

2.2.1 Consolidation of ODS NiAl alloys powder by SPS

Powder consolidation was carried out in a SPS facility at University of California Davis (UC Davis) under the heating conditions described in Figure 2-14. The pressure of 80MPa was applied to the powder specimens for 5 min at 1250°C and the vacuum chamber pressure was maintained at 10^{-5} torr during the sintering process. Sintered density was measured by an Archimedes electronic densimeter.

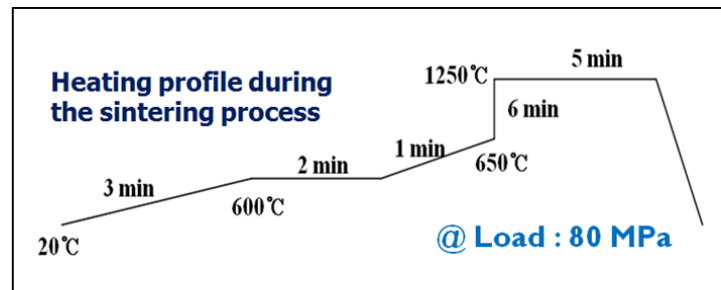


Figure 2-14. Heating profile during the SPS

2.3 Hot Extrusion and Hot Isostatic Pressing (HIP) for Fe-Cr based 14YWT

Hot extrusion (at ORNL) and HIP (at American Isostatic Presses) were performed to consolidate 14YWT powders. For the hot extrusion, the milled powders were sealed in 3 inch diameter mild steel cans, degassed in vacuum at 400°C, heated to 850°C for 1 hr and then extruded through a rectangular die. For the HIP, the powders were heated at a rate of 15°C/min and held at 1150°C for 3 hr under 200 MPa.

Chapter 3

Experimental Characterization Techniques

The materials processing involved mechanical alloying and consolidation by either spark plasma sintering for NiAl alloys or hot isostatic pressing/hot extrusion for 14YWT alloys discussed in Chapter 2. Subsequent microstructural characterization of the mechanically alloyed and consolidated alloys has been performed using X-ray diffractometry (XRD), scanning electron microscopy (SEM) along with energy dispersive X-ray spectroscopy (EDS), transmission electron microscopy (TEM), atom probe tomography (APT), and electron probe micro-analyzer (EPMA). Density and microhardness measurement of the consolidated specimen followed by spark plasma sintering were performed by electronic densimeter and Vickers microhardness tester respectively. This chapter briefly describes the experimental characterization techniques used in this study.

3.1 X-ray diffractometry

An X-ray diffractometer is composed of a source of X-rays, an X-ray generator, a diffractometer assembly, a detector assembly, and X-ray data processing system [90]. The diffractometer assembly controls the alignment of the beam, as well as the position and orientation of both the specimen and the X-ray detector. The XRD technique is applicable for an analysis of the powder crystallite size and lattice strain through an analysis of a decrease in intensity and peak broadening [91-95].

In this study, X-ray diffraction (XRD) was performed using a Siemens D-500 powder diffractometer at Lawrence Berkeley National Laboratory (LBNL) with a Cu target to generate K_{α} X-rays at settings of 40kV and 30mA. The diffractometer performed a continuous scan of 2θ from 20° to 90° at a rate of $0.01^{\circ}/\text{sec}$ to measure d-spacings. The powders were placed in a quartz container with the top surface of the powders level with the axis of rotation for the diffractometer. All of the acquired peaks were identified by International Centre for Diffraction Database (ICDD) [96]. The diffraction data were corrected for instrument broadening and fit with Gaussian functions for measuring the peak broadening.

The ball milling process causes a decrease in the diffraction peak height and an increase in the diffraction peak width with the milling times, which indicates that the crystalline size, or grain size, of the powder decreases and the micro-strain increases since the ball milling involved massive plastic deformation [44, 46, 75, 92, 93, 97-99]. Assuming a linear superposition of these effects, the total peak broadening can be described by the Hall-William equation [95]:

$$B \cdot \cos \theta = 2\varepsilon \cdot \sin \theta + \frac{\lambda}{D} \quad (3.1),$$

where B , θ , ε , λ , and D are the experimentally determined width of half maximum of the Bragg peaks, diffraction angle, micro-strain in crystallites, wavelength of incident X-rays, and grain size of the crystalline respectively. Figure 3-1 schematically illustrates the Full Width at Half Maximum to determine B from measured diffraction data. The quantities D and ε can be determined from the extrapolated intercept and the slope in plots of $B \cdot \cos \theta$ versus $2\sin\theta$ from the diffraction peaks.

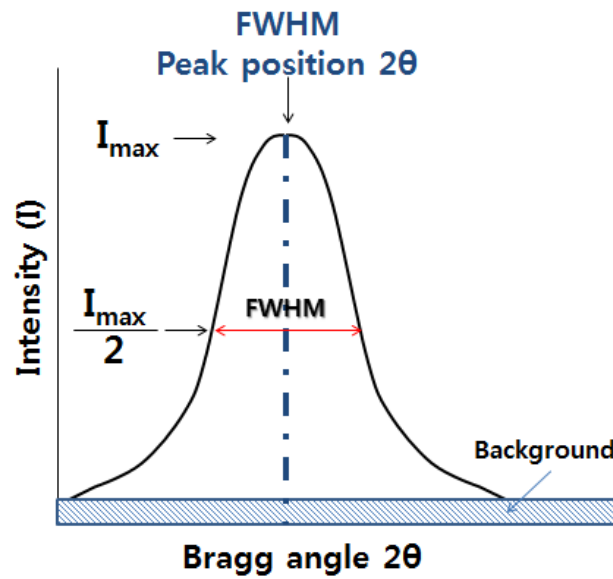


Figure 3-1. Full Width at Half Maximum (FWHM) determination from XRD peak (schematic) as reproduced from Ref [92]

The internal micro-strains generated during the ball milling could be the result of dislocation generation and of rewelding of powder particles [93]. According to Williamson [91], we can estimate the dislocation density ρ_d by equating the elastically stored energy with the total line energy of the dislocations as described by:

$$\rho_d = \frac{6\pi E}{Gb^2 \ln(r/r_0)} \varepsilon^2 \quad (3.2),$$

where E , G , b , r/r_0 , and ε are Young's modulus, shear modulus, Burgers vector, the ratio of external radius of cylinder containing the dislocation to core radius of dislocation, and micro-strain in crystallites respectively. For the present work, pure NiAl data [100], $E=188\text{GPa}$, $G=71.5\text{GPa}$, $b=0.288\text{nm}$, and $\ln(r/r_0) = 4$, were used.

3.2 Scanning electron microscopy and Energy dispersive X-ray spectroscopy

“SEM provides magnified images that closely approximate what our eye and brain expect, because the depth of field for resolved in the SEM is much greater than the spatial resolution in the field of view, which provides a perceived three dimensional topological and morphological detail in the images” [90]. The basic components of the SEM include a microscope column, various signal detector systems, the computer system used to process the collected data.

The SEM analysis was performed using a Hitachi S-4300 SEM machine equipped with EDS system to investigate the microstructure of the ball milled powder. The chemical compositional analysis was carried out by the EDS based on K and L characteristic X-rays spectra acquired at 20kV and the holding time for analysis was 10 minutes. In energy dispersive spectroscopy, the excited photons are collected as a function of their energy and spectrum of energy dependent photon intensity is analyzed to determine the chemical composition of the region of the sample excited under the electron beam [90, 101].

3.3 Transmission electron microscopy

Magnified images at a very high resolution, at the nanometer and even sub-nanometer length-scale, is currently available from transmission electron microscope. “However, the most important characteristic of the TEM is that it combines real space information at excellent resolution with information from the same object obtained in reciprocal space, electron diffraction patterns, can be recorded” [90, 102, 103]. As well, microanalytical techniques can be integrated into the same instrument, which makes the TEM one of the most versatile and powerful tools available for microstructural characterization. A TEM is composed of several components, which include a vacuum system in which the electrons travel, an electron emission source for generation of the electron stream, a series of electromagnetic lenses, as well as electrostatic plates.

The high resolution microstructures were observed by transmission electron microscopy. The TEM was performed using a Philips CM200 at ORNL and Philips CM300 at LBNL microscope with a 200 and 300 keV field emission gun respectively. The TEM

samples were prepared to have a thickness of 40-70 μm by mechanical polishing and then electropolished to have a final thickness of ~ 100 nm using a Fischione twin-jet polisher. The electrolytic solution and condition used are 25% HNO_3 -75% methanol at -12°C at 18 V. Conventional bright field TEM imaging and high resolution TEM imaging studies were performed. The EDS spectra for compositional analysis were recorded in Energy Filtered TEM (EFTEM) and Scanning transmission electron microscopy (STEM) mode at Philips CM200. Microstructural features, grain size and particle number density, were measured by Image-J and Adobe Photoshop computer program.

3.4 Atom probe tomography

Atom probe tomography (APT) is an ultra-high resolution microanalytical technique for the atomic and nanoscale characterization of microstructural features. “Atom probe is able to provide unique three-dimensional information on the atomic-scale chemistry within the bulk of a material” [104]. Atom probe (shown schematically in Figure 3-2) essentially combines a field ion microscope that can analyze a specific atom or region with a time-of-flight mass spectrometer coupled with a position sensitive detector [104, 105]. When the electric field reaches a critical value, the surface atoms of the specimen are ionized and field evaporate. The ions generated are subsequently accelerated away from the surface of the specimen by the highly divergent electric field surrounding the specimen, which gives rise to a highly magnified projection of the ions [104-106]. The flight time of the ion is measured resulting in a mass-to-charge ratio (elemental identity).

The APT was performed using a Cameca-Imago Instruments 4000X HR LEAPTM at ORNL. Samples were prepared by electropolishing and focused ion beam (FIB) using a FEI Nova 200. The APT sample is typically in the shape of a sharp needle (tip radius ≈ 10 -100 nm) shape (shown in Figure 3-3) that produces a field enhancement for field emission/evaporation of the surface atoms. The LEAP samples were examined in voltage mode and temperatures were maintained at 50K. Voltage pulses were held at 200 kHz repetition rate, the evaporation rate was typically between 0.5% and 1%.

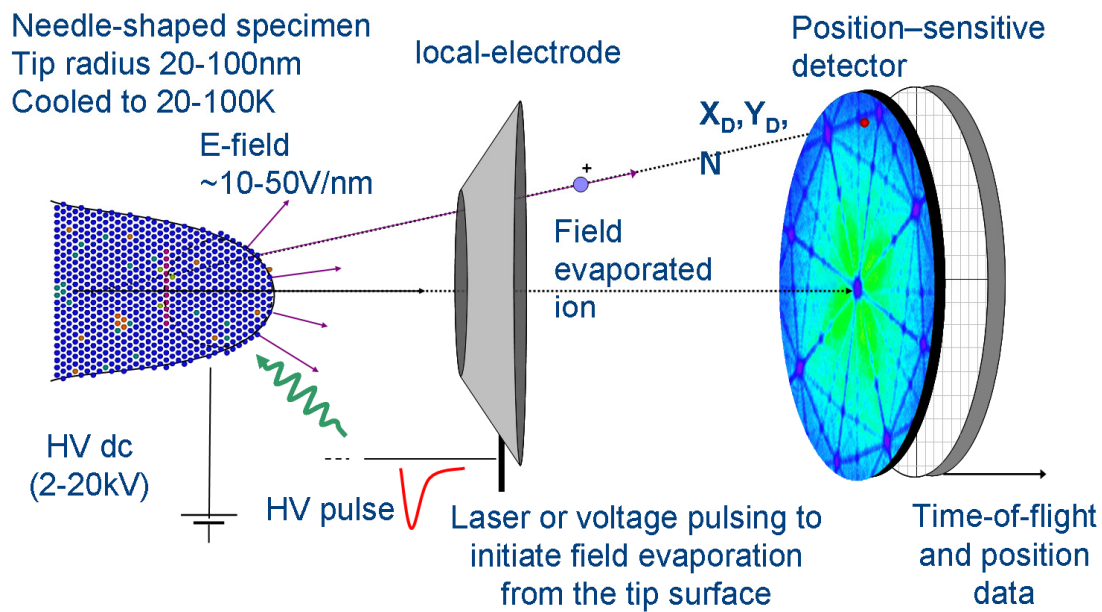


Figure 3-2. Schematic diagram of a 3D atom probe as reproduced from Ref [106]

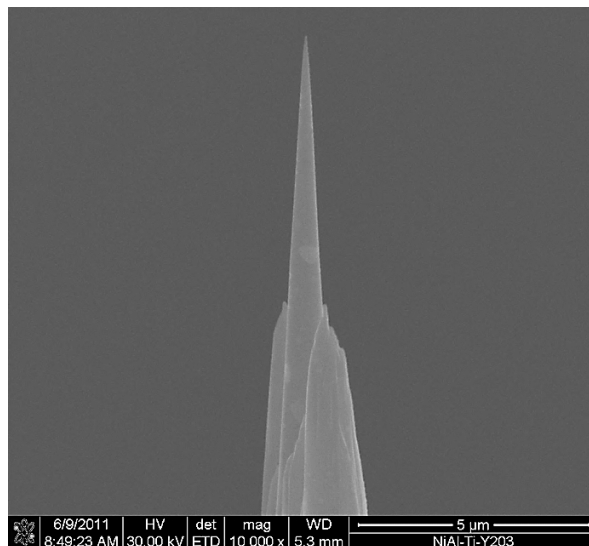


Figure 3-3. Typical APT specimen of the NiAl-Y₂O₃-Ti alloy (FIB milled)

3.5 Microhardness

Vickers microhardness measurement was performed to characterize the basic mechanical properties of the alloy materials using both Buehler microhardness tester at LBNL and Wilson 400 series Knoop/Vickers automated hardness tester at ORNL. The microhardness test was performed using a diamond pyramid indenter on a polished specimen surface. A 50g of load is applied to the Vickers indenter for 15 secs and the microhardness data was measured from approximately 10-20 indentation points. Figure 3-4 shows a typical indentation image, and a Vickers hardness value is calculated by:

$$H_v = \frac{2F \cdot \sin(68^\circ)}{d^2} \quad (3.3),$$

where F is the applied load in kg and d is the average of the two diagonals, d_1 and d_2 , of the indentation in mm. Because the Vickers hardness value is known to represent an average flow stress of the material, it can be empirically correlated to uniaxial yield strengths using the correlation [68]:

$$\sigma_y \cong \frac{H_v}{3} \quad (3.4),$$

where σ_y and H_v are the 0.2% offset yield strength (kg/mm^2) and Vickers microhardness.

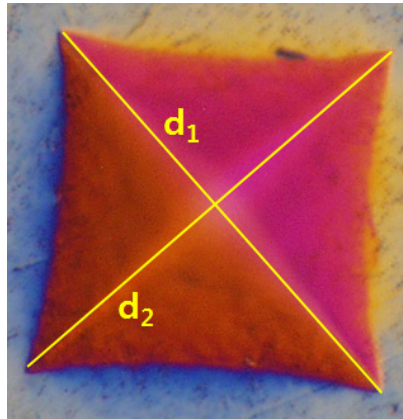


Figure 3-4. Typical Vickers hardness indentation image of the NiAl alloy

3.6 Chemistry analysis

The composition analysis of the powders following the ball milling was provided by Luvak Inc. Electron probe micro-analyzer (EPMA) was performed to investigate Y and Ti

distribution in as-milled powders using a Cameca SX-50 at UCSB. The powders were mounted in a conductive polymer and polished to a 0.05 μm finish. Three to five measurements were made on each powder particle.

Chapter 4

Results of Microstructural Characterization in As-milled and Consolidated Conditions

Microstructural characterization of the as-milled powders and the consolidated alloys were performed using the variety of techniques discussed in Chapter 3. Combinations of these techniques were used to assess the effects of alloy composition, mechanical alloying (milling), and consolidation. The objective of this chapter is to understand the sequence-of-events and factors controlling the evolution of nanoscale precipitates and other features in 14YWT and NiAl alloys. Such understanding provides a basis for optimizing alloy process.

The EPMA analysis showed the distribution of Y and Ti in as-milled powder particles associated with the milling time. X-ray diffraction patterns confirmed that mechanical alloying process dissolved the alloying elements and phases into the matrix. SEM along with energy-dispersive X-ray spectroscopy (EDS) provided information regarding the morphology of the as-milled powders and the distribution of the phases present in the microstructure of the alloys. Bright-field and phase-contrast imaging along with EDS were performed in the transmission electron microscope. APT analysis has also been performed to investigate the size, concentration and morphology of nanometer-scale precipitates.

4.1 14YWT alloys

A variety of characterization studies were carried out to determine the optimal fabrication and consolidation conditions which would effectively homogenize the alloying elements. This section specifically focuses on investigating the optimal milling time which can produce alloys with more homogeneous distributions of NCs and more uniform fine grain size distributions.

4.1.1 Results of ball milling

The investigation of elemental distribution associated with the milling time has been performed using an electron probe micro-analyzer (EPMA) and a PGT X-ray energy dispersive detector. Milling for 20 hr resulted in a wide variation of Y concentration persisted in some particles (Figure 4-1(a)). The 40 hr milling provided a much more uniform distribution of Y and Ti both within and between particles (Figure 4-1(b)). The EPMA results demonstrated that it was not sufficient for 5 and 20 hr ball milling to obtain a uniform distribution of Y and Ti in the alloy.

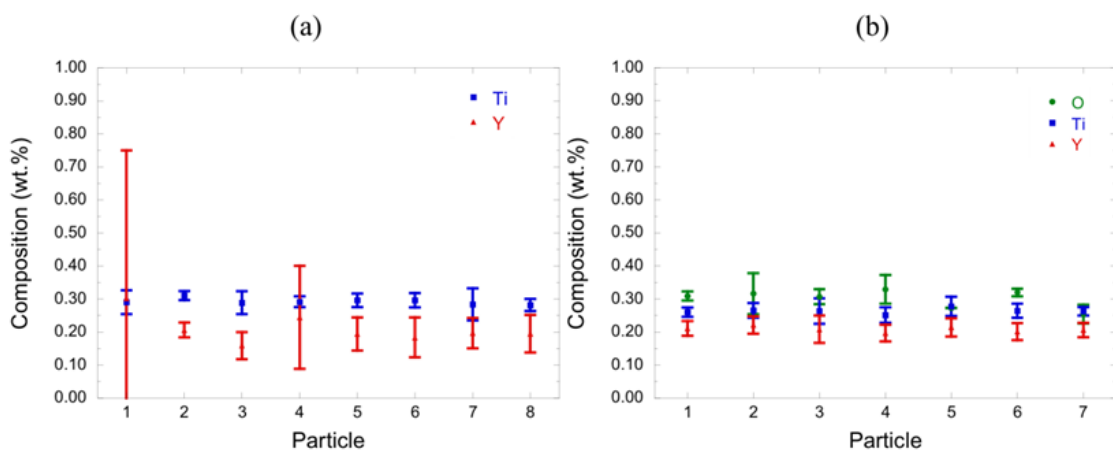


Figure 4-1. EPMA analysis of ball milled powder (a) after 20hr of milling (b) after 40hr of milling

The typical powder morphology of 14YWT powder after 20 and 40 hr ball milling is shown in Figure 4-2. The 20 hr milled powders are flake shaped with a large range of sizes from 100 to 200 μm while the 40 hr milled powders also have flake shape but smaller particle sizes of about 10 to 100 μm .

X-ray elemental mapping using the SEM EDS equipment was performed for the 40 hr milled powder to investigate the microstructural distribution of the alloying elements, Ti, Y, and W, in the Fe-Cr matrix. This EDS analysis was based on K and L characteristic X-rays spectra acquired at 20kV and the holding time for analysis was 10 minutes. The identified elements of Fe, Cr, Ti, Y, and W were mapped from the selected powders region respectively as shown in Figure 4-3. This EDS results reveals Ti, Y, and W entirely distributed in Fe-Cr matrix powder at this spatial resolution.

The EPMA result (Figure 4-4) shows the tremendous effect of ball milling for 5 hr (Figure 4-4(a)) versus 40 hr (Figure 4-4(b)) on the Y and Ti distribution in a hot extruded 14YWT alloy. Notably, there is also large variation in the Ti and Y after 5 hr of milling.

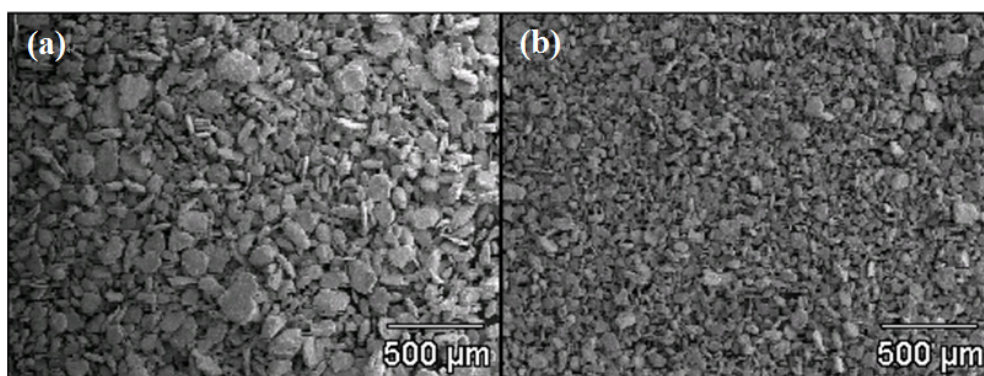


Figure 4-2. Typical SEM images of 14YWT (L2311) powder (a) after 20 hr milling (b) after 40hr milling

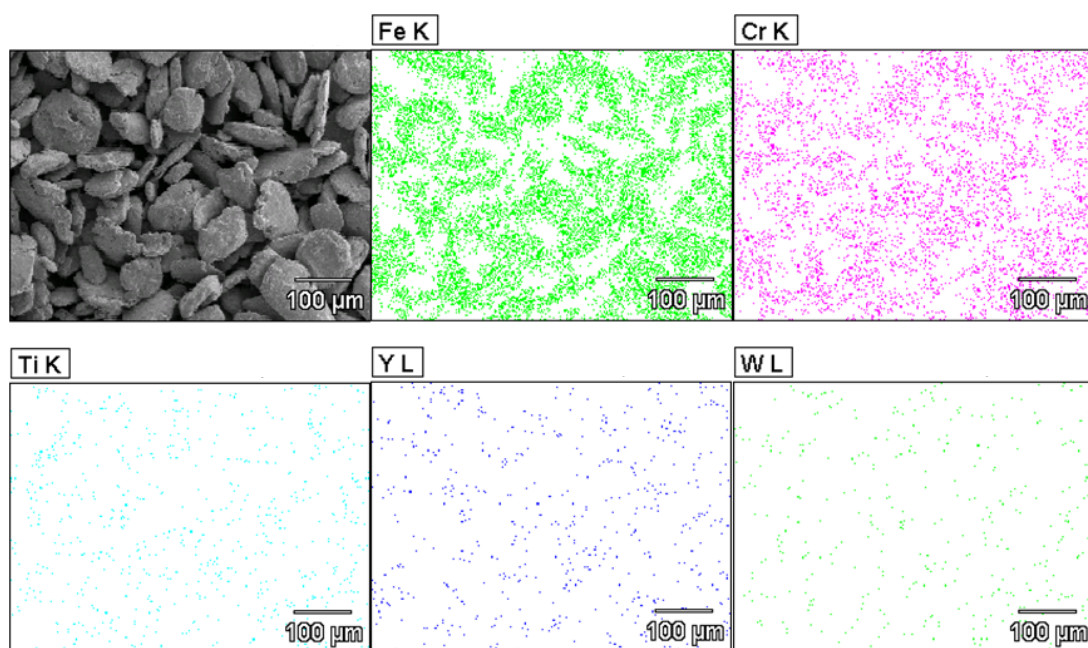


Figure 4-3. X-ray elemental (Fe, Cr, Ti, Y, W) mapping of the 14YWT powder after 40hr ball milling

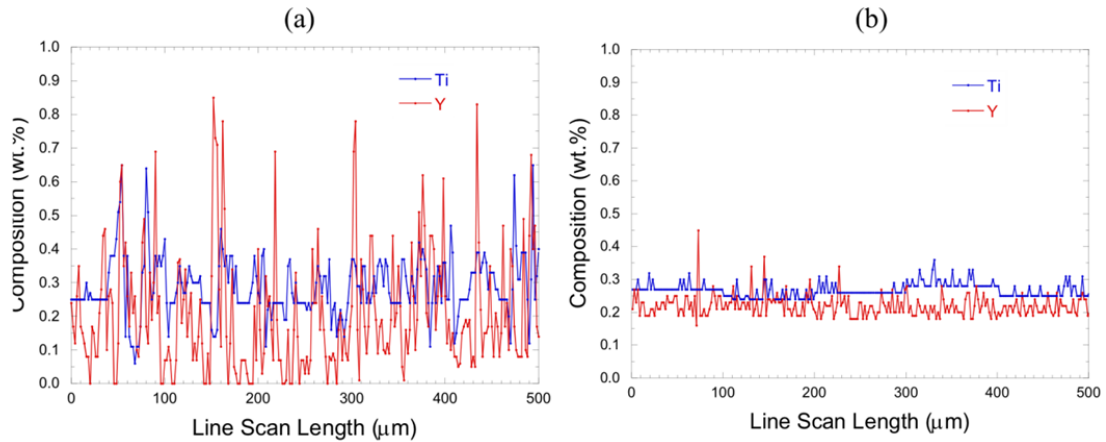


Figure 4-4. EPMA analysis showing the Y and Ti distribution in hot extruded 14YWT (L2311) alloy that were prepared from (a) 5 h and (b) 40 h ball milled powder

TEM characterization was carried out for further higher resolution study on this alloy. The TEM micrographs in Figure 4-5 show the typical NC distribution in L2311 and L2314. The average NC size or diameter and number density in the L2314 alloy, measured by TEM, are 4.7 nm and $6.2 \times 10^{22}/\text{m}^3$, respectively. The NCs in the L2314 alloy are coarser than those in L2311 which had a size of 2.4 nm and a number density of $2.8 \times 10^{23}/\text{m}^3$.

Figure 4-6 shows examples of representative NCs found in the APT studies of L2311 and L2314. The corresponding NCs diameter and number density in the L2311 alloys are 1.7 nm and $2.9 \times 10^{23}/\text{m}^3$, and 5.8 nm and $6.0 \times 10^{22}/\text{m}^3$ in the L2314, which is in quite good agreement with the TEM characterization.

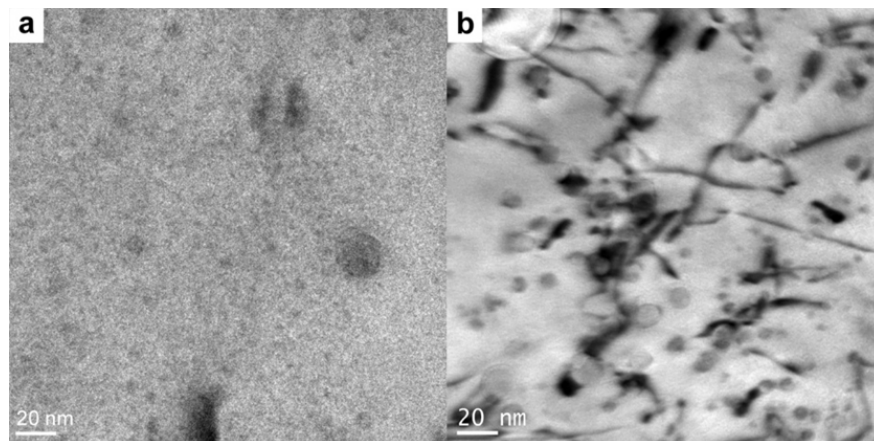


Figure 4-5. Typical conventional TEM images of 40 hr milled and HIPed at 1150°C at 200 MPa (a) L2311 (b) 2314

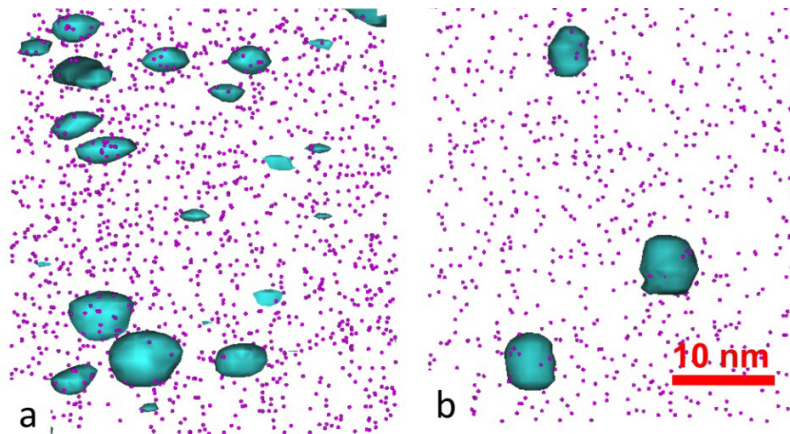


Figure 4-6. 20 nm thick Atom maps with Cr ions and Y-Ti-O isoconcentration surfaces for (a) L2311 (b) L2314.

4.1.2 Discussion

Improved milling procedures led to the effective elimination of the impurity N, however, it also resulted in lower O content as noted in Section 2.1.4. Thus, the study was extended to evaluate the effect of the O content in the range from 0.065 to 0.249% (by weight) on the microstructure, in terms of the NC distribution and microhardness of the consolidated 14YWT alloys by Y.Wu et al [107]. It reported that the microhardness increases systematically with O as shown in Figure 4-7. Y.Wu pointed out “the higher hardness in the highest O alloy was in some or large part due to the larger fraction of fine grains. The low O alloy contains fewer and coarser NC, with higher Y/Ti ratios, and a larger average grain size, compared to the higher O 14YWT”. Notably, as shown in Figure 4-8, microhardness (H_v) increases in direct proportion to the square root of volume fraction of the NCs (\sqrt{f}). These observations indicate the importance of properly balancing Y, Ti, O elemental compositions and developing processing path to produce microstructures that lead to more optimal properties. However, further discussion of these issues is beyond the scope of this dissertation.

In summary, it is considered that 40 hr ball milling is appropriate for the optimal milling time which can produce alloys with more homogeneous distributions of NCs in the 14 YWT alloys.

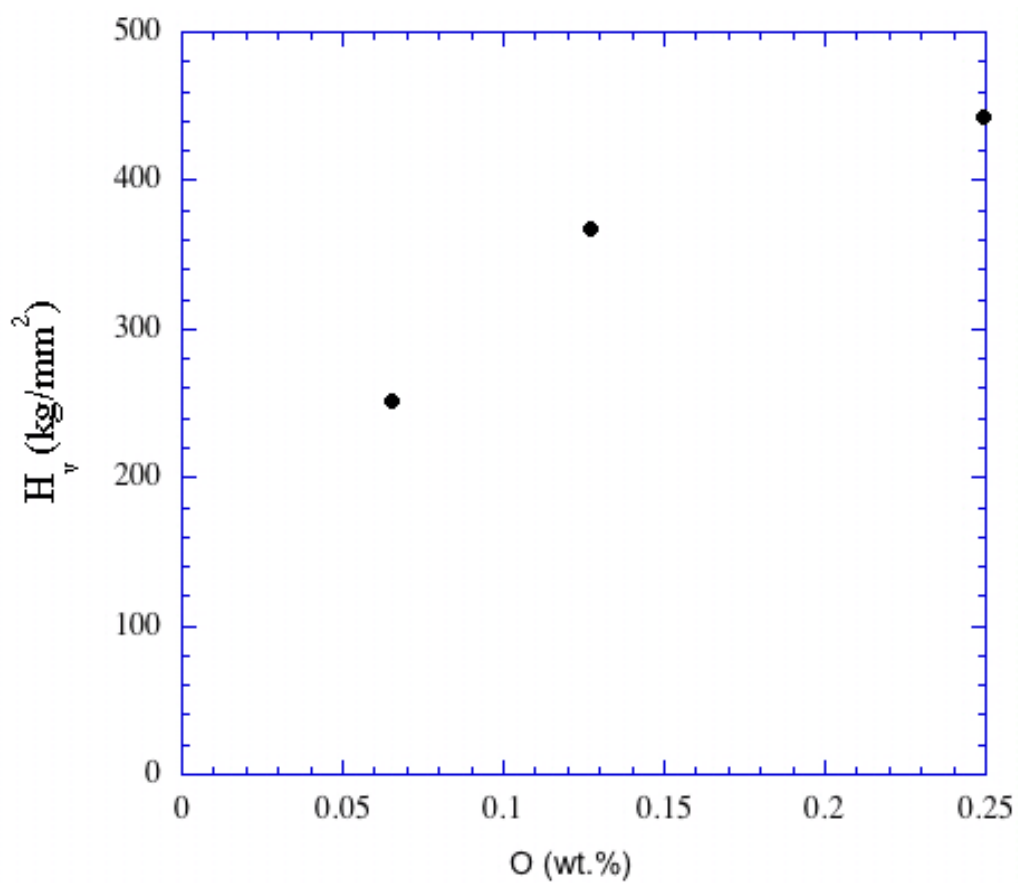


Figure 4-7. Vickers microhardness, H_v , versus O content as reproduced from Ref [107]

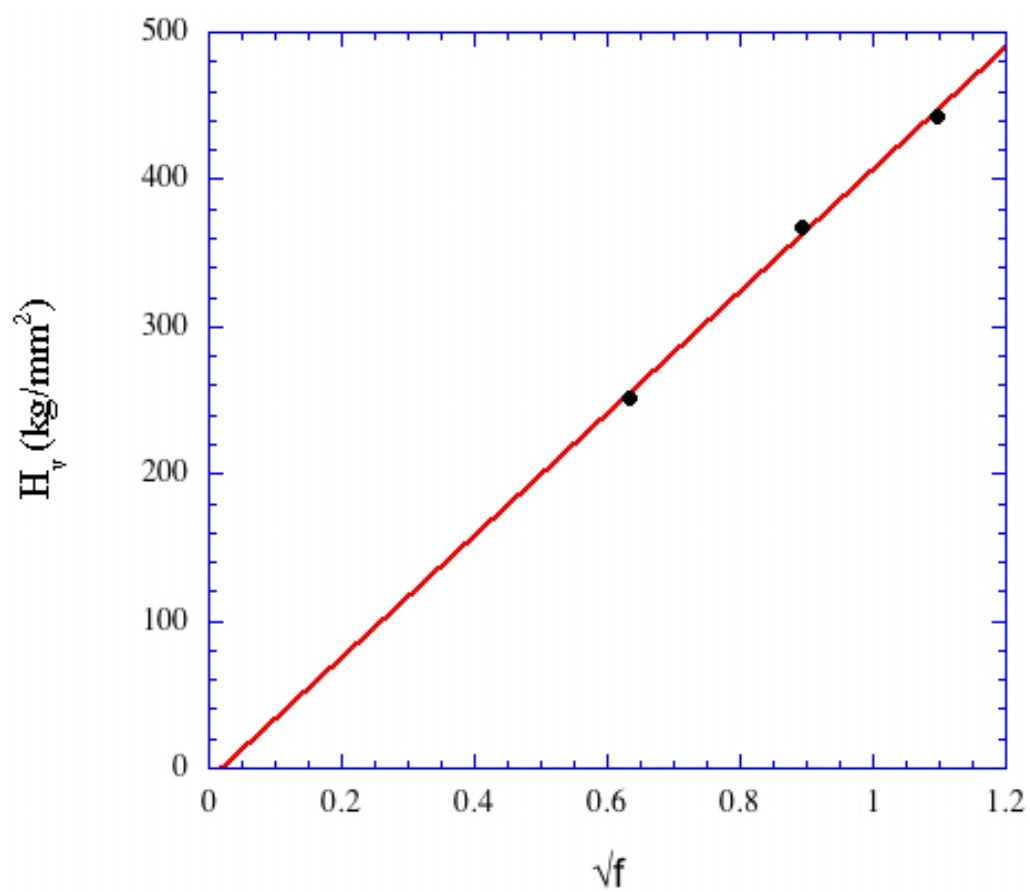


Figure 4-8. The alloy H_v versus the square root of the NCs volume fraction (\sqrt{f}) as reproduced from Ref [107]

4.2 NiAl alloys

Microstructural characterization of the mechanically alloyed NiAl powders and SPS consolidated NiAl alloys has been performed for developing a process path to produce the microstructures that lead to the best properties of the alloy.

4.2.1 As-milled powder characterization

4.2.1.1 X-ray diffractometry

Figure 4-9 illustrates the evolution of XRD as a function of milling time for three NiAl alloy powder blends. Bragg diffraction peaks of NiAl, Y_2O_3 and Ti are clearly visible for the initial powder mixtures but the peaks of alloying elements, Y_2O_3 and Ti, cannot be revealed for the powders after 2 - 10 hour ball milling. It is considered that more than 2 hour of milling time led to the disappearance of the XRD peak for Y_2O_3 and Ti caused by dissolution into the NiAl matrix. Figure 4-10 shows the calculated grain size and strain values from equation (3.1) as a function of milling time for the mechanically alloyed powders. Increased milling time results in a gradual decrease in the average crystallite sizes and increase in the average strain of NiAl alloys. The average grain size is dramatically decreased from 60 nm to 15 nm after 2 hour milling and then saturated to approximately 10 nm after 10 hour milling while the strain value is substantially increased after 2 hour milling and then gradually increased to 0.27% after 10 hour milling. These values are comparable to those reported by other investigators [75, 98]. Dislocation densities were calculated by using equation (3.2) as a function of the milling time and are shown in Figure 4-11. The dislocation density is rapidly increased to $5 \times 10^{14}/m^2$ after 2 hour milling and then saturates to a value of $10^{15}/m^2$ which corresponds to a typical dislocation density in heavily cold-worked metals [91, 93].

4.2.1.2 Scanning electron microscopy

Figure 4-12 shows typical SEM micrographs of the NiAl-1wt% Y_2O_3 -1wt%Ti composition powders before and after the ball milling using a Hitachi S-4300 SEM machine with 20kV accelerating voltage. Figure 4-12(a) shows the micrographs of elemental mixture powders before the ball milling. The powders are spherical shape and have various sizes of 5 – 40 μm . After 2 hr ball milling (Figure 4-12(b)), the powders are uniformly refined and have a flake shape less than 10 μm . After 5 -15 hr ball milling, the powders have sizes of 5 – 10 μm . There is no significant change in size and shape after 5 hr ball milling.

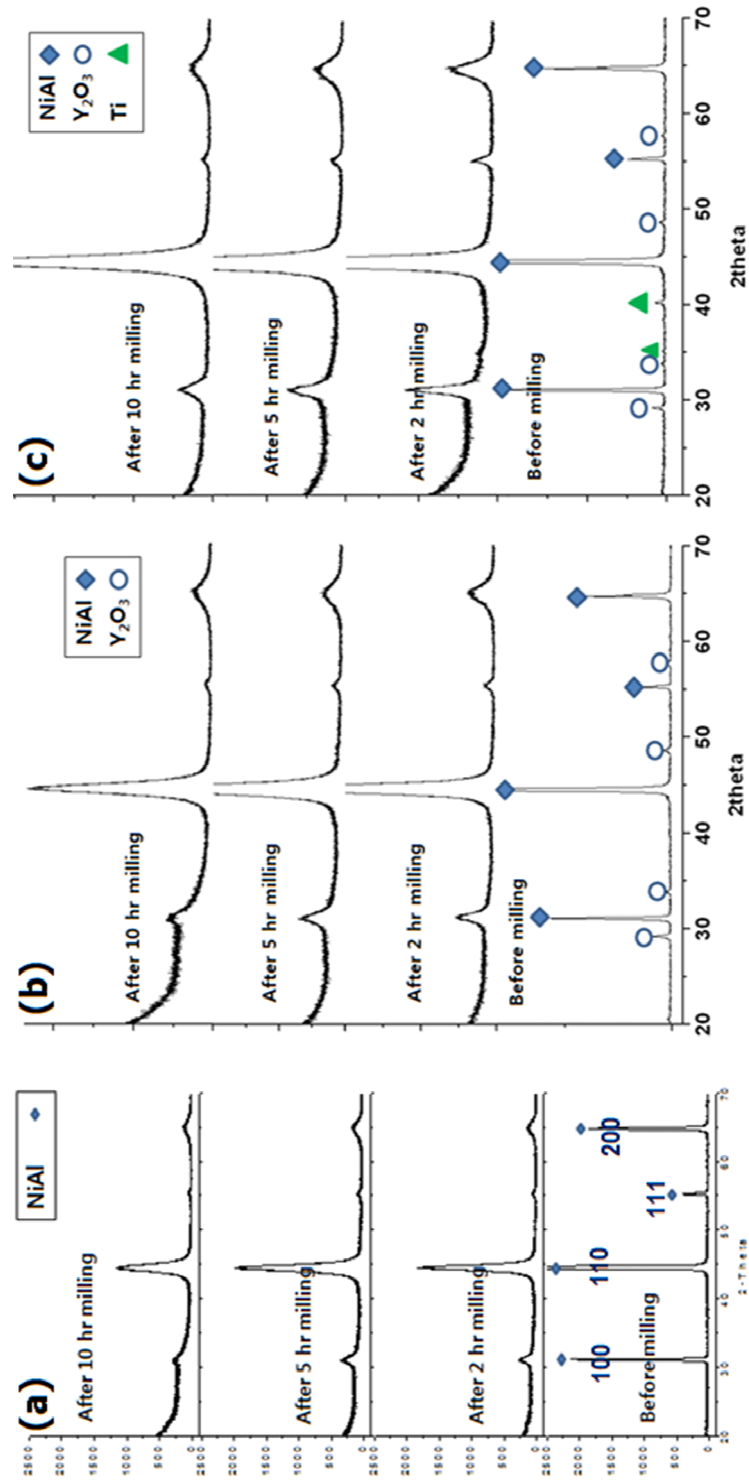


Figure 4-9. XRD patterns of the mechanically alloyed powders as a function of milling time (a) NiAl (b) NiAl-1 wt%Y₂O₃ (c) NiAl-1 wt%Y₂O₃-1 wt%Ti.

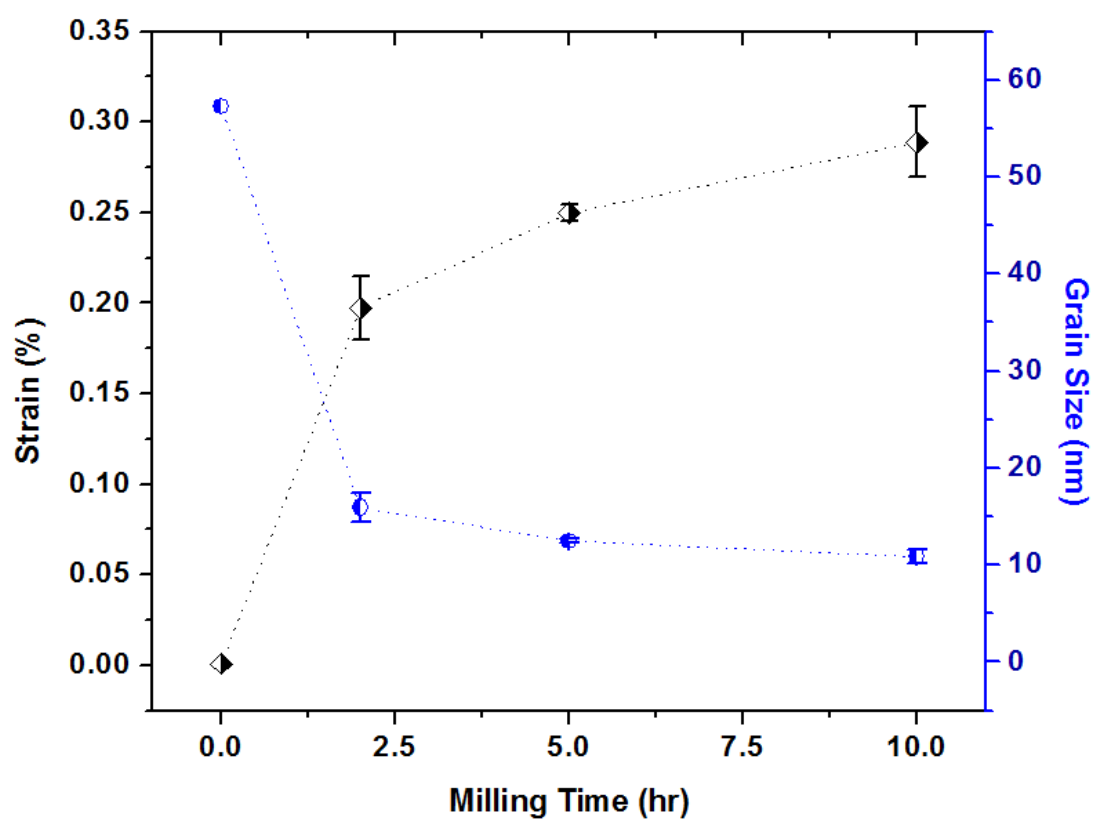


Figure 4-10. Calculated grain size and strain of the mechanically alloyed powders as a function of milling time (3 alloys averaged)

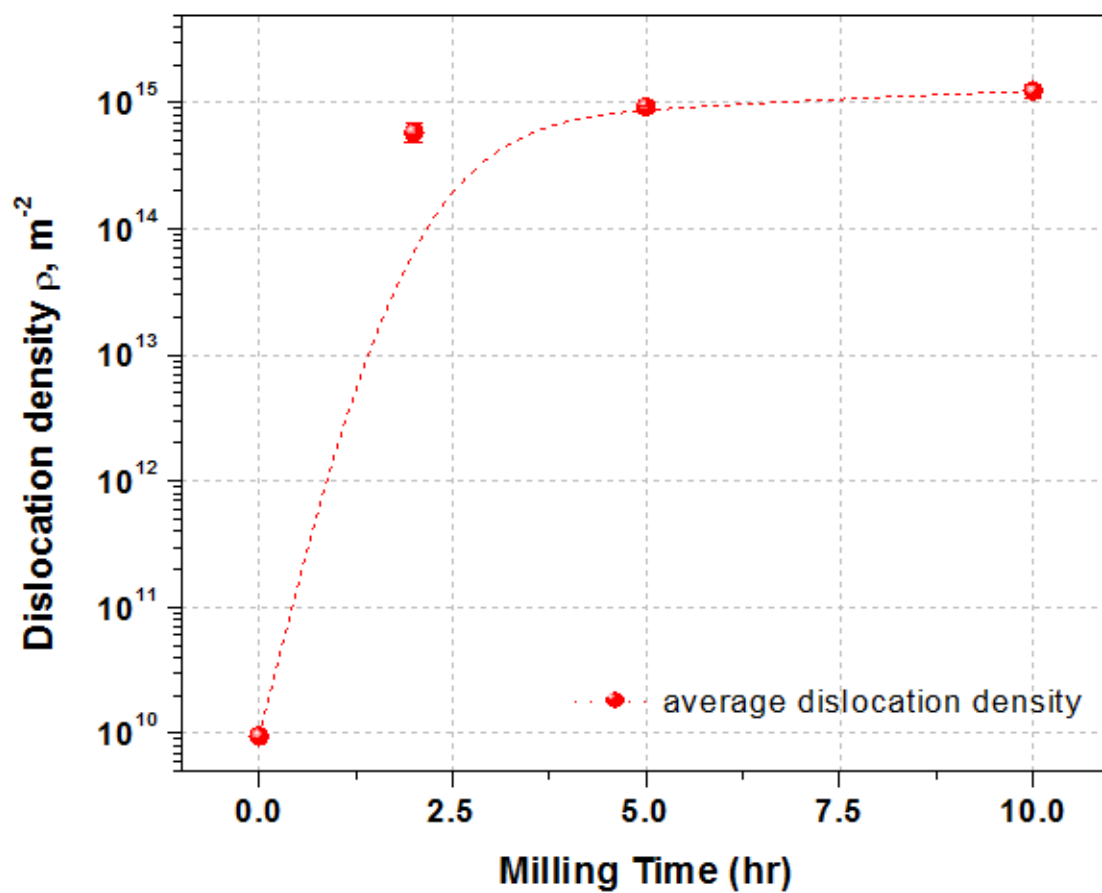


Figure 4-11. Calculated dislocation density of the mechanically alloyed powders as a function of milling time (3 alloys averaged)

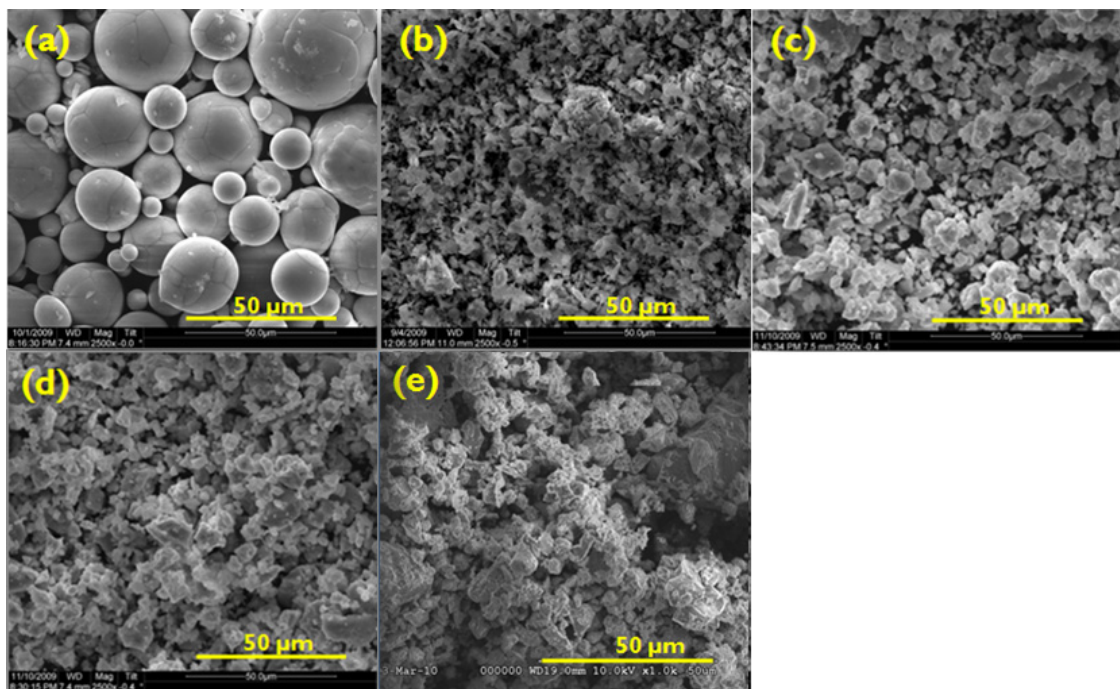


Figure 4-12. SEM micrographs of NiAl-1wt.%Y₂O₃-1wt.%Ti powder as a function of milling time;
(a) before milling (b) 2 hr (c) 5 hr (d) 10 hr (e) 15 hr ball milling

4.2.1.3 Energy dispersive X-ray spectroscopy

X-ray elemental mapping using the SEM EDS equipment was performed for mechanically alloyed NiAl-1 wt%Y₂O₃-1 wt%Ti powders to investigate the microstructural distribution of the alloying elements, Y₂O₃ and Ti, in the NiAl matrix. This EDS analysis was based on K and L characteristic X-rays spectra acquired at 20kV and the holding time for analysis was 10 minutes. The identified elements of Ni, Al, Y, O, and Ti are mapped from the selected region respectively as shown in Figure 4-13. Figure 4-13(a) shows the result of the EDS examination of the NiAl-1wt%Y₂O₃-1wt%Ti powder before the ball milling and it clearly reveals each elemental region. After 10 hr ball milling, however, agglomerated particles disappeared and all the regions contain the matrix and alloying elements as shown in Figure 4-13(b). Figure 4-14 shows the energy dispersive X-ray spectra map for the specified region corresponding to one of the particles present in Figure 4-13(b). It clearly shows that Ni and Al as matrix elements exist in the entire particle and the alloying elements are also uniformly distributed in the particle.

4.2.1.4 Discussion

During mechanical alloying, the powder undergoes severe plastic deformation through cold-welding and fracture of particles, and therefore, its micro-strain increases and the crystallite size decreases. It can be noted that mechanical alloying is an effective approach to reduce the average crystallite size to the nanocrystalline range of dimension in a relatively short time. Though the mechanism controlling dissolution of the alloying elements in the mechanically alloyed NiAl powders could not be precisely identified, there is a clear indication that milling for 5-15 hrs is actually sufficient for good mixing during the mechanical alloying process.

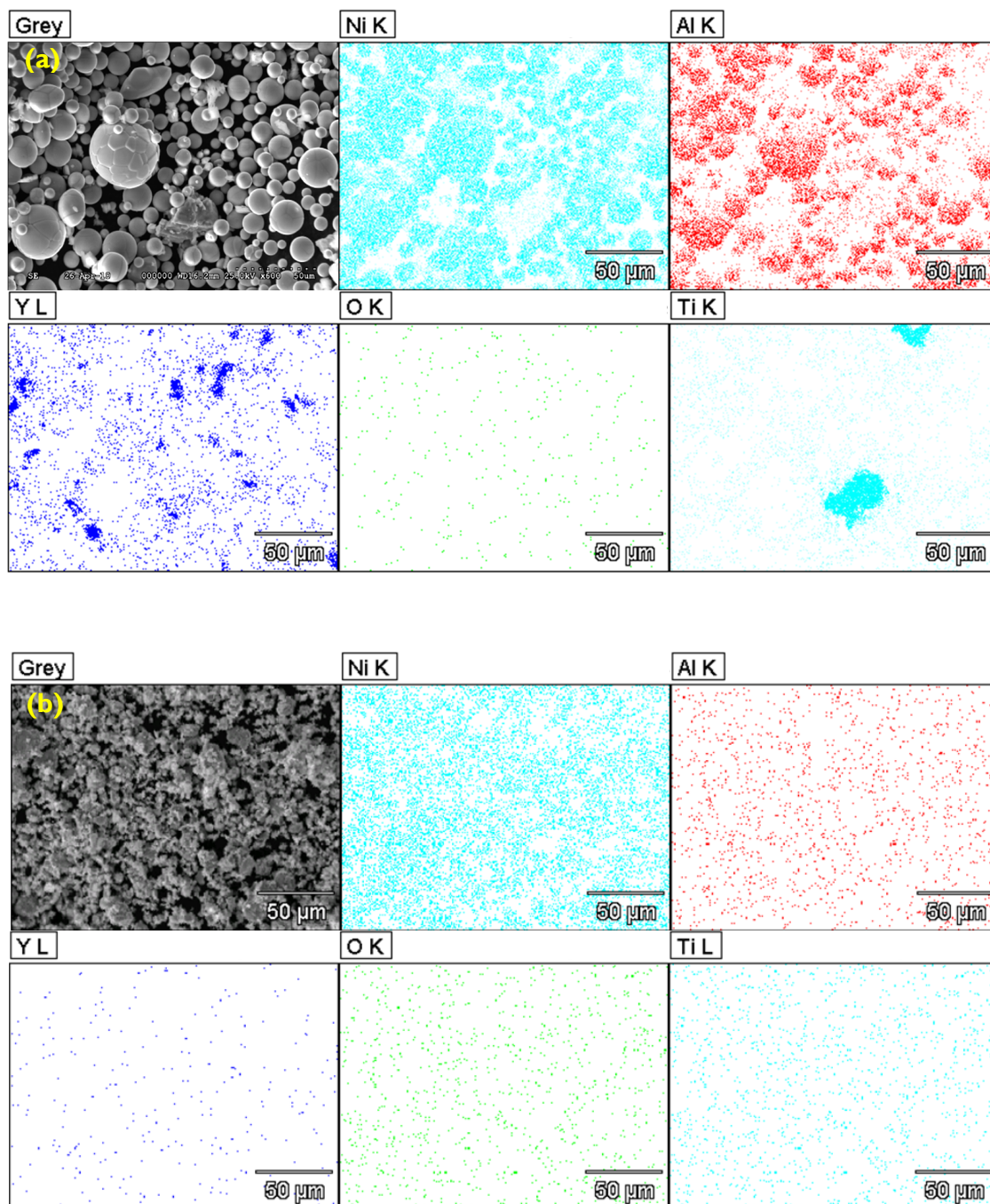


Figure 4-13. X-ray elemental (Ni, Al, Y, O, Ti) mapping of the $\text{NiAl-1wt\%Y}_2\text{O}_3\text{-1wt\%Ti}$ powder, (a) before milling (b) 10 hr ball milling

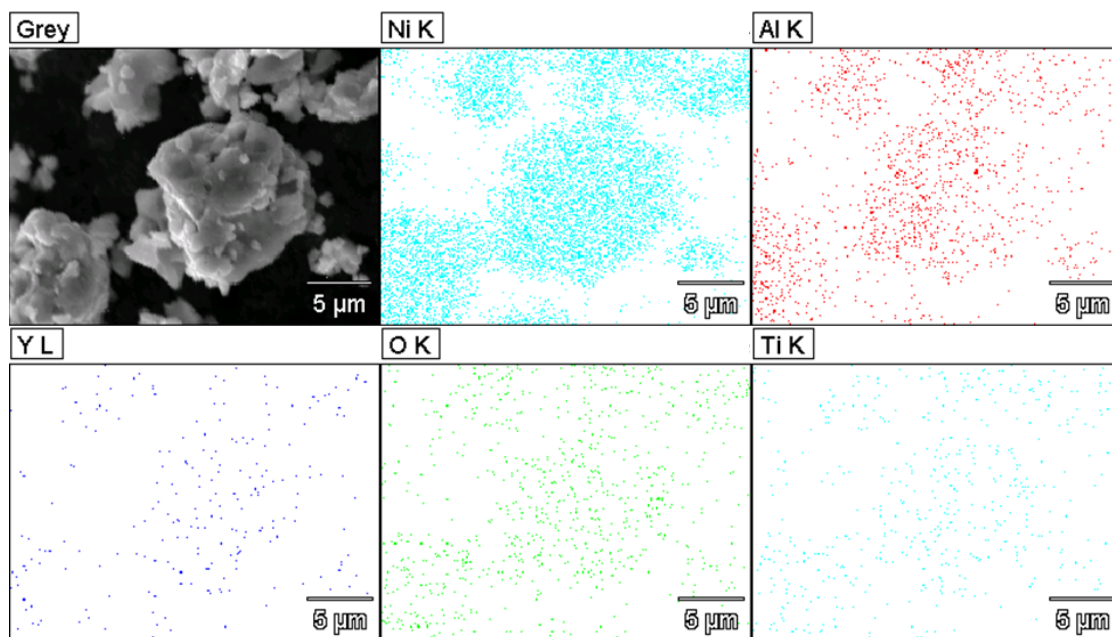


Figure 4-14. X-ray elemental (Ni, Al, Y, O, Ti) mapping from the identified region in Figure 4-13(b).

4.2.2 Consolidated specimen characterization

Powder consolidation was carried out by the spark plasma sintering (SPS) method described in Chapter 2. This section describes the microstructural characterization study performed on the consolidated NiAl alloys along with microhardness measurement. The effort has gone into rationalizing the relationship between the strength and the microstructure of the ODS NiAl alloys

4.2.2.1 Density

Sintered density was measured by an electronic densimeter. Figure 4-15 shows the relative density results of the NiAl alloys sintered by SPS as a function of the milling time. All of the consolidated specimens had between 97% and 100% of theoretical density. The theoretical density (ρ_{TD}) is defined by:

$$\rho_{TD} = \frac{N_c A}{V_c N_A} \quad (4.1),$$

where N_c , A , V_c , and N_A are number of atoms in unit cell, atomic weight, volume of unit cell, and Avogadro number respectively. Some degree of porosity is inherent in most mechanically alloyed or pressure sintered materials [108]. Several studies have indicated that some of the atmospheric elements, such as Ar inserted to keep the alloying process from air contamination, were trapped into the matrix material during mechanical alloying and then preferably trapped at the surface of ODS particles during high temperature consolidation process [109, 110]. The density would be expected to increase with the milling time due to the reduction of residual void space and powder refinement, which contributes to form a high concentration of fast diffusion paths for sintering, such as grain boundaries (i.e. fine grain size), is capable of enabling the trapped gasses to diffuse to the surface as opposed to forming pores [26, 111].

4.2.2.2 Microhardness

Vickers microhardness measurement was performed to characterize the basic mechanical properties of the ODS NiAl alloy materials. Figure 4-16 shows the microhardness results of the SPSed NiAl alloys as a function of the milling time. The results can be summarized as follows: The addition of Y_2O_3 results in smaller increases in microhardness than for additions of both Y_2O_3 and Ti. The microhardness increased with increasing milling time up to 5 hrs and then saturated. The main microstructural contributions to this microhardness, or strength, of these alloys are believed to be grain refinement and particle strengthening. A quantitative relation between the microstructure and microhardness is presented in Section 4.2.2.6. This microhardness measurement method has been also used to study the thermal stability during an extensive matrix of long-term thermal annealing, which will be discussed in Chapter 5.

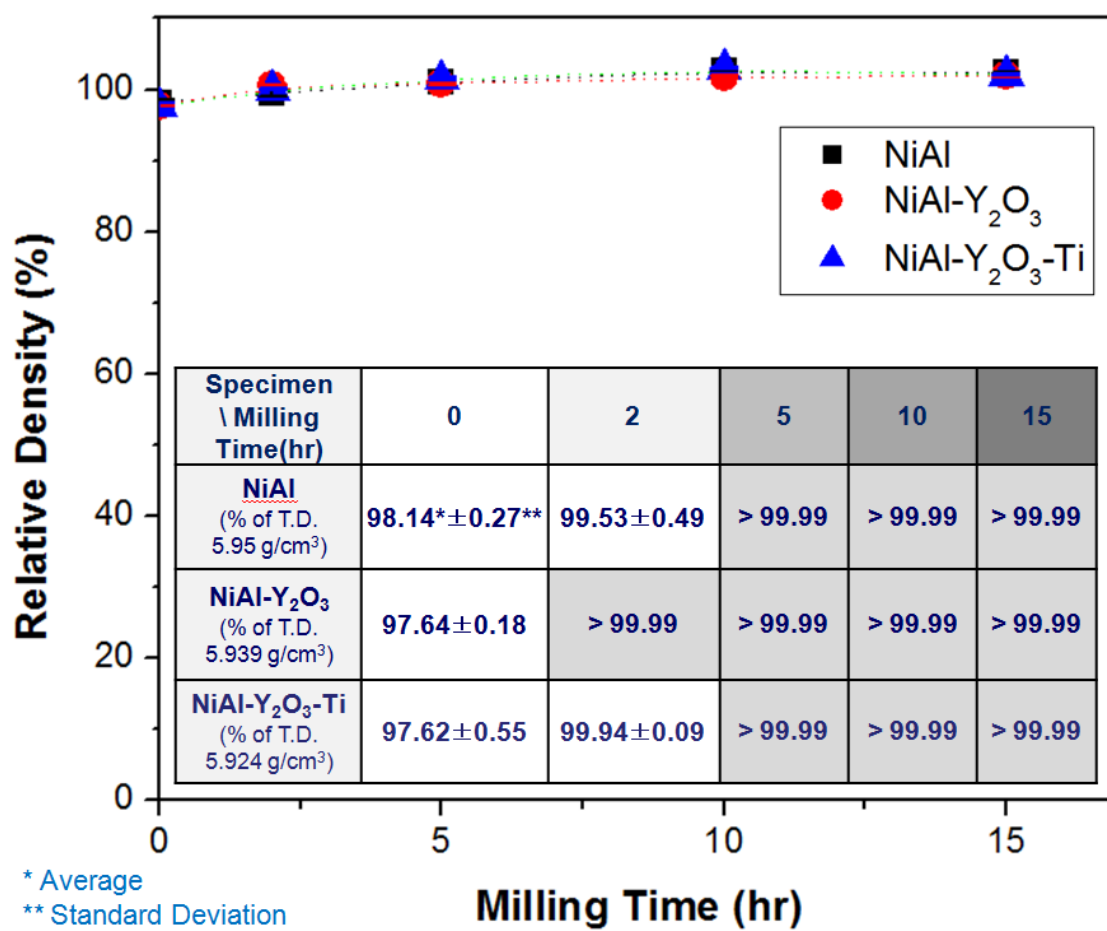


Figure 4-15. Relative density measurement results of the SPSed specimens as a function of the milling time

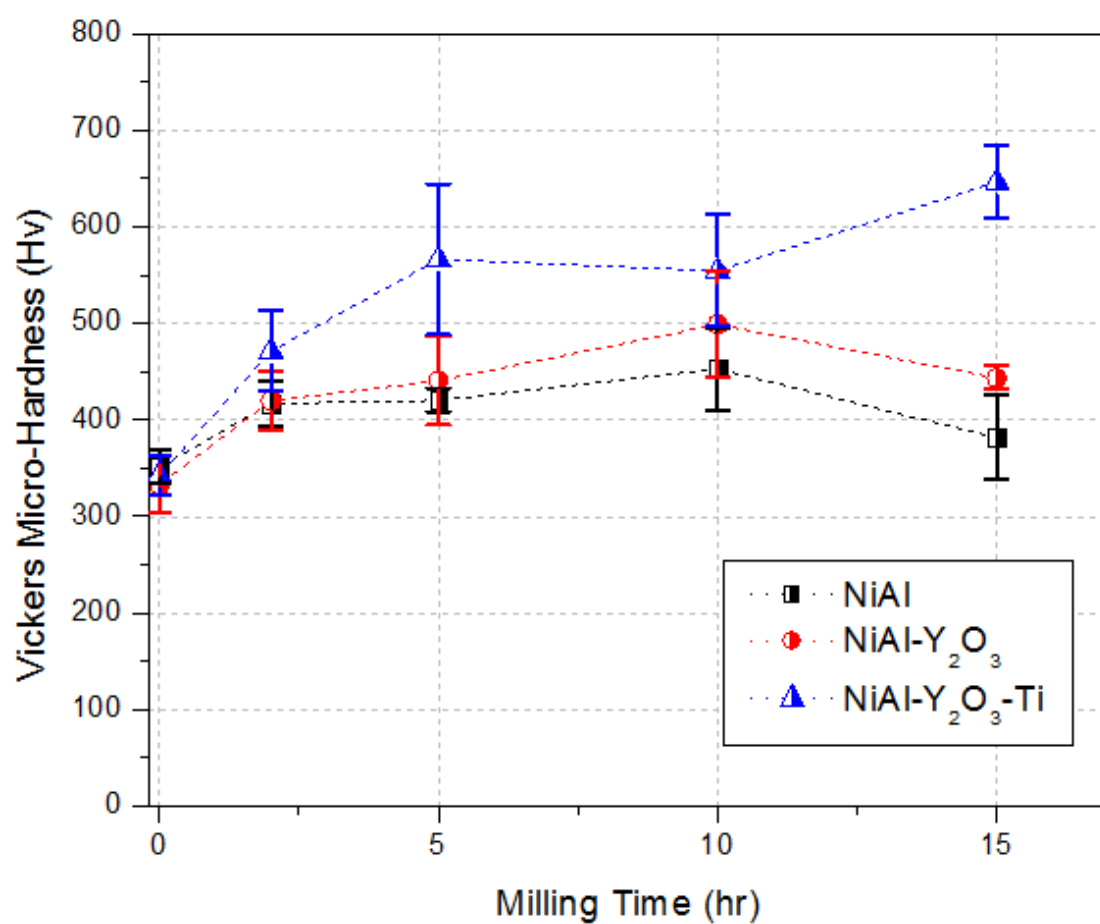
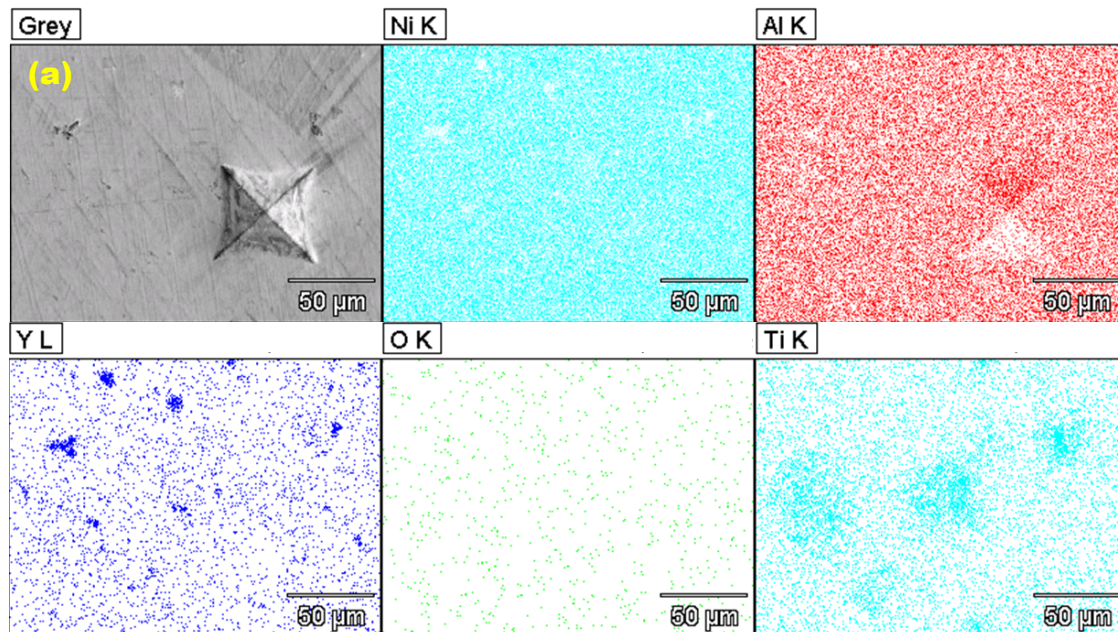


Figure 4-16. Vickers microhardness test results of the consolidated NiAl specimens as a function of milling time

4.2.2.3 Energy dispersive X-ray spectroscopy

Energy dispersive X-ray spectroscopy (EDS) elemental analysis was performed for the consolidated NiAl-1wt%Y₂O₃-1wt%Ti alloys to investigate the distribution of the alloying elements, Y₂O₃ and Ti, in the NiAl matrix with the milling time. The identified elements of Ni, Al, Y, O, and Ti were mapped from the selected region, near the location of the microhardness indentation, respectively as shown in Figure 4-17. The agglomerated particles of Y₂O₃ and Ti were clearly identified in the unmilled specimen as shown in Figure 4-17(a). After 5-10 hr ball milling, however, agglomerated particles were disappeared and all of the alloying elements were entirely distributed in the specimen region (Figure 4-17(b) and (c)). It looks like homogeneous distribution of all of the alloying elements at this micro-scale investigation, however, it has a definite limitation to be assured whether NCs are formed and uniformly distributed such a desired nm scale. Therefore, higher resolution studies by TEM and APT are performed to verify whether these milling time is appropriate for NCs formation and distribution, which is discussed in the following section.



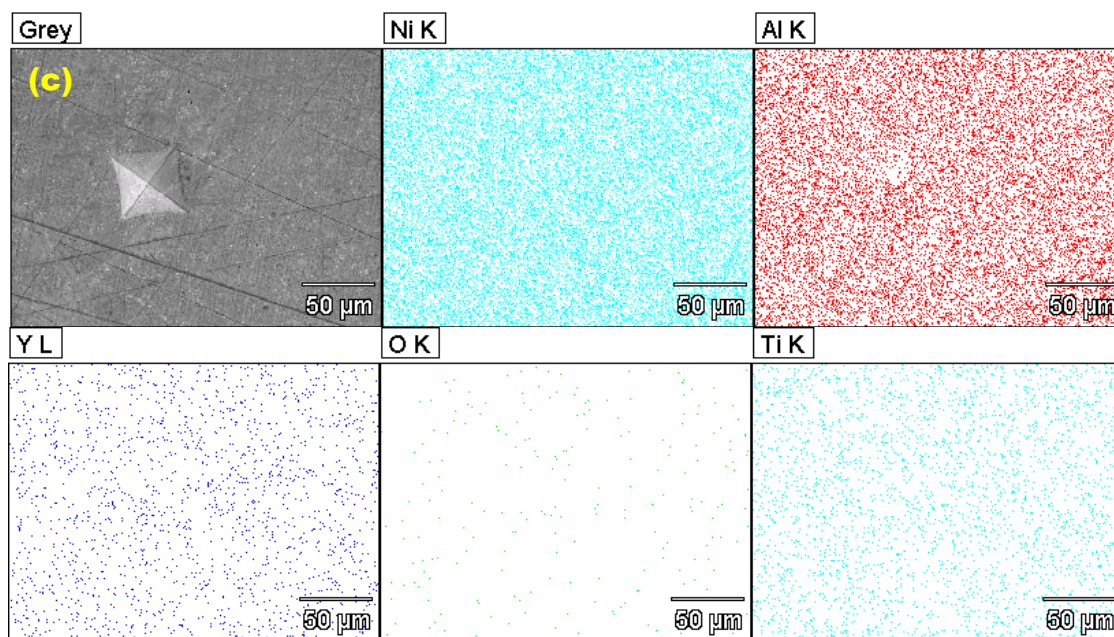
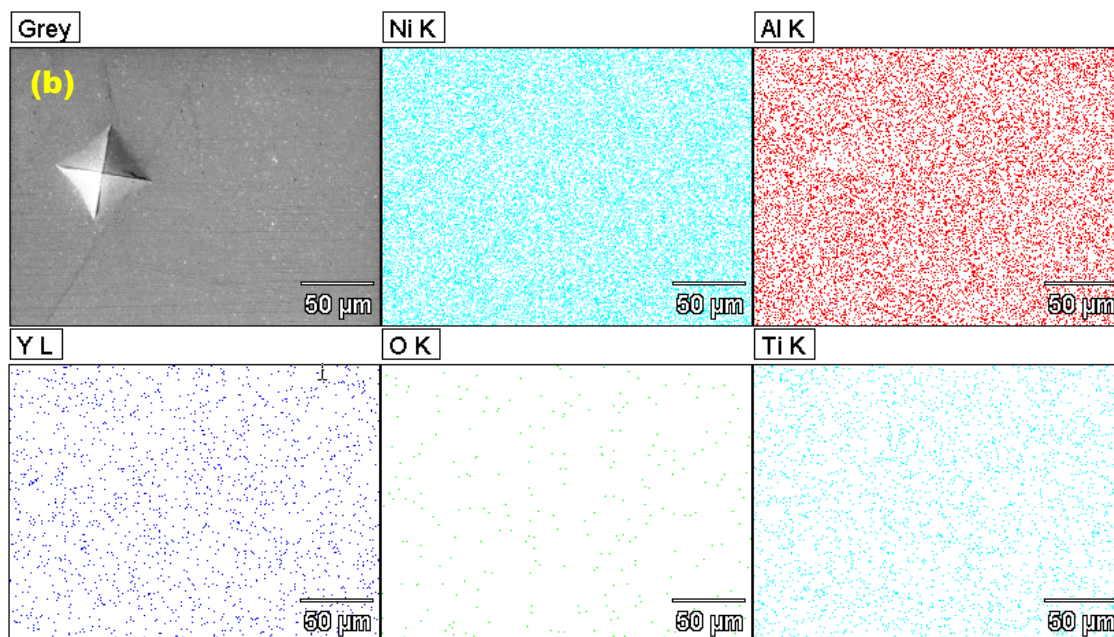


Figure 4-17. X-ray elemental(Ni, Al, Y, O, Ti) mapping of the consolidated NiAl-1wt%Y₂O₃-1wt%Ti specimen, (a) before milling (b) 5 hr milled (c) 10 hr milled

4.2.2.4 Transmission electron microscopy

TEM analysis of the as-consolidated NiAl alloys after ball milling for 10 hr was conducted to investigate the microstructure of the ODS NiAl alloys. Figure 4-18(a)-(c) shows the TEM microstructure evolution of the 10 hr milled and SPS consolidated NiAl alloys. The grain size and precipitate number density, measured by TEM, are summarized in Table 4-1. The grain size has a multimodal distribution with both fine (< 200 nm) and coarser (> 1 μ m) grain regions. The average grain size of the NiAl alloys including either Y_2O_3 or both Y_2O_3 and Ti is smaller than that of the pure NiAl alloy. The tempting conclusion is that the grain growth during the consolidation was definitely controlled by the addition of Y_2O_3 and Ti. The NiAl-1wt% Y_2O_3 and NiAl-1wt% Y_2O_3 -1wt%Ti alloys have very similar grain size distribution.

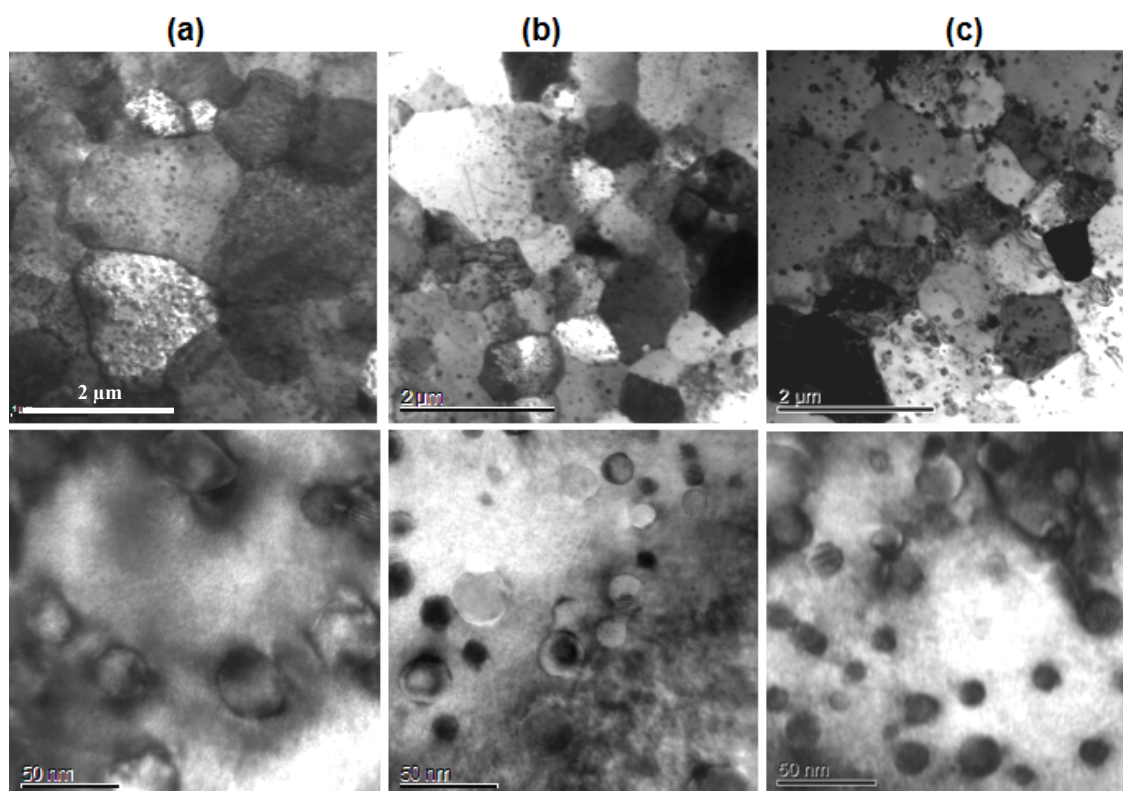
Aluminum oxide particles with sizes around 40 nm were observed in the pure NiAl alloy (Figure 4-18(a)). Precipitates of 10 to 20 nm size were distributed in both the NiAl-1wt% Y_2O_3 and NiAl-1wt% Y_2O_3 -1wt%Ti alloys (Figure 4-18(b) and (c)). The particle number densities of each alloy were $0.3 \times 10^{22}/m^3$, $0.8 \times 10^{22}/m^3$, and $1.4 \times 10^{22}/m^3$ for NiAl, NiAl-1wt% Y_2O_3 , and NiAl-1wt% Y_2O_3 -Ti respectively. Despite the high levels of strain introduced by the mechanical alloying, this TEM investigation of the consolidated NiAl alloys rarely found dislocations.

EDS measurements were used to estimate the compositions of precipitates in the NiAl alloys. Figure 4-19 and Figure 4-20 show the TEM bright field images and the estimated compositions on individual precipitates in NiAl-1wt% Y_2O_3 and NiAl-1wt% Y_2O_3 -1wt%Ti alloys, respectively. In the NiAl-1wt% Y_2O_3 , 7 out of the 10 precipitates (average diameter ≈ 15.0 nm) observed were Y-Al-O particles, so-called garnet or YAG, as shown in Figure 4-19(b) and 3 had Y-rich oxide phases. As well, it was observed that relatively large particles (~ 100.0 nm) were also garnet phases (Figure 4-19(c)). On the other hand, in the NiAl-1wt% Y_2O_3 -1wt%Ti (Figure 4-20), 18 out of the 20 precipitates (average diameter ≈ 15.0 nm) observed were similar to the garnet phase and contained no Ti (Figure 4-20(b)), and the other 2 precipitates were Ti and Al incorporated oxide phases (not shown). The large particles (~ 150.0 nm) were also found and identified as either garnet ($Y_2Al_4O_7$) or $Y_2Al_9Ti_2O_6$ phase (Figure 4-20(c)). There also appears to be a high density of smaller precipitates in the matrix of the grains with diameters less than 10 nm, however, it was very difficult to reveal the compositions of these particles because of the limitation of conventional TEM/EDS resolution.

Figure 4-21 shows TEM images (Figure 4-21(a)) and an accumulated percent of the compositions (Figure 4-21(b)), measured by EDS, corresponding to the particles present in Figure 4-21(a). A total of 8 precipitates with sizes from 16 to 200 nm in the NiAl-1wt% Y_2O_3 -1wt%Ti alloy were measured to investigate the chemical composition associated with particle size. The clear indication is that the Al composition of a particle increases as the particle size increases, and Y was dominantly found at the particles size of smaller than 50 nm while Ti was found at the relatively large particles size of larger than 100 nm. Accordingly, the Al incorporation is believed detrimental to the formation of nanoscale Y-Ti-O precipitates.

Table 4-1. Summary of the characteristics measured in the NiAl alloys

Alloy	NiAl	NiAl-Y ₂ O ₃	NiAl-Y ₂ O ₃ -Ti
Grain size (μm)	1.04 ± 0.19	0.67 ± 0.12	0.68 ± 0.11
Precipitate N (10^{22} m^{-3})	0.3	0.8	1.4
Precipitate size (nm)	30 ± 7.5	15 ± 6.6	14 ± 6.1
Microhardness(kg/mm^2)	450 ± 42	501 ± 54	550 ± 58

Figure 4-18. TEM micrographs of the as-consolidated NiAl alloys, (a) NiAl (b) NiAl-1wt%Y₂O₃ (c) NiAl-1wt%Y₂O₃-1wt%Ti

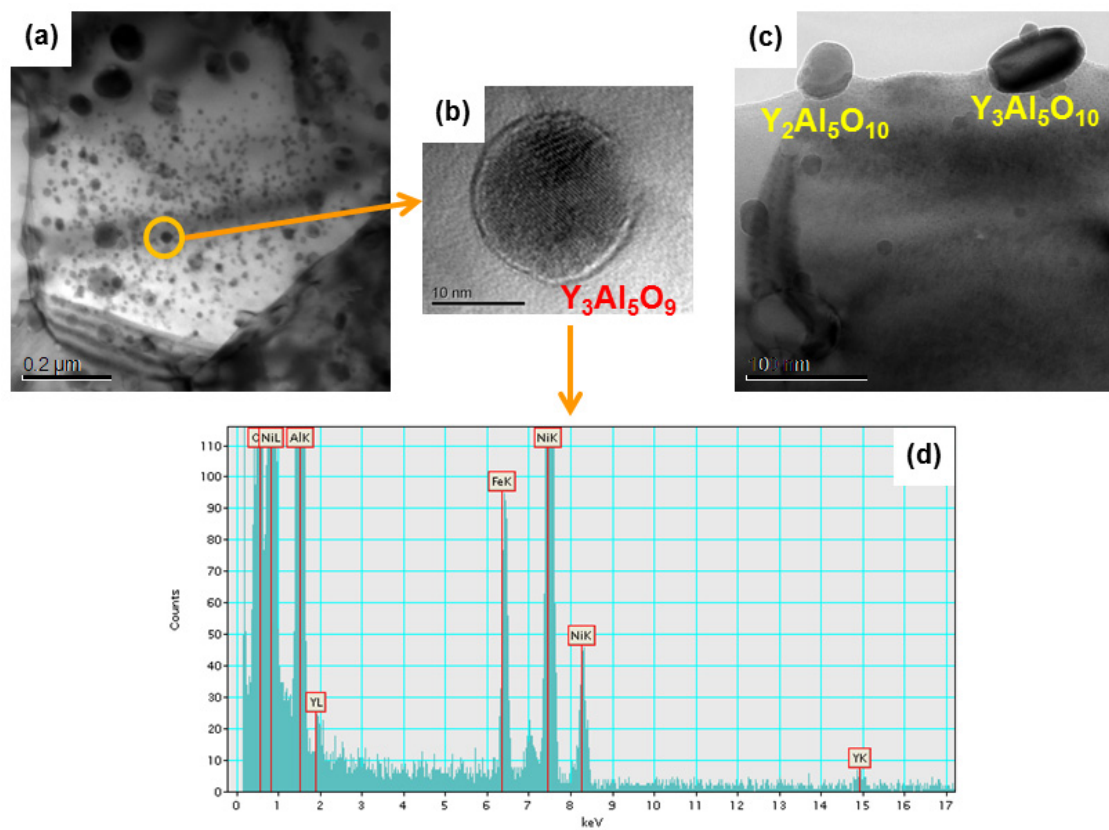


Figure 4-19. TEM bright image and compositions of the precipitates from the as-consolidated NiAl-1wt%Y₂O₃ alloy (a)-(c); EDS spectra from the precipitates marked by the arrows (d)

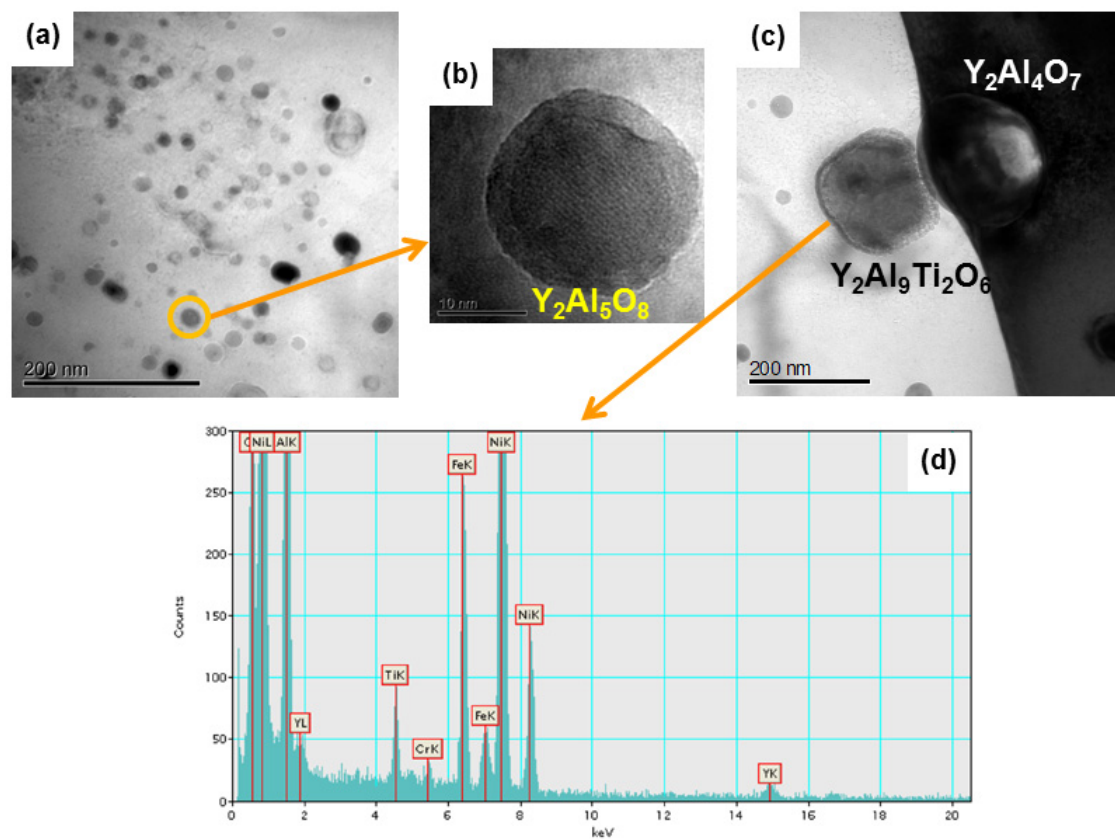


Figure 4-20. TEM bright image and compositions of the precipitates from the as-consolidated NiAl-1wt% Y_2O_3 -1wt%Ti alloy (a)-(c); EDS spectra from the precipitates marked by the arrows (d)

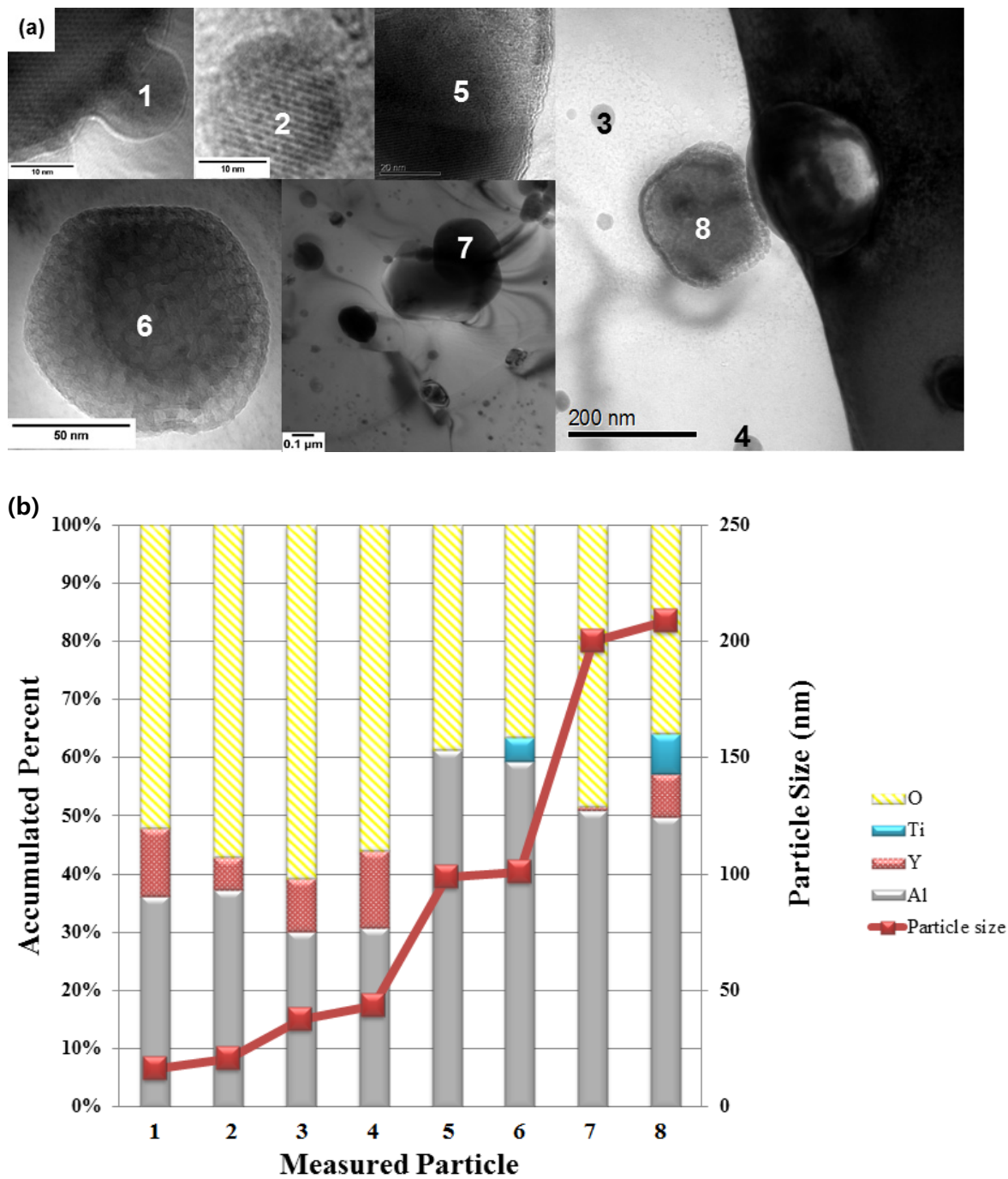


Figure 4-21. TEM image of the various precipitates from the as-consolidated NiAl-1wt%Y₂O₃-1wt%Ti alloy (a); accumulated percent of compositions in the precipitates marked by the numbers (b)

4.2.2.5 Atom probe tomography

Atom Probe Tomography (APT) was performed in collaboration with Mike Miller at ORNL and the characterization technique described in Section 3.4. Figure 4-22 shows a 3-dimensional APT map for the as-consolidated NiAl-1wt%Y₂O₃-1wt%Ti alloy. Such atom maps can provide information on the overall solute distribution as well as the size and composition of fine scale precipitates. As shown in Figure 4-22, the Ni, Al and Fe elements were homogeneously distributed. There was indication of Y-Ti-O clustering along with some heterogeneous distributions of Y, Ti, and O. Additional APT studies are needed. However, limitations of the time available on the ORNL instruments and challenges of specimen preparation for the LEAP instrument precluded more extensive APT study.

4.2.2.6 The relationship between the microhardness and microstructure

The conventional wisdom is that the strengthening in metals relates to the process of impeding dislocation movement within the lattice [112]. The major strengthening mechanisms include dislocation interactions with grain boundaries, with solute atoms, with dispersed precipitates, and with other dislocations. Therefore, it is worthwhile to assess the effective strengthening provided by these strengthening mechanisms. Although the total strength does not always follow linear superposition of individual strengthening components, the increase of yield stress ($\Delta\sigma_y$) can be expressed as the linear sum of each contribution source if the simplest linear superposition model is assumed, such as;

$$\Delta\sigma_y = \sum_i \Delta\sigma_i \quad (4.2).$$

Here each contribution source term, i , is related to: $\Delta\sigma_s$, solid-solution strengthening; $\Delta\sigma_g$, grain refinement strengthening; $\Delta\sigma_d$, strain hardening strengthening; $\Delta\sigma_p$, dispersion strengthening, and etc. Note that the assumption of the linear superposition of these various contributions to strength may not be valid in some cases and moreover complete information on all details of the microstructure, physical properties, and thorough physical models are not available. However, it is still useful to qualitatively, if not semi-quantitatively assess these strengthening terms.

$\Delta\sigma_s$ – Weak or negligible if all the solutes are assumed to be precipitated during the high temperature consolidation process. Not known if the Fe solutes from contamination (discussed in Chapter 2) contribute to the solid-solution strengthening.

$\Delta\sigma_g$ – Take $\Delta\sigma_g = k/\sqrt{d}$ based on the well-known Hall-Petch equation where k is a constant and d is the grain size. For the k (0.2~0.5 depending on grain size) and d (0.67~1.04 μm from Table 4-1), $\Delta\sigma_g = 196\sim610$ MPa.

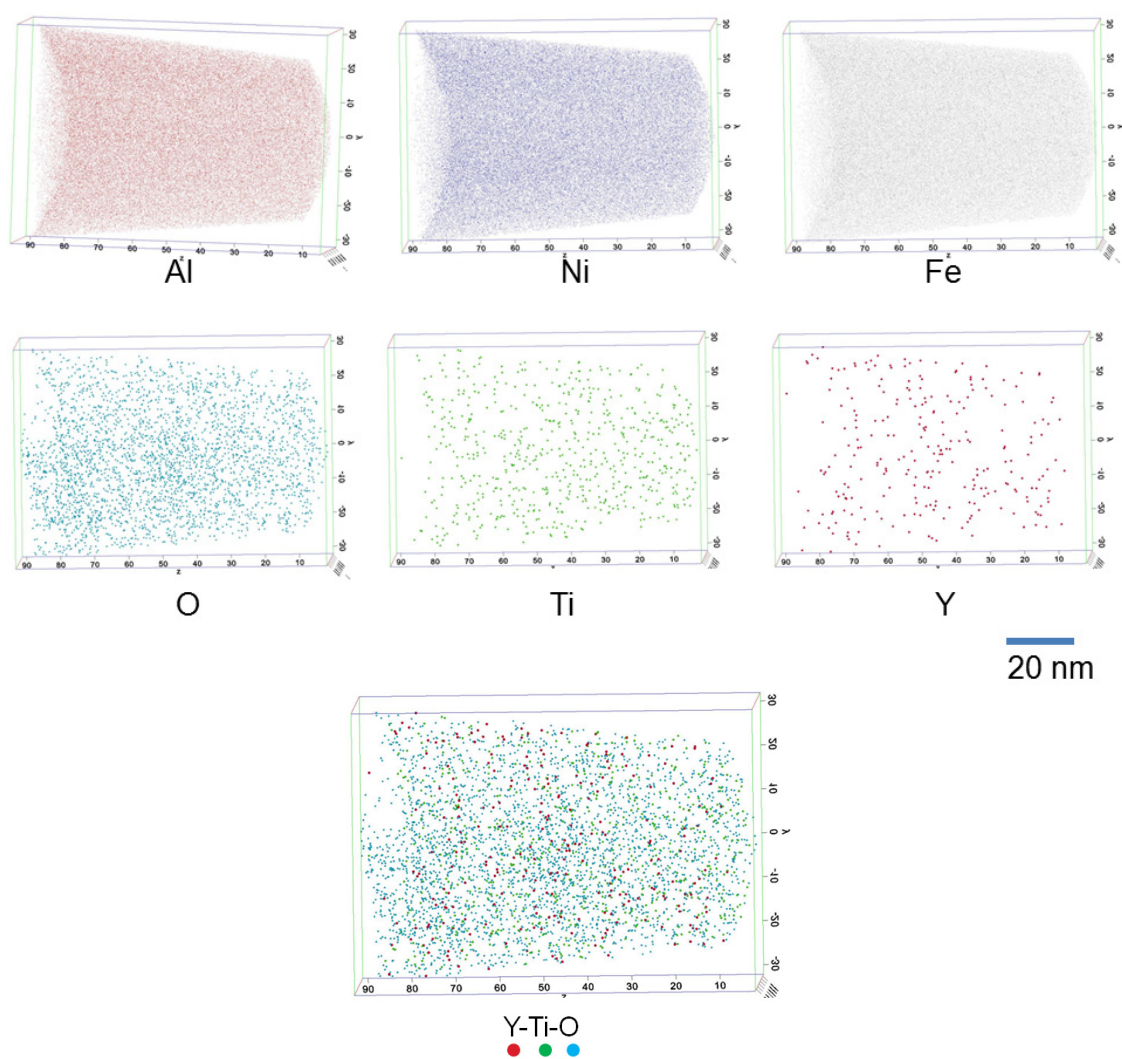


Figure 4-22. Atom probe tomography images of Al, Ni, Fe, Y, Ti, and O that were observed in the as-consolidated NiAl-1wt%Y₂O₃-1wt%Ti alloy

$\Delta\sigma_d$ – Take $\Delta\sigma_d \approx 1.2Gb\sqrt{\rho}$ where G is the shear modulus (~ 71.5 GPa), b is the magnitude of Burgers vector (~ 0.288 nm), and ρ is the dislocation density. If the dislocation density is $\sim 4.1 \times 10^{14}/\text{m}^2$ (estimated by XRD for the as-consolidated conditions) then $\Delta\sigma_d \approx 500$ MPa.

$\Delta\sigma_p$ – Take $\Delta\sigma_p = \alpha M G b / \lambda \approx \alpha M G b \sqrt{n} D$ based on the Orowan model, where α is the constant (0.2~1) that may depend on particle size, M is the Taylor factor (~ 3.06), λ is the effective interparticle distance, n is the particle number density, and D is the precipitate size. For the particle number densities (n) ranging from 0.3×10^{22} to 1.4×10^{22} from Table 4-1 and the precipitate size (D), measured by TEM, ranging from 14 to 30 nm, $\Delta\sigma_p = 81 \sim 1291$ MPa.

In addition, the Vickers microhardness value discussed in Chapter 3.5, equation (3.4) can be rewritten as;

$$\Delta\sigma_y \approx \frac{\Delta H_v}{3} \quad (4.3).$$

Focused on the major contributions of the alloy dependent strengthening components, namely the grain refinement and dispersion strengthening, the microhardness data discussed in Section 4.2.2.2 were evaluated based on the data from the TEM microstructural characterization discussed in Section 4.2.2.4. Table 4-2 represents the summary of the contributing strengthening components and the microhardness value assessment between the NiAl alloys. To reduce the uncertainty of various constants, each strengthening term was calculated and represented with the relative value to that of the NiAl. The results can be summarized as follows:

- Based on the grain refinement strengthening, the indication is that the yield stress increase ($\Delta\sigma_g$) in both NiAl-1wt%Y₂O₃-Y₂O₃(alloy ②) and NiAl-1wt%Y₂O₃-1wt%Ti (alloy ③) are about 24% higher strengthening effect than that of NiAl (alloy ①). The difference of the grain refinement strengthening between the alloy ② and ③ is negligible.
- From the Orowan model, the yield stress increase ($\Delta\sigma_p$) in the alloy ② was estimated as 15% higher than alloy ①, while the alloy ③ was about 47% higher than alloy ①. The ratio of precipitate strengthening in alloy ③ to ② is approximately 1.28.
- By equation (4.3), the increase of Vickers microhardness is linearly proportional to the increase of yield stress.
- But, the increase of the microhardness between the alloy ① and ②, $\Delta H_{②-①}$, is 51 while that of between the alloy ① and ③, $\Delta H_{③-①}$, is 100. The increase ratio of the alloy ③ to ② is 2, which is not consistent with the Orowan model strengthening estimation if we neglect the grain refinement strengthening contribution.

- As far as the average microhardness values are concerned, assuming that each alloy has its own consistent microstructure for the saturated period of time (5-15 hrs), it makes the difference between the Orowan model strengthening and the increase of the microhardness even bigger (the increase ratio of the alloy ③ to ② is 3.7) as represented in Table 4-2.

It appears that alloy ③ definitely received a strengthening benefit from the Ti addition, although the microstructural characterization results cannot be fully rationalized with the microhardness data of the observed precipitate distributions. This raises the question of whether small Y-Ti-O clusters observed in APT could provide sufficient contribution the strengthening of the alloy. Since the conventional TEM has a resolution limitation for identifying the presumable small particles, a higher resolution study along with additional Atom Probe Tomography is required for further microstructure research.

Table 4-2. The summary of strengthening components and the microhardness value assessment

	$\frac{1}{\sqrt{d}}$ [nm ^{-1/2}]	$\frac{\Delta\sigma_g}{\Delta\sigma_g^{①}}$	n [# / m ³]	D [nm]	$\frac{\Delta\sigma_p}{\Delta\sigma_p^{①}}$	$H_{v,10h}$ ($\langle H_v \rangle$)	$\Delta H_{v,10h}$ ($\langle \Delta H_v \rangle$)	$\frac{\Delta H_{v,10h}^{③}}{\Delta H_{v,10h}^{②}} \left(\frac{\langle \Delta H_v^{③} \rangle}{\langle \Delta H_v^{②} \rangle} \right)$
① NiAl	3.10E-2	1.00	0.3E+22	30±7.5	1.00	450(417)	$\left. \begin{array}{l} 51 \\ (46) \end{array} \right\} 100 \\ (173)$	2 (3.7)
② NiAl-Y ₂ O ₃	3.86E-2	1.24	0.8E+22	15±6.6	1.15	501(463)		
③ (NiAl-Y ₂ O ₃ -Ti)	3.82E-2	1.23	1.4E+22	14±6.1	1.47	550(590)		

$\langle \Delta H_v \rangle$: Average microhardness for 5-15 hrs milling conditions

4.3 Summary and discussion

In this chapter, the results of microstructural characterization along with microhardness measurement in the mechanically alloyed and as-consolidated alloys were discussed.

For Fe-Cr based 14YWT alloys, EPMA, EDS, TEM, and APT results demonstrated that milling for 40 hr provided sufficient milling to obtain a uniform distribution of Y and Ti in the alloy for 14YWT. In addition, the effect of decreased O content caused by process modification was discussed.

For ODS NiAl alloys, the key observations can be summarized as followings:

- There was a clear indication that milling for 5-15 hrs was sufficient to produce good mixing during the mechanical alloying process, as determined by XRD, SEM, and EDS results.
- Powder consolidation was carried out by spark plasma sintering (SPS), as described in Chapter 2. Fully dense NiAl alloy materials were produced by SPS.

- Grain size for the consolidated alloys was characterized by TEM.
- A distribution of 10-20 nm precipitates was found in NiAl-Y₂O₃ and NiAl-Y₂O₃-Ti alloys, and those precipitates were identified as Y-Al-O (garnet) particles in the NiAl-Y₂O₃, while both garnet (Y₂Al₄O₇) and Y₂Al₉Ti₂O₆ phase particles were found at the NiAl-Y₂O₃-Ti alloy.
- The Al composition of a particle increases as the particle size increases, and Y was dominantly found at the particles size of less than 50 nm while Ti was found at the relatively larger particles with size larger than 100 nm. The Al incorporation believed detrimental to the formation of nanoscale Y-Ti-O precipitates.
- The effect of Hall-Petch grain size and dispersion strengthening mechanisms in ODS NiAl alloys were semi-quantatively assessed.
- The strength assessment based on the microstructure of the ODS NiAl alloys could not fully rationalize the microhardness data of the observed precipitate distributions. The outstanding question was raised whether small Y-Ti-O clusters observed in APT could provide sufficient contribution the strengthening of the alloy.

Chapter 5

Thermal Stability of Nano Oxide Precipitates and Grain Growth Kinetics

The results of microstructural characterization of the as-milled powders and the consolidated alloys were discussed in Chapter 4. Some indication of nanoscale oxide precipitates was observed in the consolidated alloys, along with larger Y-Al-Ti oxide precipitates. Notably, the combination of grain size refinement and larger oxide precipitate dispersion was unable to fully explain the increase in strength of the NiAl-Y₂O₃-Ti alloy relative to NiAl. This further supports the possibility of the presence of nm-sized Y-Ti-O precipitates. This chapter presents an investigation on the thermal annealing behavior of the ODS NiAl alloys. Thermal stability of the nanosize precipitates and the grain size, as well as the mechanical properties have been studied following high temperature isothermal annealing. The Orowan strengthening effect on thermal annealed ODS NiAl alloys has been studied with particle size and number density, measured by TEM, along with microhardness data. The relationship between the grain size and the microhardness has been assessed to derive the effective Hall-Petch strengthening component. Finally, grain growth kinetics for the ODS NiAl were studied by TEM microstructure characterization associated with the annealing temperature and time.

5.1 Thermal annealing

The thermal annealing was performed for the 10 hr ball milled and SPS consolidated NiAl alloys in an alumina tube using a CM Inc. High Temperature Furnace. The ends of the tube were fitted with inlet and outlet purified Ar gas flow tubes. An oxygen analyzer was incorporated at the exit end to monitor the oxygen contamination during the thermal annealing. The tube was evacuated and back-filled with Ar gas to eliminate oxygen environment. In addition, the annealing specimens were wrapped with Niobium thin (0.01 mm) foil to serve as an oxygen getter to minimize the specimen oxidation. The heating rate was 10°C/min to prevent the alumina tube from cracking. Extensive thermal annealing was carried out for 500 hr at selected constant temperatures of 1433, 1626, and

1723K, which correspond to 75, 85, and 90% of the NiAl melting temperature (1914K) respectively. Table 5-1 describes the annealing study matrix.

Table 5-1. Temperatures and times for annealing study

Temp(K) \ hrs	5	10	20	50	100	200	500
1433 (0.75 T_m)	○	○	○	○	○	○	○
1626 (0.85 T_m)	○	○	○	○	○	○	○
1723(0.90 T_m)	○	○	○	○	○		

5.2 Microstructure evolution during thermal annealing

Figure 5-1 shows the microstructure evolution during annealing the NiAl and NiAl-Y₂O₃-Ti alloys at 1626K respectively, starting with the as-consolidated condition. In the as-consolidated condition (Figure 5-1(a) and (b)), the NiAl alloy showed average size of 1.04 μm grains with about 30 nm aluminum oxide particles while the NiAl-Y₂O₃-Ti alloy showed average size of 0.68 μm grains with about 14 nm Y-Al-(Ti)-O oxide particles (as discussed in Section 4.2.2.4). Figure 5-1(b) and (d) compare the structure of the NiAl and NiAl-Y₂O₃-Ti alloys, after annealing at 1626K for 20 hr. There was an increase in the particle size upon annealing the NiAl alloy as shown in Figure 5-1(b). In contrast, it appears that nanosized (~ 15 nm) oxide particles still existed within the matrix grain, in addition to coarsened aluminum oxide particles in the NiAl-Y₂O₃-Ti alloy (Figure 5-1(d)). In both cases, the annealing at 1626K for 20 hr led to grain growth, up to > 2 μm .

The TEM microstructure of the NiAl-Y₂O₃-Ti alloy annealed at 1433K for 20 hr and 200 hr is shown in Figure 5-2(a) and (b) respectively. The grain growth was very effectively inhibited even after 200 hr at 1433K. There was a steady increase in the size of the aluminum oxide particles while the nanosized particles showed a relatively high thermal stability to resist changes in size upon annealing at 1433K. Table 5-2 describes the grain and particle sizes for each annealing temperature and time for the ODS NiAl alloys.

Figure 5-3 shows TEM microstructure evolution in the NiAl-Y₂O₃-Ti alloy after 100 hr, 200 hr, and 500 hr at 1626K (Figure 5-3(a)-(c)) and after 100 hr at 1723K (Figure 5-3(d)). An average grain size of the NiAl-Y₂O₃-Ti alloy after 100 hr, 200 hr, and 500 hr at 1626K was estimated to 2.04, 2.74, and 3.91 μm , while an average particle size of the NiAl-Y₂O₃-Ti alloy during the corresponding annealing condition was 156, 224, and 255 nm respectively. On the other hand, a particle number density of the NiAl-Y₂O₃-Ti alloy annealed at 1626K for 100 hr, 200 hr, and 500 hr, as described in Table 5-3, was 0.30E+20, 0.26E+20, and 0.17E+20 m^{-3} . It indicates that the particle number density

decreases as the average particle size increases, which implies that the particle growth diffusion process follows the thermodynamically-driven Ostwald Ripening mechanism [113]. The bimodal particle size distribution was also observed in the microstructure of the NiAl-Y₂O₃-Ti alloy during annealing at 1626K and 1723K as shown in Figure 5-3. Further, there was evidence of the presence of precipitated Ar gas in the TEM microstructure, especially shown in Figure 5-3(c), which is believed that the Ar gas was trapped into the NiAl matrix during the mechanical alloying and then precipitated during high temperature process such as consolidation and thermal annealing.

A plot of the grain size versus particle size (Figure 5-4) in the NiAl-Y₂O₃-Ti alloy reveals that the grain size increases as the particle size increases and shows a much steeper increase during the annealing at 1626K than during annealing at 1433K. The evolution of grain size and particle size in the NiAl-Y₂O₃-Ti alloy as a function of annealing time at 1626K has been plotted in Figure 5-5(a) and (b) respectively, which shows a steady increase in both values with increasing annealing time. There are wide variations in the results of the particle size (shown in Table 5-2 and Figure 5-5(b)) caused by bimodal particle size distribution in the microstructure.

Figure 5-6 shows TEM images (Figure 5-6(a)) of the NiAl-Y₂O₃-Ti alloy after 20 hr at 1433K and an assessment of the precipitate compositions (Figure 5-6(b)) corresponding to the particles present in Figure 5-6(a). A total of 5 precipitates sizes from 10 to 75 nm were measured to investigate the chemical composition as a function of particle size. It was revealed that the Al was rarely found at small oxide particles (size smaller than 30 nm) while Y was dominantly found at this small particle size. In contrast, Al dominantly exists in coarser oxide particles (size larger than 40 nm) and Al composition of a particle increases as the particle size increases, which showed a similar tendency as we have discussed about the chemical composition of as-consolidated alloys in Section 4.2.2.4. It was not able to detect Ti element during the EDS study, on the other hand, a STEM (Scanning TEM) with Electron Energy Loss Spectroscopy (EELS) characterization could detect the Ti elements in several particles as shown in Figure 5-7. However, quantitative assessment data for the Ti composition in the particles is not available.

Table 5-2. Evolution of average particle size and grain size as a function of annealing temperature and time

Alloy	Temperature (K)	Annealing time (hr)	Particle size (nm)	Grain size (nm)
NiAl	1626	As-consolidated	30 ± 7.5	1510 ± 520
		20	305 ± 104	2150 ± 570
		100	450 ± 120	6130 ± 930
NiAl-Y ₂ O ₃	1433	As-consolidated	15 ± 6.6	670 ± 120
		200	18 ± 6.4	970 ± 230
NiAl-Y ₂ O ₃ -Ti	1433	As-consolidated	14 ± 6.1	680 ± 110
		5	12 ± 11	770 ± 230
		20	28 ± 27	780 ± 220
		200	41 ± 16	840 ± 70
	1626	5	112 ± 97	1110 ± 200
		20	121 ± 152	1700 ± 230
		100	156 ± 169	2040 ± 280
		200	224 ± 229	2740 ± 550
		500	255 ± 227	3910 ± 290

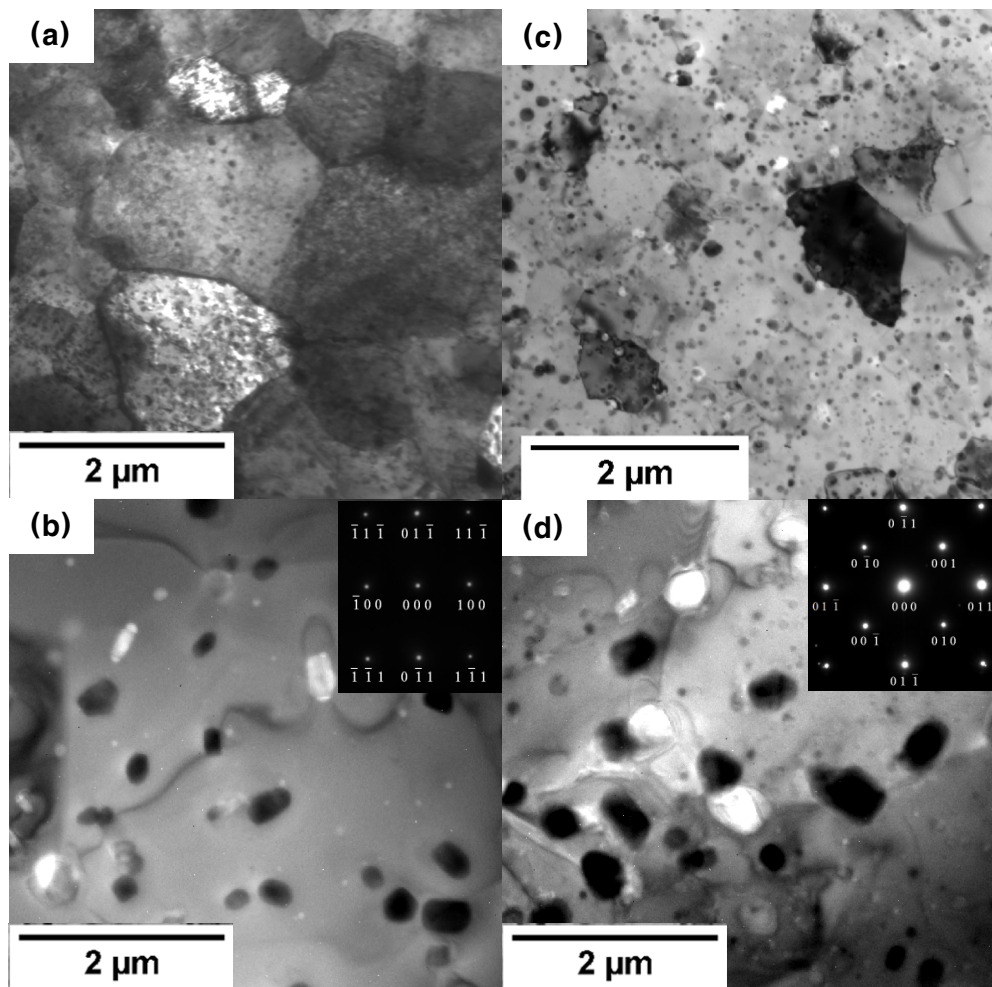


Figure 5-1. Microstructure evolution in (a, b) NiAl and (c, d) NiAl-Y₂O₃-Ti, as-consolidated, after 20 hr at 1626K, respectively, showing grains and oxide particle

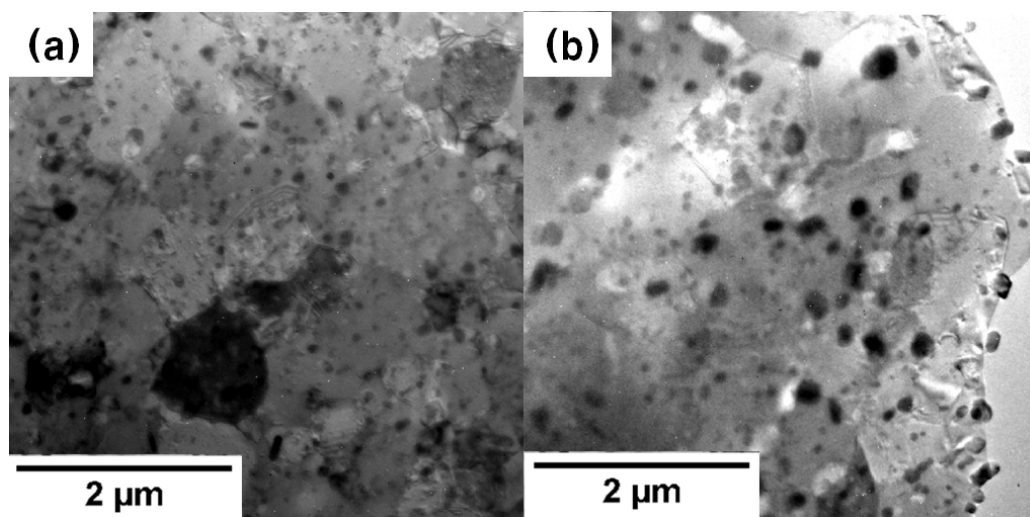


Figure 5-2. Microstructure evolution in NiAl-Y₂O₃-Ti (a) after 20 hr (b) after 200 hr at 1433K

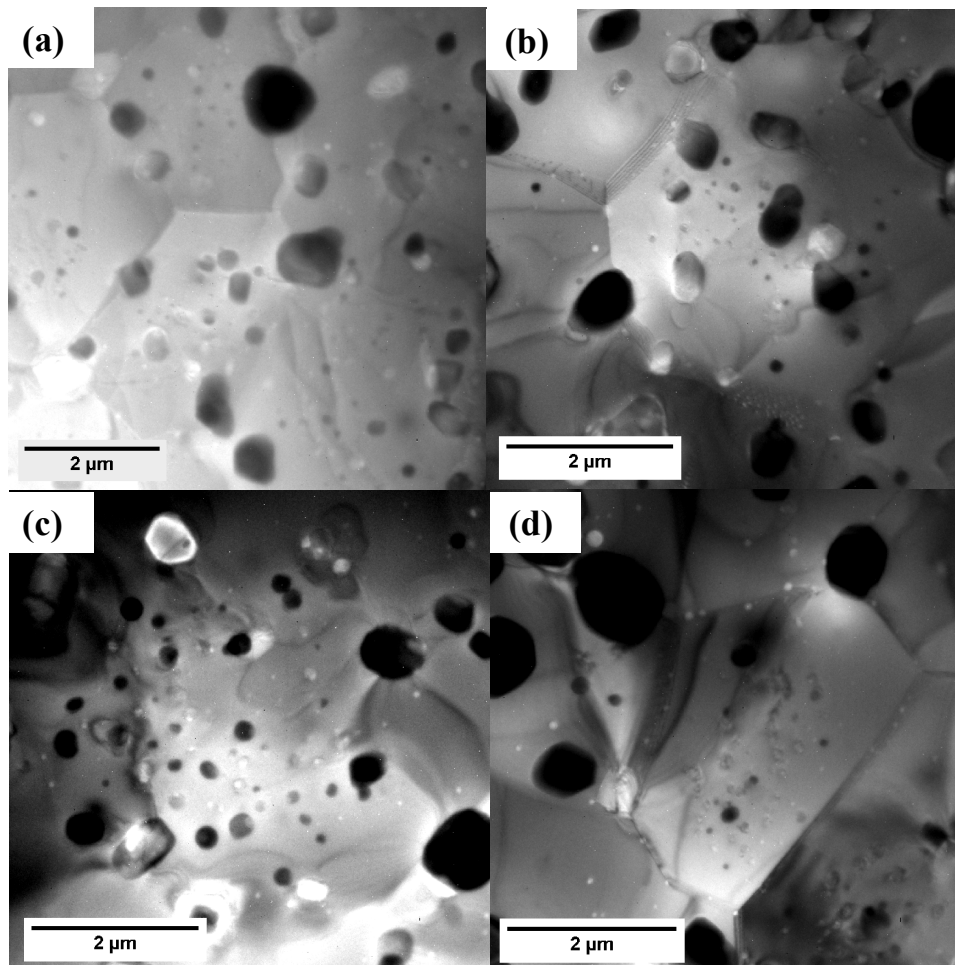


Figure 5-3. Microstructure evolution in NiAl-Y₂O₃-Ti after 100 hr, 200 hr, and 500 hr at 1626K (a)-(c); after 100 hr at 1723K (d)

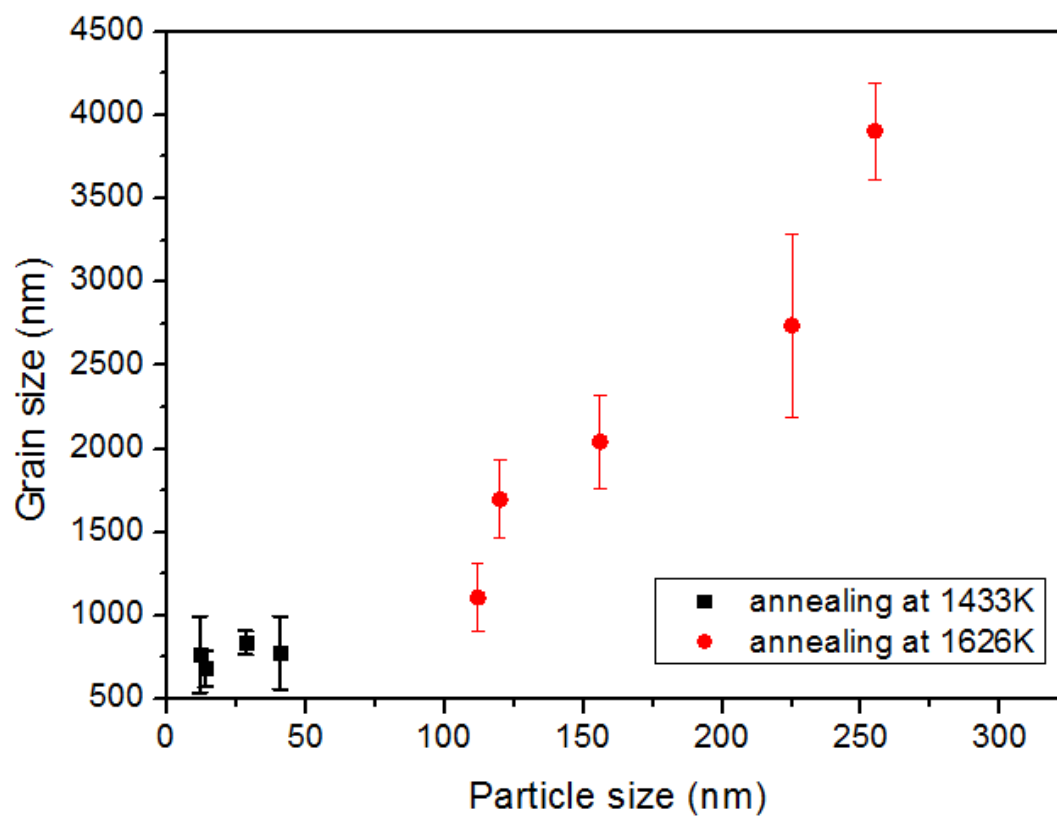


Figure 5-4. A plot between grain size and particle size in NiAl-Y₂O₃-Ti

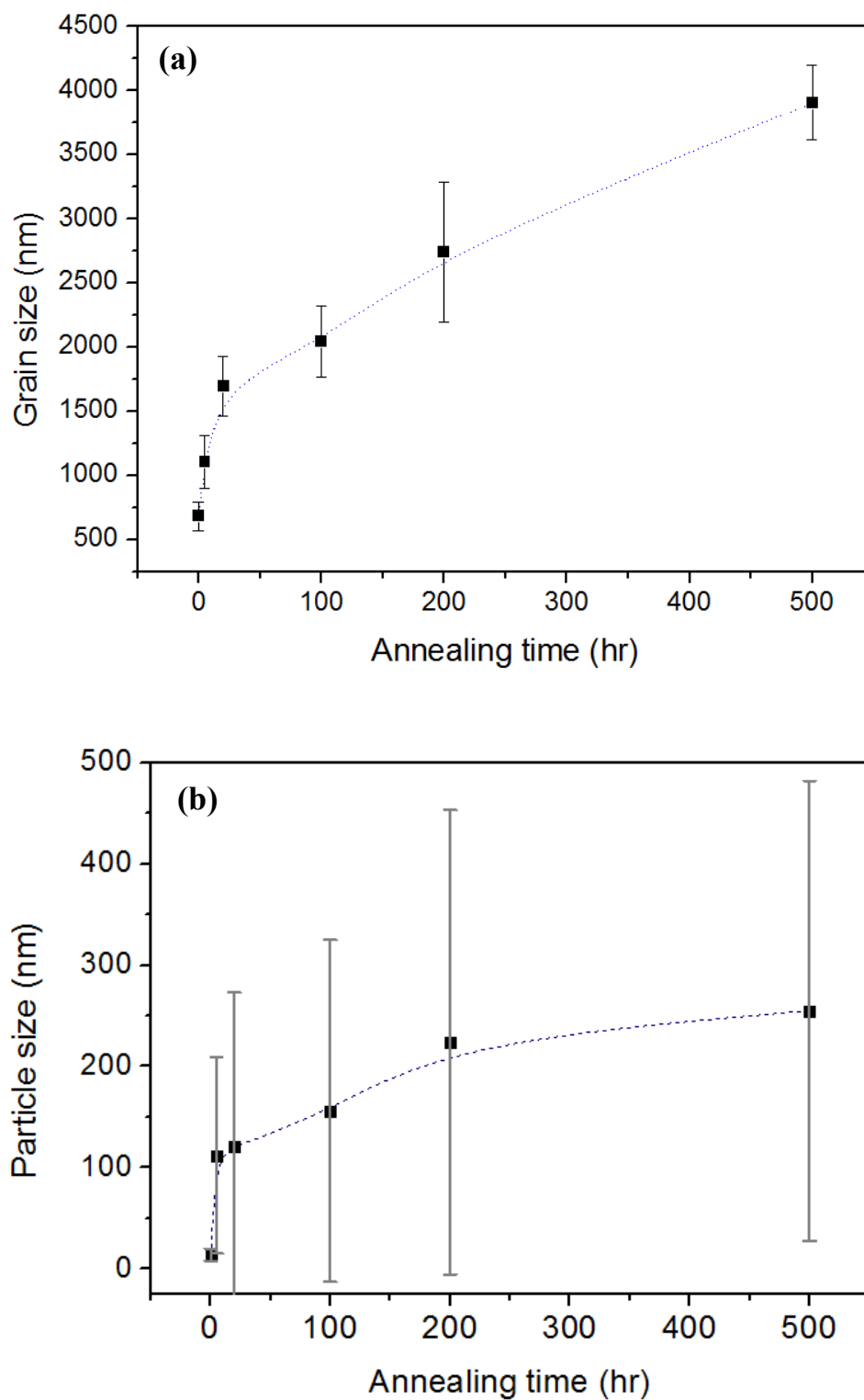


Figure 5-5. Evolution of: (a) grain size and (b) particle size in NiAl-Y₂O₃-Ti as a function of annealing time at 1626K

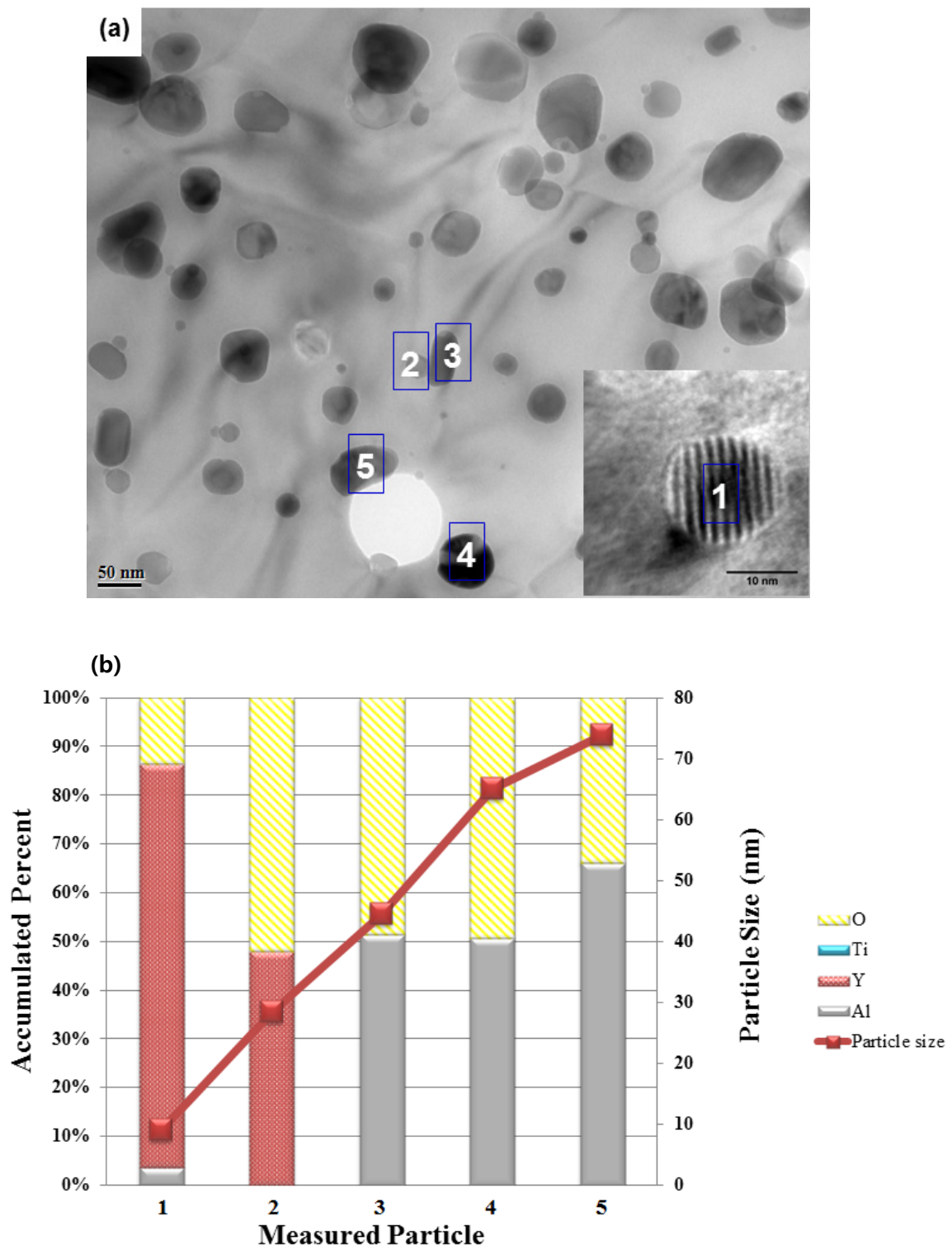


Figure 5-6. TEM image of the precipitates from NiAl-Y₂O₃-Ti alloy after 20 hr at 1433K (a); accumulated percent of compositions in the precipitates marked by the numbers (b)

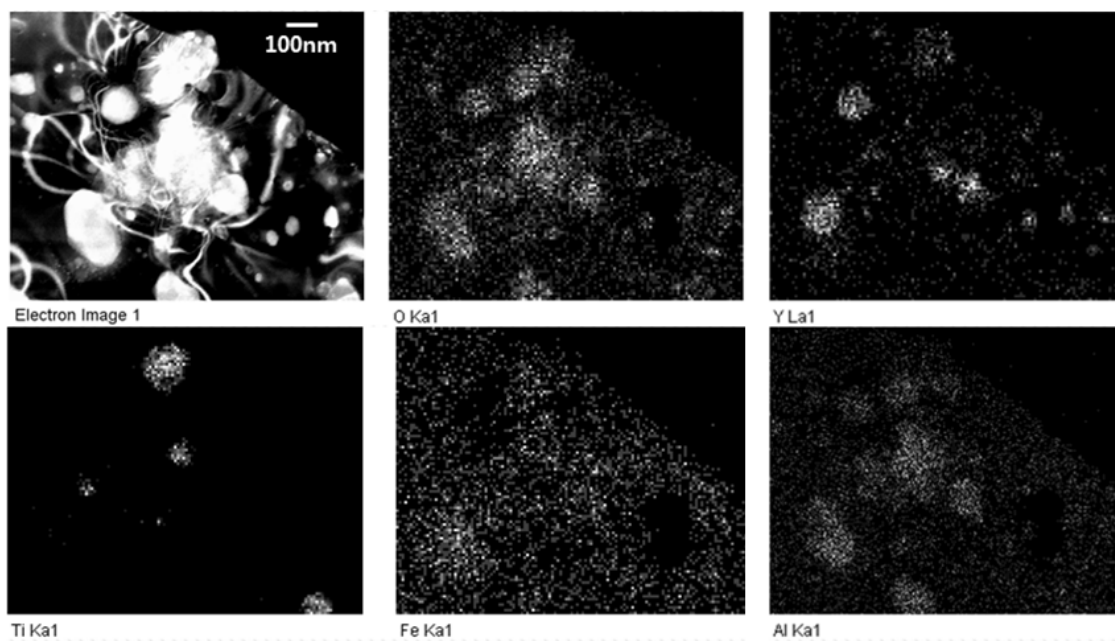


Figure 5-7. Elements (O, Y, Ti, Fe, Al) mapping of the NiAl-Y₂O₃-Ti alloy after 20 hr at 1433K by STEM EELS characterization

5.3 Variation of microhardness with annealing conditions

The evolution of average microhardness values as a function of annealing time at 1433, 1626, and 1723K is presented in Figure 5-8 to Figure 5-10. The NiAl-Y₂O₃-Ti alloy material has the highest microhardness value among the ODS NiAl alloys and persisted through thermal annealing for 500 hrs at 1433K and 1626K as well as for 100 hrs at 1723K. A large decrease in microhardness occurred at the beginning of the annealing time and then saturated during the annealing at 1626 and 1723K. However, during the annealing at 1433K, no significant decrease in microhardness value was observed through the long term (up to 500 hrs) annealing compared to the as-consolidated microhardness value. The very limited grain and particle growth discussed in Section 5.2 are believed to contribute to the decrease in microhardness (strength) of the alloy.

There is one feature of Figure 5-8 and Figure 5-9 that should be noted. All of the NiAl alloys show a consistent trend of initial increase in microhardness, at annealing temperatures of 1433 and 1626K. From the precipitation (Orowan) strengthening point of view, the additional precipitation during the early stage of time is believed as one possible contribution to this microhardness increase. From the grain boundary (Hall-Petch) strengthening point of view, an idea of “non-equilibrium” grain boundaries is introduced to explain the initial increase in microhardness. It was suggested that the grain boundary is not clearly defined, namely, non-equilibrium grain boundaries, in as-fabricated conditions as well as in submicrometer grain size alloys produced by intense plastic deformation [114, 115]. Furukawa et al. [114] state that “Plastic flow occurs when the microhardness indenter impinges on the specimen surface and non-equilibrium grain boundaries may be essentially transparent to the movement of mobile lattice dislocations”. Notably, Furukawa [114] pointed out that static annealing led to evolution of the grain boundaries into an equilibrium condition, thereby leading to an initial increase in microhardness, which is believed as another possible explanation for the initial increase in microhardness of the NiAl alloys at annealing temperatures of 1433 and 1626K.

In Figure 5-11, the graphs show the variation of microhardness with grain size (Figure 5-11(a)) and particle size (Figure 5-11(b)). It is observed that microhardness has a decreasing trend with increasing grain and particle sizes, as expected. The variation of microhardness with annealing time showed a reverse trend to the evolution of grain and particle sizes with annealing time, namely, decreasing hardness with increases in time and temperature as shown in Figure 5-8 to Figure 5-10. This indicates that both grain refinement (Hall-Petch) and dispersion (Orowan) strengthening are effective in tandem although it is not clear which of these two mechanisms is the dominant strengthening mechanism in the ODS NiAl alloys. Further analysis on these contributions to strengthening would be informative to estimate each contribution, therefore, it will be discussed the Orowan strengthening derived from microhardness along with particle size and number density and Hall-Petch strengthening derived from relationship between microhardness and grain sizes associated with thermal annealing in Section 5.4 and 5.5 respectively.

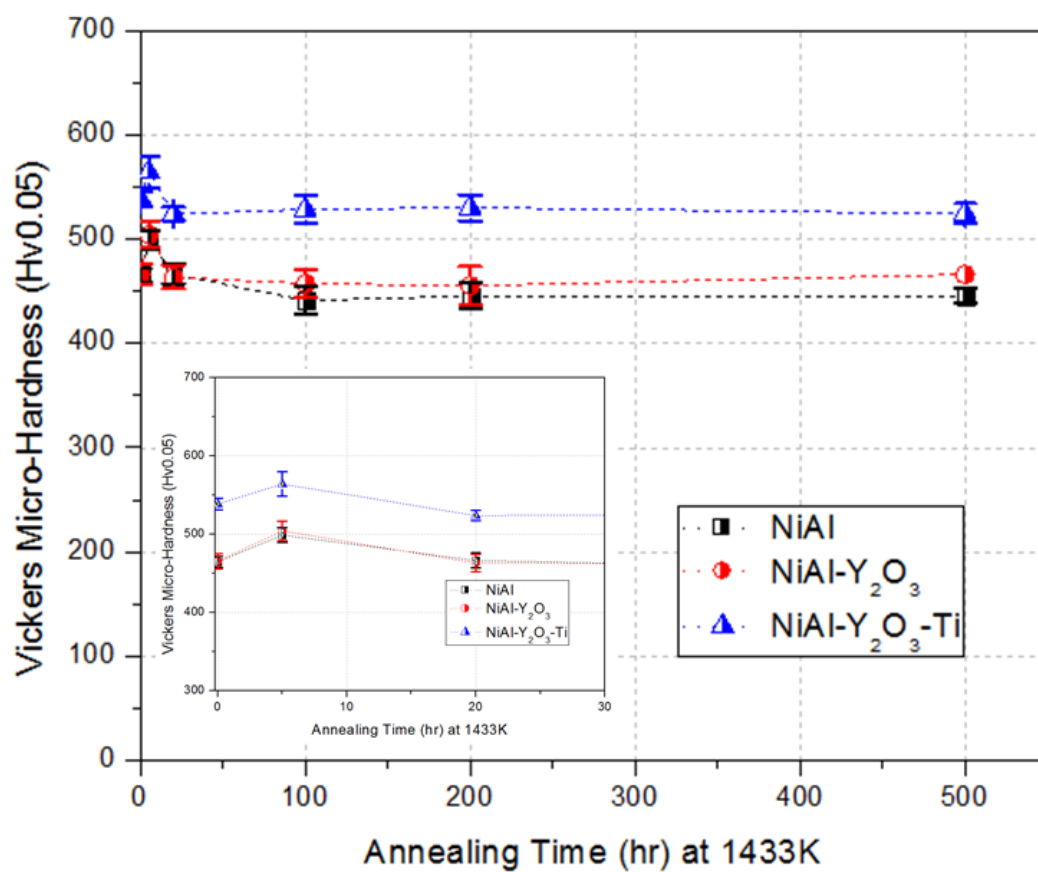


Figure 5-8. Evolution of microhardness with annealing time at 1433K

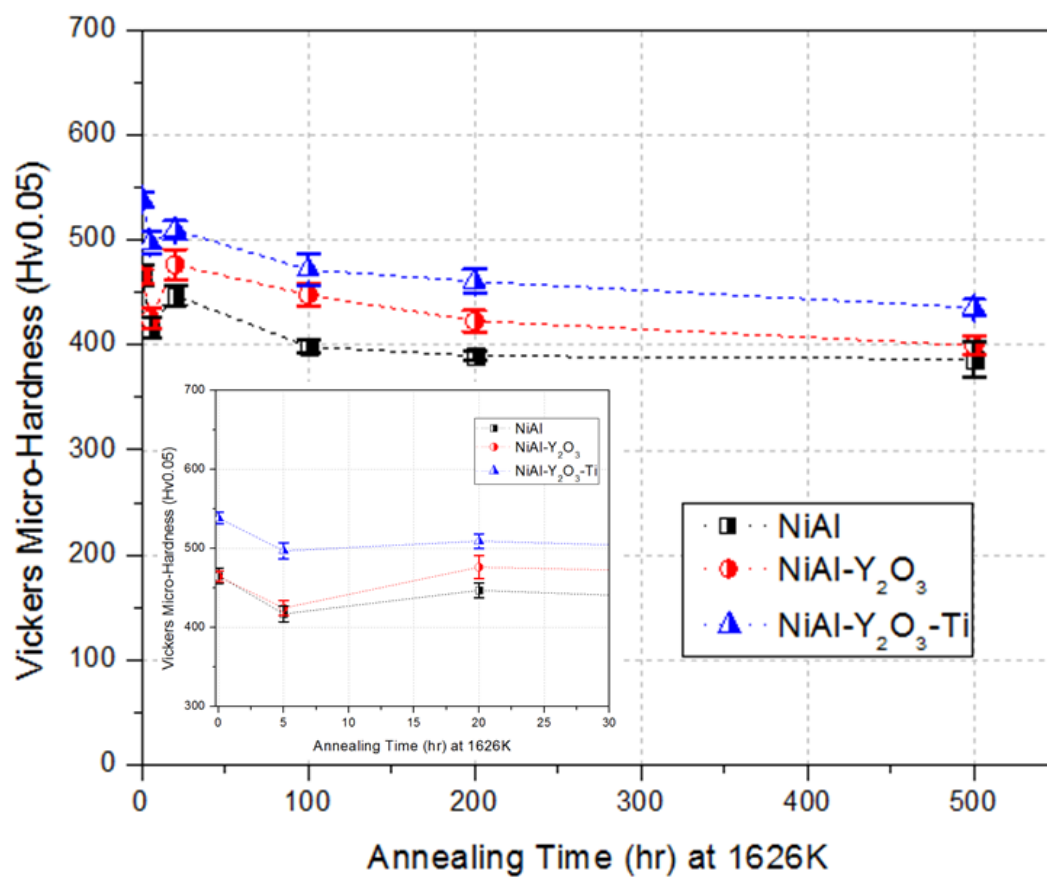


Figure 5-9. Evolution of microhardness with annealing time at 1626K

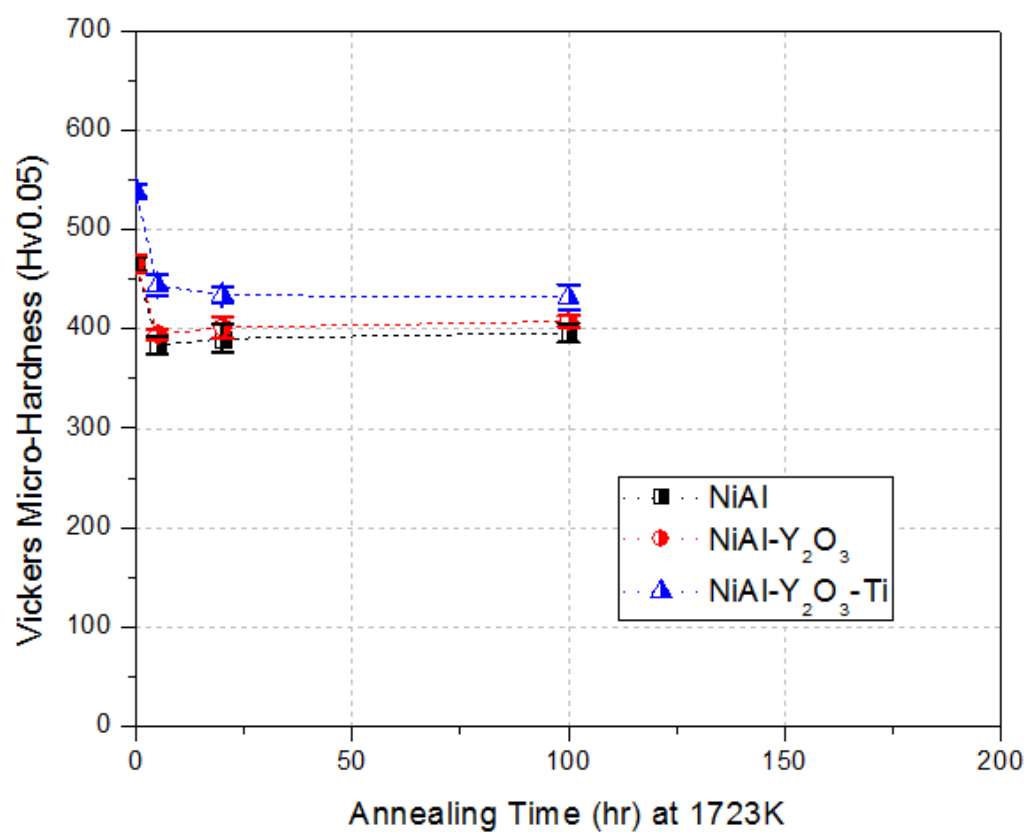


Figure 5-10. Evolution of microhardness with annealing time at 1723K

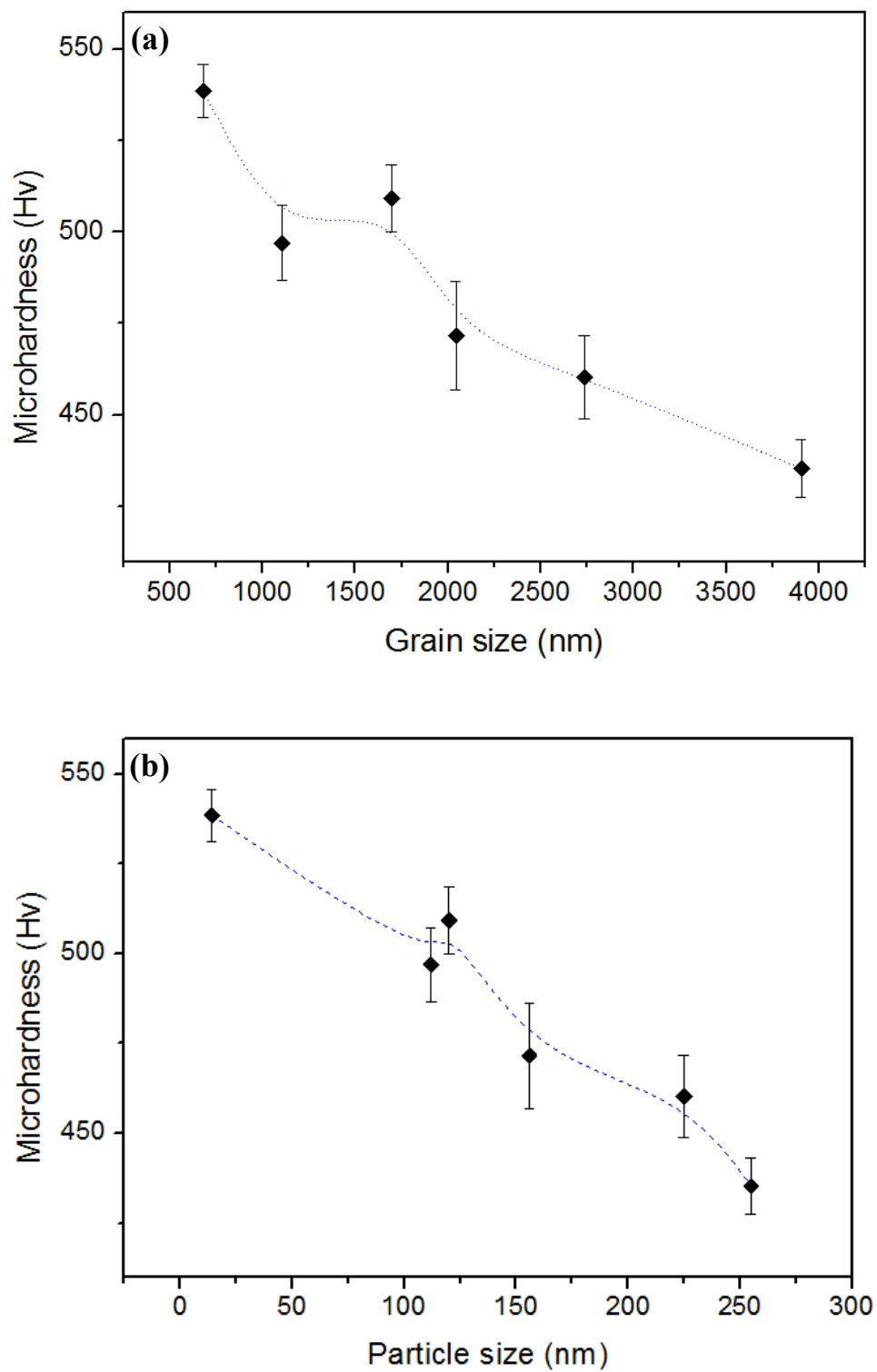


Figure 5-11. Evolution of: microhardness as a function of (a) grain size and (b) particle size in NiAl-Y₂O₃-Ti at 1626K

5.4 Orowan strengthening effect on NiAl-Y₂O₃-Ti alloy

The basic Orowan strengthening model was introduced in Section 1.1 and the semi-quantitative assessment of the Orowan strengthening mechanism for ODS NiAl alloy was discussed in Section 4.2.2.6. This section discusses the Orowan strengthening effect on thermal annealed ODS NiAl alloys.

Evolution of average particle size, particle number density, \sqrt{nD} , and microhardness value for NiAl and NiAl-Y₂O₃-Ti alloys during the thermal annealing at 1626K is represented in Table 5-3. Since we have observed bimodal particle size distribution in the TEM microstructure of the NiAl-Y₂O₃-Ti alloy annealed at 1626K for 20hr, the average particle size of the NiAl-Y₂O₃-Ti is broken up into two groups, smaller than 50 nm and larger than 50 nm, to investigate the evolution of average particle size and fraction of each group associated with annealing time at 1626K. After 20 hr, the fraction of the smaller particle group decreases as annealing time increases. The average particle size of each group increases with annealing time (discussed in Section 5.2) while the particle number density decreases with the annealing time.

Figure 5-12 shows an evolution of \sqrt{nD} and microhardness in NiAl-Y₂O₃-Ti as a function of annealing time at 1626K. After 5 hr annealing, \sqrt{nD} value is dramatically dropped from 1.4×10^7 to 2.09×10^6 and the corresponding microhardness is also significantly decreased from 538 to 497 Hv. The \sqrt{nD} reached plateau after only 5 hrs, while microhardness shows steady decrease with the annealing time. The grain size increase during the annealing, as we have seen in Figure 5-5(a), is believed to be responsible for the steady decrease in microhardness during the annealing.

The microhardness evolution as a function of \sqrt{nD} in NiAl-Y₂O₃-Ti annealed at 1626K is shown in Figure 5-13. It indicates that the Orowan Strengthening in the NiAl-Y₂O₃-Ti is very sensitively working to \sqrt{nD} in a range from 2.08×10^6 to 2.91×10^6 , in contrast, less sensitive after then up to 1.4×10^7 .

Table 5-3. Evolution of average particle size, particle number density, \sqrt{nD} , and microhardness value during the annealing

Alloy	Temperature (K)	Annealing time (hr)	Avg. particle size (D) (nm)		Particle number density (n) (10 ²⁰ /m ³)	√nD	Micro- hardness
			< 50 nm (%)	Avg. size			
			> 50 nm (%)				
NiAl		As- consolidated	30		30	9.49E+06	464.5±7.1
	1626	20	305		0.13	1.99E+06	447.0±9.5
NiAl- Y ₂ O ₃ -Ti		As- consolidated	14		140	1.40E+07	538.5±7.2
	1626	5	30 (31%)	112	0.75	2.91E+06	497±10.2
			150 (69%)				
		20	34 (50%)	120	0.59	2.67E+06	509.2±9.2
			208 (50%)				
		100	40 (24%)	156	0.30	2.17E+06	471.6±14.8
			193 (76%)				
		200	44 (34%)	225	0.26	2.42E+06	460.4±11.4
			318 (66%)				
	500	38 (2%)	255	0.17	2.08E+06	435.3±7.8	
260 (98%)							

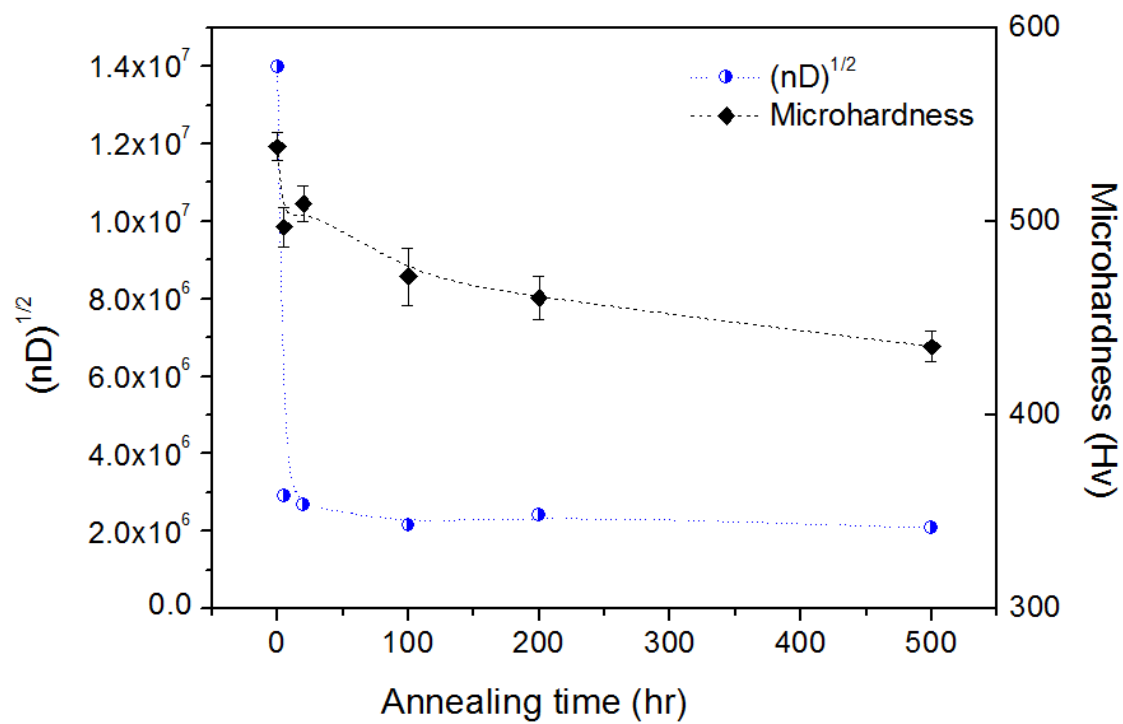


Figure 5-12. Evolution of \sqrt{nD} and microhardness in NiAl-Y₂O₃-Ti as a function of annealing time at 1626K

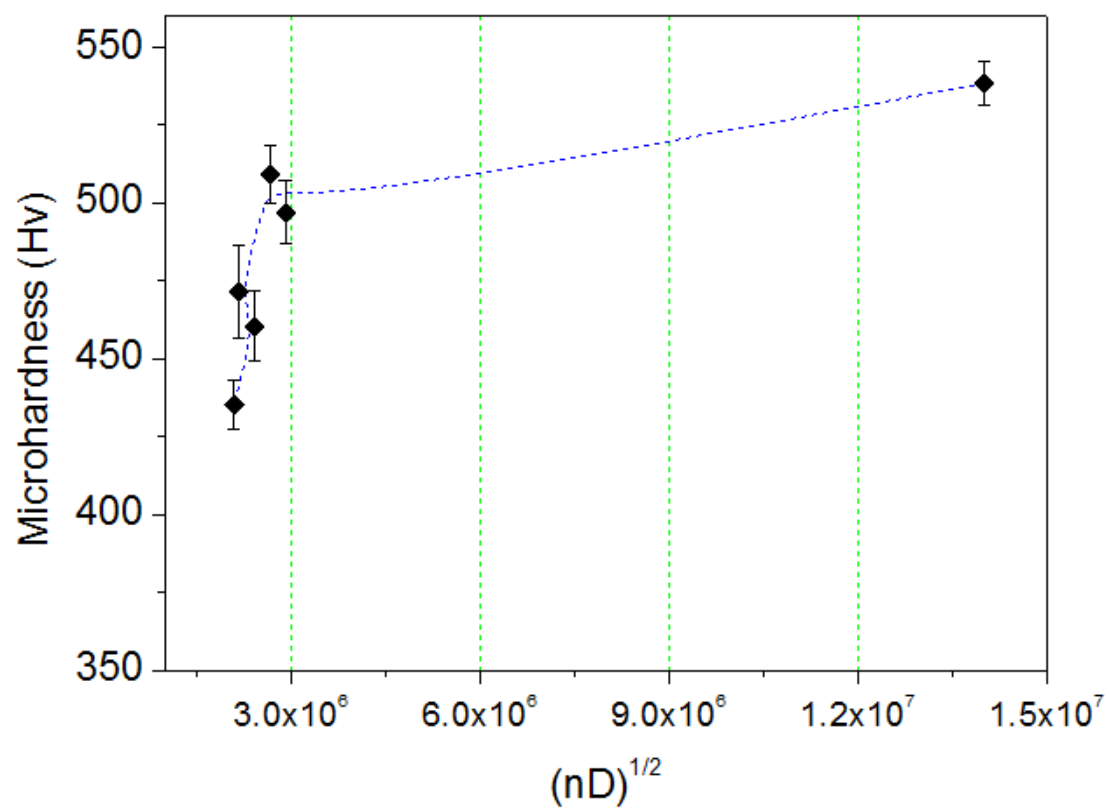


Figure 5-13. Evolution of microhardness as a function of \sqrt{nD} in NiAl-Y₂O₃-Ti at 1626K

5.5 Hall-Petch strengthening effect on NiAl-Y₂O₃-Ti alloy

The Hall-Petch strengthening mechanism is based on dislocation pile up at grain boundaries [12]. The Hall-Petch relationship between the yield strength, σ_y , and grain size, d , is one of the relevant models that describe the strengthening mechanism for conventional materials:

$$\sigma_y = \sigma_o + kd^{-1/2} \quad (5.1),$$

where k is a constant and σ_o is the inherent friction stress of the material in the absence of any other strengthening mechanism. Since the Vickers microhardness value is empirically correlated to the yield strength as discussed in Section 3.5, equation (5.1) can be rewritten as;

$$H_V = H_o + k'd^{-1/2} \quad (5.2),$$

where H_o equals $3\sigma_o$ and k' is a constant. There are some recent reports that the Hall-Petch relationship may not hold for ultrafine nanosized grain structures [99, 114] although the published trends are inconclusive. On the other hand, Furukawa et al. [114] reported that the microhardness data for ultrafine grain materials were consistent with equation (5.1) although with a lower value of k than at the larger grain sizes.

Microhardness measurement data as a function of grain size in NiAl-Y₂O₃-Ti alloy of the present work along with other data from the literature, taken from T.Chen [81] and R.Bowman [116], have been superimposed on Figure 5-14 for comparison. As shown in the Hall-Petch plot in Figure 5-14, a slope of approximately 50.71 GPa(nm)^{1/2} and 1.18 GPa of σ_o (1/3 H_o) are estimated. It is indicated that the microhardness data as a function of grain size holds the Hall-Petch relationship and the k value in the present work is apparently higher than that of the nanometer (10-500 nm) grain sizes [81] but close to that of the micrometer (10-200 μ m) grain sizes [116]. Though the Hall-Petch equation could be derived by fitting the microhardness measurement data with grain size in the present work, the grain size effect is actually not so straightforward. As Srinivasan [117] pointed out, the slope ' k ' refers to the contribution from grain boundaries to the strengthening so that it can vary vastly depending on the condition of the grain boundary, for example, whether the grain boundary is decorated with particles or has any preferential orientation. Hence, it is useful to assess possible effects of the dispersed oxide particle in the NiAl-Y₂O₃-Ti alloy on the grain growth associated with thermal annealing, which will be discussed in Section 5.7.

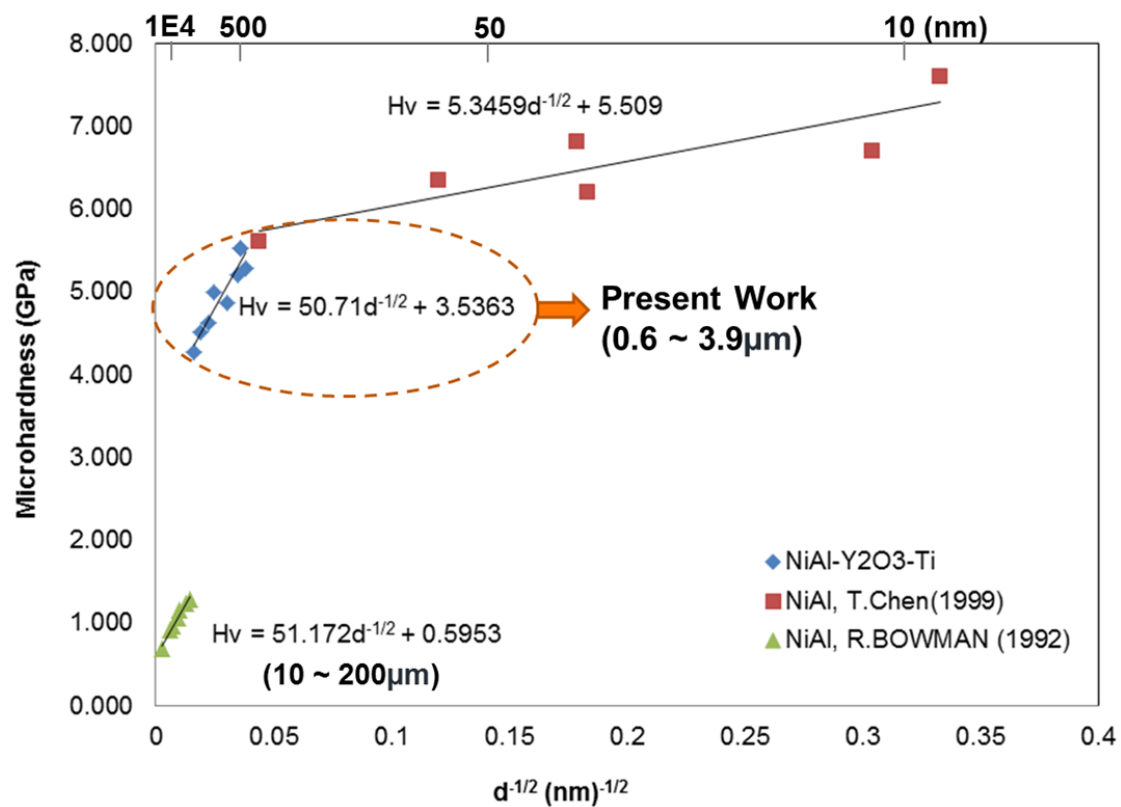


Figure 5-14. Variation in microhardness with $d^{-1/2}$ for NiAl-Y₂O₃-Ti and NiAl alloys. Source: Ref [81, 116]

5.6 Discussion strengthening mechanisms on NiAl-Y₂O₃-Ti alloy

The Orowan and Hall-Petch strengthening effect have been discussed in Section 5.4 and 5.5 respectively. The present work attempts to assess the role played by the two strengthening mechanisms in the ODS NiAl alloys annealed at 1626K. Assuming the major strengthening mechanism of the alloy is contributed by the grain refinement and dispersion strengthening, the microhardness data along with microstructure characterization data discussed in Section 5.2 through 5.5 was evaluated to investigate the contribution of each strengthening mechanism, and was attempted to rationalize the increase in strength with the microstructure of the ODS NiAl alloys.

The microhardness (converted into unit of MPa), Hall-Petch, and Orowan strength as a function of annealing time in NiAl-Y₂O₃-Ti annealed at 1626K are plotted in a graph as illustrated in Figure 5-15. The observation is that there is a significant contribution (about 45% of total strength/microhardness) from the Orowan strengthening for the as-consolidated specimen, however, the Orowan contribution is rapidly decreased to ~150 MPa (about 10% of total strength) after 5 hrs and reaches plateau after then. On the other hand, the Hall-Petch strengthening contributes strength of 569 MPa for the as-consolidated condition and suddenly decreased until 20 hrs, and then the Hall-Petch strengthening contribution is gradually decreased as annealing time increases. It indicates that the contribution of the Hall-Petch strengthening mechanism is dominant compared to Orowan strengthening mechanism during the annealing at 1626K.

Table 5-4 represents the summary of the contributing strengthening components and the microhardness value assessment between the NiAl (alloy ①) and NiAl-Y₂O₃-Ti (alloy ③) alloys annealed at 1626K for 20 hr, where α is assumed to 0.8, and M, G, b, and k are 3.06, 71.5 (GPa), 0.288x10⁻⁹ (m), and 0.53 (MPa \sqrt{m}) as estimated in Figure 5-14. The results can be summarized as follows:

- From the Orowan strengthening, the yield stress increase ($\Delta\sigma_p$) in the alloy ① is computed to 100.3 MPa while that of the alloy ③ is about 134.6 MPa.
- Based on the Hall-Petch strengthening, the indication is that the yield stress increase ($\Delta\sigma_g$) in alloy ① and alloy ③ are computed to be 361.5 and 406.5 MPa respectively.
- The difference in the sum of two strengthening effects between the alloy ① and ③ is 79 MPa.
- But, the increase of the microhardness between the alloy ① and ③ is 203 MPa, which is not consistent with the strengthening estimations as represented in Table 5-4.

The combination of grain size refinement and oxide precipitate (coarser than 10-15 nm) dispersion strengthening was not able to fully explain the increase in strength of the NiAl-Y₂O₃-Ti alloy. This supports the possibility of the presence of nanosized Y-Ti-O precipitates in the NiAl-Y₂O₃-Ti alloy. Thus, a higher resolution study along with small

angle neutron scattering (SANS) study for better estimation by volume averaged characterization is required for further microstructure research.

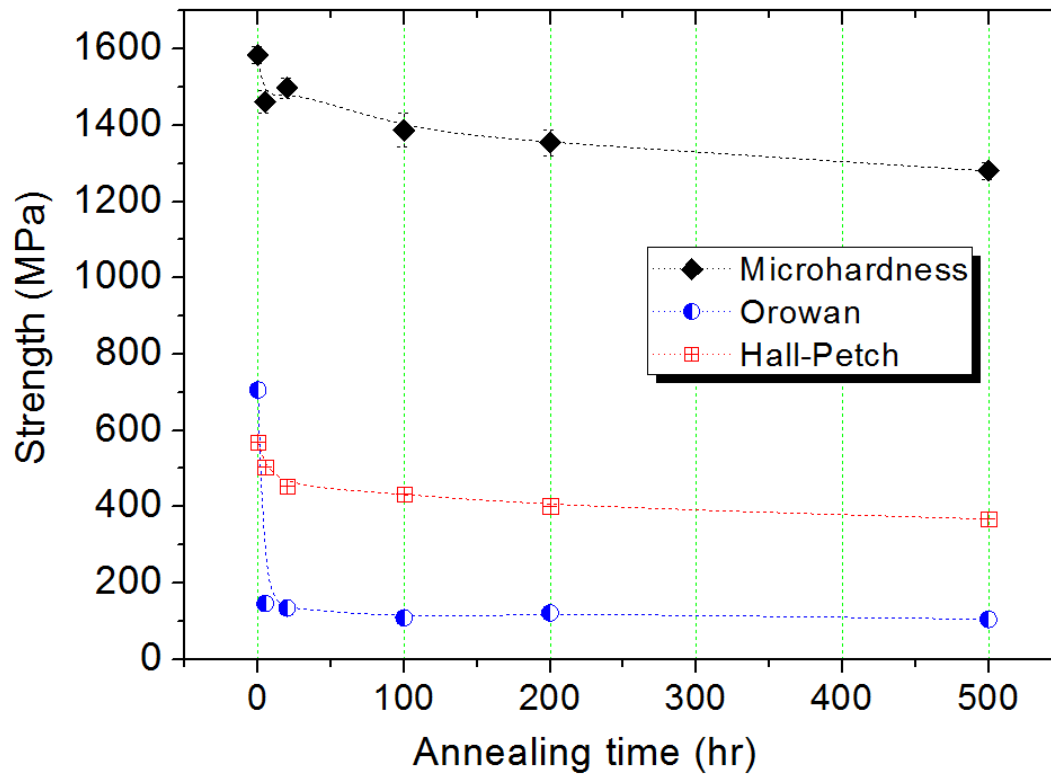


Figure 5-15. Evolution of microhardness, Orowan strength, and Hall-Petch strength as a function of annealing time in NiAl-Y₂O₃-Ti annealed at 1626K

Table 5-4. The details of strengthening components and the microhardness value assessment for NiAl alloys

Alloy	Anneal time (hr) & Temp. (K)	\sqrt{nD} (10^6)	$\Delta\sigma_p$ (MPa) = $(\alpha M G b \sqrt{nD})$	$d^{-1/2}$	$\Delta\sigma_g$ (MPa) = $(k d^{-1/2})$	Micro-hardness (Hv)	σ_y (MPa) = $1/3 H_v$	$(\Delta\sigma_p + \Delta\sigma_g)^{\textcircled{3}} - (\Delta\sigma_p + \Delta\sigma_g)^{\textcircled{1}}$ (MPa)	$\Delta\sigma_{y^{\textcircled{3}} - \textcircled{1}}$ (MPa)
①NiAl	20 hr at 1626K	1.99	100.3	0.0015	361.5	447.0	1460	79	203
③NiAl-Y ₂ O ₃ -Ti		2.67	134.6	0.0013	406.5	509.2	1663		

5.7 Grain growth kinetics

Grain growth occurs by grain boundary migration, or more appropriately, the motion of atoms across grain boundaries. It is obvious that not all grains can grow but large ones enlarge at the expense of small ones that shrink, in other words, smaller grains which have a higher radius of curvature shrink as a result of losing atoms to larger grains [12, 118]. Thus, the average grain size increases with time provided enough activation energy for grain growth, therefore, a range of grain sizes exist at any particular instant. Grain boundary migration is just the short-range diffusion of atoms from one side of the boundary to the other. The directions of boundary movement and atomic motion are opposite to each other, as shown in Figure 5-16. For many polycrystalline materials, the grain diameter d varies with time t according to the relationship [12, 118];

$$d^2 - d_0^2 = k_g t^n \quad (5.3),$$

where d and d_0 are the instantaneous and initial grain size, respectively, k_g is a temperature dependent constant, t is the time and the value of n is generally equal to unity. The constant k_g can be expressed as;

$$k_g = A \exp\left(-\frac{Q}{RT}\right) \quad (5.4),$$

where Q is the activation energy for grain growth, R is the gas constant, T is temperature, and A is a constant.

Figure 5-17 shows the grain size evolutions of the ODS NiAl alloys as a function of annealing time. As for the NiAl-Y₂O₃-Ti alloy, grain growth rate at 1626K is approximately 35 times faster than that at 1433K. On the other hand, it is observed that the grain growth rate of the NiAl is 0.0636 (μm²/hr) while that of the NiAl-Y₂O₃-Ti alloy is 0.0283 (μm²/hr) upon annealing at 1626K. When it comes to the annealing at 1433K, grain growth rate of the NiAl-Y₂O₃ is much faster than that of the NiAl-Y₂O₃-Ti alloy although the grain growth rates at 1433K are far below compared to the grain growth rates at 1626K. Using the equation (5.3) and (5.4), a semi-logarithmic plot of $(d^2 - d_0^2)$ versus $1/T$ for NiAl-Y₂O₃-Ti alloy is shown in Figure 5-18. The activation energy for grain growth was estimated to 305±7.9 kJ/mol which is close to the activation energy for lattice self-diffusion in pure NiAl [119].

5.8 Summary and discussion

Thermal stability study on the ODS NiAl alloys following high temperature isothermal annealing has been discussed in this chapter. The grain growth was very effectively inhibited during the annealing at 1433K while fairly significant grain growth occurred during the annealing at 1626K. The bimodal particle size distribution was observed during the high temperature annealing. There was a steady increase in the size of the aluminum oxide particles, on the other hand, the nanosized particles showed a relatively

high thermal stability to resist changes in size upon annealing at 1433K and 1626K as well as 1723K. It was indicated that the NiAl-Y₂O₃-Ti alloy has the highest thermal stability among the ODS NiAl alloys, in which it was believed that presumable small particles contribute to the very limited grain and particle growth resulted in high strength of the alloy. The combination of grain size refinement and coarser oxide precipitate dispersion strengthening was not able to fully explain the increase in strength of the NiAl-Y₂O₃-Ti alloy. The Orowan strengthening effect and the effective Hall-Petch strengthening component have been studied to assess the role played by two strengthening mechanisms in the advanced ODS NiAl alloys. Finally, the grain growth kinetics for the NiAl-Y₂O₃-Ti alloy could be derived through TEM microstructure characterization and microhardness measurement. The NiAl-Y₂O₃-Ti alloy has the smallest grain growth rate at temperatures of 1433K and 1626K and lattice diffusion is believed to be the dominant grain growth mechanism.

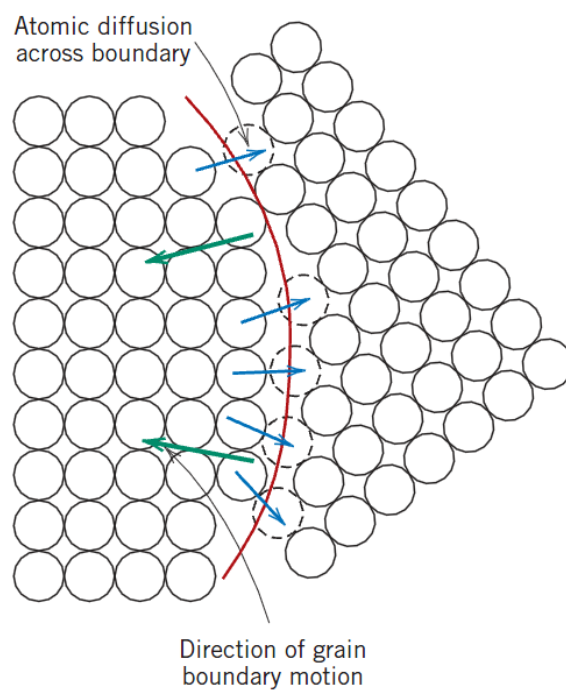


Figure 5-16. Schematic representation of grain growth by atomic diffusion as reproduced from Ref [118]

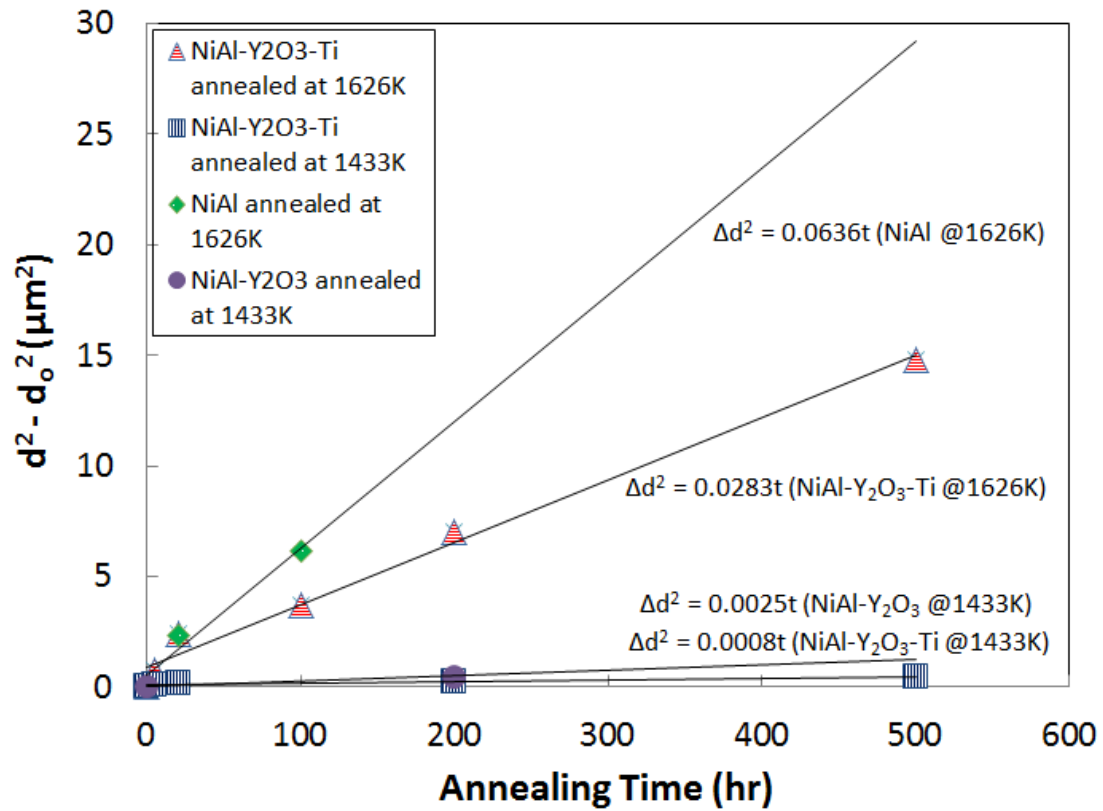


Figure 5-17. The grain size evolutions of the ODS NiAl alloys as a function of annealing time at 1433 and 1626K

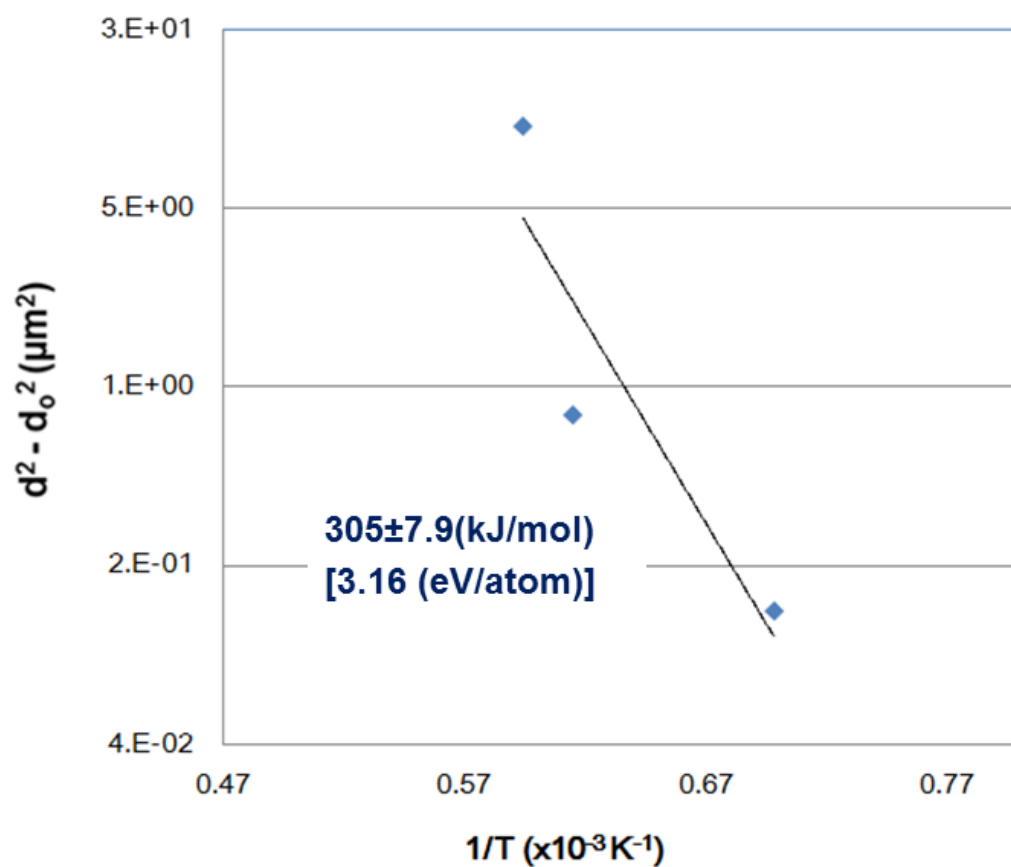


Figure 5-18. Semi-logarithmic plot of $(d^2 - d_0^2)$ versus $1/T$ for NiAl- Y_2O_3 -Ti

Chapter 6

Conclusions and Future Work

6.1 Conclusions

This dissertation investigated advanced ODS NiAl alloys, along with Fe-Cr based 14YWT alloys with the objective of improving the high temperature strength and creep resistance driven by incorporating a high number density of thermally stable nano-meter scale oxide precipitate clusters, including (1) materials processing, (2) experimental characterization, and (3) thermal stability and grain growth kinetics for ODS NiAl. An extensive experimental study has been performed to characterize nanoscale microstructural features that lead to the best properties of the alloy and understand the thermodynamics and kinetics of nanoclusters formation and thermal stability, effective strengthening components, and grain growth kinetics associated with high temperature annealing. In this final chapter, the key observations of previous chapters are summarized and some ideas for future work are suggested.

6.1.1 Materials processing

The details of the materials processing that were performed during the fabrication of ODS NiAl and ferritic 14YWT alloys were described in Chapter 2. The investigation on the optimal milling time which can produce alloys with more homogeneous distributions of NCs and more uniform fine grain size distributions were performed. In addition, processing improvement for reducing nitrogen contamination was achieved by the modification of Simoloyer CM-01 operating procedure and installation of a gate valve. Spark plasma sintering, hot extrusion, and hot isostatic pressing were applied to consolidate the alloy power materials.

6.1.2 Experimental characterization

Various experimental characterization techniques and methodologies used in this

study to investigate the materials microstructure were introduced in Chapter 3. In Chapter 4, the results of microstructural characterization along with microhardness measurement in the mechanically alloyed and consolidated alloys were discussed.

6.1.3 Thermal stability and grain growth kinetics for ODS NiAl

A systematic study on the thermal stability of ODS NiAl alloys following high temperature isothermal annealing was discussed in Chapter 5. Extensive thermal annealing was performed for 500 hrs at selected temperatures of 1433, 1626, and 1723K. The evolution of nanosize precipitate size, grain size, particle number density, and microhardness has been assessed associated with annealing time and temperature. The Orowan strengthening effect and the effective Hall-Petch strengthening component have been studied. Finally, grain growth kinetics for the ODS NiAl were studied through TEM microstructure characterization associated with the annealing temperature and time.

6.2 Future work

While a significant experimental effort has been performed to develop advanced ODS NiAl alloys as well as to contribute to studying mechanical alloying process of nanostructured ferritic 14YWT alloys. There remain several research items for further study and improvement of these alloys.

For the ODS NiAl alloys, the suggested future research includes the following: from the practical point of view, alloy design modification as well as material process optimization is necessary to obtain a higher number density of nanoclusters with fine grain structure to further improve the high thermal stability. Additional XRD characterization or any other technique is need to investigate any phase separation of B2 NiAl structure after thermal annealing since a significant amount of Al-rich oxide precipitates were observed in the microstructure after the annealing, which gives rise to concern about destabilizing the B2 NiAl phase and transformation from NiAl to Ni₃Al or any possible Ni-rich intermetallic. A higher resolution study along with additional Atom Probe Tomography is required for further microstructure characterization to confirm or rule out the presence of small particles in the NiAl-Y₂O₃-Ti alloy and their evolution during thermal annealing. More TEM characterization along with small angle neutron scattering (SANS) study for better estimation by volume averaged characterization is also needed to better quantify the size, number density, and composition of the precipitates associated with thermal annealing to quantatively assess an Orowan strengthening component, which will eventually enable assessing whether the Hall-Petch or Orowan strengthening mechanism is dominant in the ODS NiAl alloys. Further, the development of atomic simulations will be important to provide insight into oxide precipitate cluster composition that could ultimately provide a framework to optimize alloy compositions containing the largest number density of nanoclusters with the highest thermal stability. Besides, atomistic molecular dynamics simulations can provide understanding of dislocation-obstacle interactions and detachment mechanisms. Finally, it will be

important to develop a fundamental knowledge to optimize the nano-microstructures of the ODS NiAl alloys to achieve a good balance of required thermo-mechanical properties such as high temperature strength, creep strength, fracture toughness, corrosion resistance, and etc.

As far as the 14YWT alloy concerned, an extensive study of experimental characterization and atomic calculation have been performing in collaborating with researchers at UCSB, the optimization of material process study is likely to need to resolve heterogeneity of nano features in the microstructure. In addition, more high resolution study is also needed to characterize the nanosize oxide precipitates, grain, and dislocation structures as well as their correlations with each other.

Bibliography

- [1] Komai, N., F. Masuyama, and M. Igarashi, *10-year experience with T23(2.25Cr-1.6W) and T122(12Cr-0.4Mo-2W) in a power boiler*. Journal of Pressure Vessel Technology-Transactions of the Asme, 2005. 127(2): p. 190-196.
- [2] Masuyama, F., *History of power plants and progress in heat resistant steels*. Isij International, 2001. 41(6): p. 612-625.
- [3] Dimiduk, D.M. and J.H. Perepezko, *Mo-Si-B alloys: Developing a revolutionary turbine-engine material*. Mrs Bulletin, 2003. 28(9): p. 639-645.
- [4] Goidich, S.J., *SUPERCRITICAL BOILER OPTIONS TO MATCH FUEL COMBUSTION CHARACTERISTICS*. 2007.
- [5] Mark Richardson, Y.K.a.Y.S., *Supercritical Boiler Technology Matures*. 2004.
- [6] A. Onyszko, K.K., J. Sieniawski, *Turbine blades of the single crystal nickel based CMSX-6 superalloy*. Journal of Achievements in Materials and Manufacturing Engineering, 2009. 32(1).
- [7] Zhao, J.C. and J.H. Westbrook, *Ultrahigh-temperature materials for jet engines*. Mrs Bulletin, 2003. 28(9): p. 622-630.
- [8] Clarke, D.R. and C.G. Levi, *Materials design for the next generation thermal barrier coatings*. Annual Review of Materials Research, 2003. 33: p. 383-417.
- [9] Ashby, M.F., *FIRST REPORT ON DEFORMATION-MECHANISM MAPS*. Acta Metallurgica, 1972. 20(7): p. 887-&.
- [10] Arzt, E., et al., *Interface controlled plasticity in metals: dispersion hardening and thin film deformation*. Progress in Materials Science, 2001. 46(3-4): p. 283-307.
- [11] Arzt, E., *Overview no. 130 - Size effects in materials due to microstructural and dimensional constraints: A comparative review*. Acta Materialia, 1998. 46(16): p. 5611-5626.
- [12] E.Reed-Hill, R., *Physical Metallurgy Principles 2nd Edition*1973: Litton Educational Publishing, Inc. 326-377.
- [13] E.Arzt, *Creep of Oxide-dispersion Strengthened Alloys*. Encyclopedia of Materials: Science and Technology, 2001: p. 1800-1806.
- [14] E. Arzt, E.G.a.P.G., *Dispersion strengthened intermetallics by mechanical alloying: creep results and dislocation mechanisms*. High Temperature Ordered Intermetallic Alloys V, 288 Mat. Res. Soc. Symp. Proc.MRS Fall Meeting 1992, Boston, USA (2nd edition), (1995), 1992: p. 861.
- [15] Grahle, P. and E. Arzt, *Microstructural development in dispersion strengthened NiAl produced by mechanical alloying and secondary recrystallization*. Acta Materialia, 1997. 45(1): p. 201-211.

- [16] Sherman, M. and K. Vedula, *HIGH-TEMPERATURE DISPERSION STRENGTHENING OF NiAl*. Journal of Materials Science, 1986. 21(6): p. 1974-1980.
- [17] Arzt, E. and P. Grahle, *High temperature creep behavior of oxide dispersion strengthened NiAl intermetallics*. Acta Materialia, 1998. 46(8): p. 2717-2727.
- [18] Kitaoka, A., et al., *Toughening and strengthening of NiAl with Al₂O₃ by the addition of ZrO₂(3Y)*. Journal of the American Ceramic Society, 2000. 83(5): p. 1311-1313.
- [19] Rablbauer, G.F.a.R., *HIGH TEMPERATURE RESISTANT INTERMETALLIC NiAl-BASED ALLOYS WITH REFRACTORY METALS Cr, Mo, Re*. Mat. Res. Soc. Symp. Proc. , 2003. Vol. 753.
- [20] Kim, J.S., et al., *Densification and mechanical property of nanostructured NiAl produced by mechanical-alloying and spark-plasma sintering*, in *Designing, Processing and Properties of Advanced Engineering Materials, Pts 1 and 2*, S.G. Kang and T. Kobayashi, Editors. 2004. p. 1101-1104.
- [21] Oruganti, R.K., S. Sampath, and S. Amancherla, *On the Arzt-Rosler-Wilkinson (ARW) model for detachment controlled creep*. Scripta Materialia, 2005. 52(4): p. 323-327.
- [22] Rosler, J. and E. Arzt, *THE KINETICS OF DISLOCATION CLIMB OVER HARD PARTICLES .1. CLIMB WITHOUT ATTRACTIVE PARTICLE-DISLOCATION INTERACTION*. Acta Metallurgica, 1988. 36(4): p. 1043-1051.
- [23] Arzt, E. and E. Gohring, *A model for dispersion strengthening of ordered intermetallics at high temperatures*. Acta Materialia, 1998. 46(18): p. 6575-6584.
- [24] Ukai, S., et al., *ALLOYING DESIGN OF OXIDE DISPERSION-STRENGTHENED FERRITIC STEEL FOR LONG-LIFE FBRS CORE MATERIALS*. Journal of Nuclear Materials, 1993. 204: p. 65-73.
- [25] Alinger, M.J., G.R. Odette, and D.T. Hoelzer, *The development and stability of Y-Ti-O nanoclusters in mechanically alloyed Fe-Cr based ferritic alloys*. Journal of Nuclear Materials, 2004. 329: p. 382-386.
- [26] Okuda, T. and M. Fujiwara, *DISPERSION BEHAVIOR OF OXIDE PARTICLES IN MECHANICALLY ALLOYED ODS STEEL*. Journal of Materials Science Letters, 1995. 14(22): p. 1600-1603.
- [27] J. Bentley, D.T.H., D.W. Coffey and K.A. Yarborough, *EFTEM and Spectrum Imaging of Mechanically Alloyed Oxide-Dispersion-Strengthened 12YWT and 14YWT Ferritic Steels*. Microscopy and Microanalysis, 2004: p. 662-663
- [28] Yamashita, S., et al., *Formation of nanoscale complex oxide particles in mechanically alloyed ferritic steel*. Philosophical Magazine Letters, 2004. 84(8): p. 525-529.
- [29] Jiang, Y., J.R. Smith, and G.R. Odette, *Formation of Y-Ti-O nanoclusters in nanostructured ferritic alloys: A first-principles study*. Physical Review B, 2009. 79(6).
- [30] Klimiankou, M., R. Lindau, and A. Moslang, *HRTEM Study of yttrium oxide particles in ODS steels for fusion reactor application*. Journal of Crystal Growth, 2003. 249(1-2): p. 381-387.
- [31] Hoelzer, D.T., et al., *Influence of particle dispersions on the high-temperature strength of ferritic alloys*. Journal of Nuclear Materials, 2007. 367: p. 166-172.

- [32] Alinger, M.J., et al., *Lattice Monte Carlo simulations of nanocluster formation in nanostructured ferritic alloys*. Journal of Nuclear Materials, 2007. 367: p. 153-159.
- [33] Alinger, M.J., *On the Formation and Stability of Nanometer Scale Precipitates in Ferritic Alloys during Processing and High Temperature Service*. 2004.
- [34] Ukai, S., et al., *R&D of oxide dispersion strengthened ferritic martensitic steels for FBR*. Journal of Nuclear Materials, 1998. 258: p. 1745-1749.
- [35] Odette, G.R., M.J. Alinger, and B.D. Wirth, *Recent developments in irradiation-resistant steels*, in *Annual Review of Materials Research* 2008. p. 471-503.
- [36] Kishimoto, H., et al., *TEM examination of microstructural evolution during processing of 14CrYWTi nanostructured ferritic alloys*. Journal of Nuclear Materials, 2004. 329: p. 369-371.
- [37] Haussler, D., et al., *Interaction processes between dislocations and particles in the ODS nickel-base superalloy INCONEL MA 754 studied by means of in situ straining in an HVEM*. Materials Science and Engineering a-Structural Materials Properties Microstructure and Processing, 2001. 309: p. 500-504.
- [38] Ukai, S., et al., *High-temperature strength characterization of advanced 9Cr-ODS ferritic steels*. Materials Science and Engineering a-Structural Materials Properties Microstructure and Processing, 2009. 510-11: p. 115-120.
- [39] Miller, M.K., et al., *Atom probe tomography of nanoscale particles in ODS ferritic alloys*. Materials Science and Engineering a-Structural Materials Properties Microstructure and Processing, 2003. 353(1-2): p. 140-145.
- [40] Coreno-Alonso, O., et al. *Characterization of NiAl intermetallic produced by mechanical alloying and consolidated by spark plasma sintering*. 2000. Trans Tech Publications Ltd.
- [41] Liu, Z.G., et al., *Consolidation and compression property of nanocrystalline NiAl synthesized by mechanical alloying*. Journal of Materials Science & Technology, 1996. 12(1): p. 7-10.
- [42] Kim, J.S., et al. *Densification and mechanical property of nanostructured NiAl produced by mechanical-alloying and spark-plasma sintering*. 2004. Trans Tech Publications Ltd.
- [43] Peng, L.M., *Fabrication and mechanical properties of microalloyed and ceramic particulate reinforced NiAl-based alloys*. Journal of Alloys and Compounds, 2007. 440(1-2): p. 150-153.
- [44] N. V. Chi, T.Q.L., N. H. Viet and N. M. Cu, *Formation of Metastable Phases of the Ni-Al System by Mechanical Milling*. Journal of Materials Online, 2005.
- [45] Liu, K.W., et al., *Formation of nanocrystalline B2-structured (Ru,Ni)Al in the ternary Ru-Al-Ni system by mechanical alloying and its thermal stability*. Materials Science and Engineering a-Structural Materials Properties Microstructure and Processing, 2001. 313(1-2): p. 187-197.
- [46] Portnoy, V.K., et al., *Formation of nickel aluminides by mechanical alloying and thermodynamics of interaction*. Journal of Alloys and Compounds, 2002. 336(1-2): p. 196-201.
- [47] Ur, S.C., P. Nash, and G.T. Higgins, *Grain growth and secondary recrystallization in mechanically alloyed NiAl*. Scripta Materialia, 1996. 34(1): p. 53-59.
- [48] Albiter, A., et al., *Improvement of the mechanical properties in a nanocrystalline*

- NiAl intermetallic alloy with Fe, Ga and Mo additions*. Materials Science and Engineering a-Structural Materials Properties Microstructure and Processing, 2003. 347(1-2): p. 154-164.
- [49] Abhik, N.C., et al., *Influence of heat of formation of B2/L1(2) intermetallic compounds on the milling energy for their formation during mechanical alloying*. Journal of Alloys and Compounds, 2008. 465(1-2): p. 106-112.
- [50] Liu, Z.G., et al., *Mechanical alloying synthesis and structural characterization of ternary Ni-Al-Fe alloys*. Journal of Materials Science, 1997. 32(18): p. 4857-4864.
- [51] Cheng, T.Y., *MECHANICALLY ALLOYED NIAL STRENGTHENED BY TiB₂ AND Y₂O₃*. Journal of Materials Science Letters, 1995. 14(20): p. 1455-1457.
- [52] Oh-ishi, K., Z. Horita, and M. Nemoto, *Microstructure and strength of B2-ordered NiAl containing L2(1)-Ni₂AlHf precipitates*. Materials Science and Engineering a-Structural Materials Properties Microstructure and Processing, 1997. 240: p. 472-478.
- [53] Guo, J.T., X.H. Du, and L.Z. Zhou. *Preparation of nanocrystalline NiAl compounds and composites by mechanical alloying*. 2005. Trans Tech Publications Ltd.
- [54] Krivoroutchko, K., et al., *Solid state reactions in Ni-Al-Ti-C system by mechanical alloying*. Journal of Alloys and Compounds, 2000. 308: p. 230-236.
- [55] Gaffet, E., *STRUCTURAL INVESTIGATION OF MECHANICALLY ALLOYED (NiAl)_(1-x)(M)_(x) (M=Fe, Zr) NANOCRYSTALLINE AND AMORPHOUS PHASES*. Nanostructured Materials, 1995. 5(4): p. 393-409.
- [56] Enayati, M.H., F. Karimzadeh, and S.Z. Anuari, *Synthesis of nanocrystalline NiAl by mechanical alloying*. Journal of Materials Processing Technology, 2008. 200(1-3): p. 312-315.
- [57] Ivanov, E.Y., et al., *SYNTHESIS OF NICKEL ALUMINIDES BY MECHANICAL ALLOYING*. Izvestiya Sibirskogo Otdeleniya Akademii Nauk Sssr Seriya Khimicheskikh Nauk, 1988(6): p. 80-83.
- [58] Krivoroutchko, K., et al. *Synthesis of powder alloys in Ni-Al-Nb-C system by mechanical alloying*. 2001. Trans Tech Publications Ltd.
- [59] Miettinen J., H.U.o.T., Laboratory of Metallurgy, Helsinki, Finland. *Thermodynamic description of the Cu-Al-Ni system at the Cu-Ni side, Calphad*. 2005; Available from: <http://www1.asminternational.org/asmenterprise/APD/ViewAPD.aspx?id=101031>.
- [60] Scheppe, F., et al., *Nickel aluminides: a step toward industrial application*. Materials Science and Engineering a-Structural Materials Properties Microstructure and Processing, 2002. 329: p. 596-601.
- [61] Whittenberger, J.D., B. Aikin, and J. Salem, *Creep and toughness of cryomilled NiAl containing Cr*. Journal of Materials Research, 2001. 16(5): p. 1333-1344.
- [62] Ma, G.J., et al., *Initial study of strengthening of NiAl-Cr(Mo)-Hf alloys by strong magnetic field*. Journal of Materials Research, 2005. 20(2): p. 295-298.
- [63] Fu, C.L., et al., *Magnetism-induced solid solution softening in NiAl with Co, Fe, Mn, and Cr solute atoms: theory and experiment*. Intermetallics, 2004. 12(7-9): p. 911-919.
- [64] Darolia, R., *Ductility and fracture toughness issues related to implementation of NiAl for gas turbine applications*. Intermetallics, 2000. 8(9-11): p. 1321-1327.

- [65] Liu, C.T., *RECENT ADVANCES IN ORDERED INTERMETALLICS*. Materials Chemistry and Physics, 1995. 42(2): p. 77-86.
- [66] Whittenberger, J.D. and M.J. Luton, *ELEVATED-TEMPERATURE CREEP-PROPERTIES OF NIAL CRYOMILLED WITH AND WITHOUT Y2O3*. Journal of Materials Research, 1995. 10(5): p. 1171-1186.
- [67] Ur, S.C. and P. Nash, *Secondary recrystallization and high temperature compressive properties of ODS MA NiAl*. Scripta Materialia, 2002. 47(6): p. 405-409.
- [68] Ashby, M.F., H.U.C.M.D.O. ENGINEERING, and A. PHYSICS., *The theory of the critical shear stress and work hardening in dispersion-hardened crystals* 1966: Defense Technical Information Center.
- [69] Gilman, P.S. and J.S. Benjamin, *MECHANICAL ALLOYING*. Annual Review of Materials Science, 1983. 13: p. 279-300.
- [70] Shewfelt, R.S.W. and L.M. Brown, *High-temperature strength of dispersion-hardened single crystals: I. Experimental results*. Philosophical Magazine, 1974. 30(5): p. 1135-1145.
- [71] Lund, R.W. and W.D. Nix, *High temperature creep of Ni-20Cr-2ThO₂ single crystals*. Acta Metallurgica, 1976. 24(5): p. 469-481.
- [72] Meng, J., C.C. Jia, and Q. He, *Characteristics of mechanical alloyed Ni-Al powder for sintering*. Rare Metals, 2007. 26(4): p. 372-376.
- [73] Wright, R.N., J.R. Knibloe, and R.D. Noebe, *CONSOLIDATION OF NIAL POWDERS USING HOT ISOSTATIC PRESSING*. Materials Science and Engineering a-Structural Materials Properties Microstructure and Processing, 1991. 141(1): p. 79-83.
- [74] Wilson, A.W. and J.M. Howe, *Effect of alloying additions on beta ' precipitation in NiAl-Ti base alloys*. Acta Materialia, 2001. 49(14): p. 2653-2660.
- [75] Heshmati-Manesh, S. and A. Jabbarnia, *Effect of milling time on crystallite size and morphology of NiAl based nano composite powder prepared by mechanical assisted SHS route*. AIP Conference Proceedings, 2009. 1136.
- [76] Borner, I. and J. Eckert. *Grain size effects and consolidation in ball-milled nanocrystalline NiAl*. 1997. Transtec Publications Ltd.
- [77] Joardar, J., S.K. Pabi, and B.S. Murty, *Milling criteria for the synthesis of nanocrystalline NiAl by mechanical alloying*. Journal of Alloys and Compounds, 2007. 429(1-2): p. 204-210.
- [78] Czeppe, T. and S. Wierzbinski. *Structure and mechanical properties of NiAl and Ni3Al-based alloys*. 2000. Pergamon-Elsevier Science Ltd.
- [79] Witkin, D.B. and E.J. Lavernia, *Synthesis and mechanical behavior of nanostructured materials via cryomilling*. Progress in Materials Science, 2006. 51(1): p. 1-60.
- [80] Li Lu, M.O.L., *Mechanical Alloying* 1998: Kluwer Academic Publishers.
- [81] Chen, T., J.M. Hampikian, and N.N. Thadhani, *Synthesis and characterization of mechanically alloyed and shock-consolidated nanocrystalline NiAl intermetallic*. Acta Materialia, 1999. 47(8): p. 2567-2579.
- [82] Bakker, H., G.F. Zhou, and H. Yang, *MECHANICALLY DRIVEN DISORDER AND PHASE-TRANSFORMATIONS IN ALLOYS*. Progress in Materials Science, 1995. 39(3): p. 159-241.

- [83] TOKITA, M., *Mechanism of spark plasma sintering*. Proceedings of 2000 Powder Metallurgy World Congress, 2000.
- [84] Song, J., et al., *High temperature microstructure and microhardness evolution in dense NiCrAlY bulk material fabricated by spark plasma sintering*. Materials Science and Engineering a-Structural Materials Properties Microstructure and Processing, 2011. 528(7-8): p. 3210-3217.
- [85] Murakami, T., et al., *High-temperature tribological properties of Al₂O₃, Ni-20 mass% Cr and NiAl spark-plasma-sintered composites containing BaF₂-CaF₂ phase*. Wear, 2005. 259(1-6): p. 626-633.
- [86] Hyun Rok Cha, C.H.Y., Hyeon-Taek Son, Jae Ik Cho, *The Improvement of permeability and strength in soft magnetic composites motor core using spark plasma sintering process*. Advanced Materials Research, 2007. 26-28: p. 609-612.
- [87] Kwon, Y.S., et al., *Microstructure changes in TiB₂-Cu nanocomposite under sintering*. Journal of Materials Science, 2004. 39(16-17): p. 5325-5331.
- [88] Hwan-tae Kim, M.K.a.M.T., *Specimen Temperature and Sintability of Ni Powder by Spark Plasma Sintering*. Journal of the Japan Society of Powder and Powder Metallurgy, 2000. 47: p. 887.
- [89] Tamari, N., et al., *EFFECT OF SPARK PLASMA SINTERING ON DENSIFICATION AND MECHANICAL-PROPERTIES OF SILICON-CARBIDE*. Journal of the Ceramic Society of Japan, 1995. 103(7): p. 740-742.
- [90] David Brandon, W.D.K., *Microstructural Characterization of Materials, 2nd Edition* 2008.
- [91] Williamson, G.K. and R.E. Smallman, *DISLOCATION DENSITIES IN SOME ANNEALED AND COLD-WORKED METALS FROM MEASUREMENTS ON THE X-RAY DEBYE-SCHERRER SPECTRUM*. Philosophical Magazine, 1956. 1(1): p. 34-46.
- [92] B.D.Culity, *Elements of x-ray diffraction*. 2nd ed 1978: Addison-Wesley Publishing Company Inc.
- [93] Ungar, T., *Micro structural parameters from X-ray diffraction peak broadening*. Scripta Materialia, 2004. 51(8): p. 777-781.
- [94] Wilfinger, K.R., W.R. Cannon, and T. Tsakalakos, *RMS MATRIX STRAINS IN TRANSFORMATION TOUGHENED ALUMINA*. Journal of Materials Science, 1990. 25(10): p. 4401-4404.
- [95] Williamson, G.K. and W.H. Hall, *X-RAY LINE BROADENING FROM FILED ALUMINIUM AND WOLFRAM*. Acta Metallurgica, 1953. 1(1): p. 22-31.
- [96] *The International Centre for Diffraction Data*. Available from: <http://www.icdd.com/>.
- [97] Cammarota, G.P. and A. Casagrande, *Effect of ternary additions of iron on microstructure and microhardness of the intermetallic NiAl in reactive sintering*. Journal of Alloys and Compounds, 2004. 381(1-2): p. 208-214.
- [98] Moshksar, M.M. and M. Mirzaee, *Formation of NiAl intermetallic by gradual and explosive exothermic reaction mechanism during ball milling*. Intermetallics, 2004. 12(12): p. 1361-1366.
- [99] Volpp, T., et al., *Grain size determination and limits to Hall-Petch behavior in nanocrystalline NiAl powders*. Nanostructured Materials, 1997. 8(7): p. 855-865.
- [100] Zhang, C.L., et al., *First-principles study of the mechanical properties of NiAl*

- microalloyed by M (Y, Zr, Nb, Mo, Tc, Ru, Rh, Pd, Ag, Cd)*. Journal of Physics D-Applied Physics, 2008. 41(9): p. 5.
- [101] Evekhardt, T.E., O.O. Wells, and C.W. Oatley, *Factors Affecting Contrast and Resolution in the Scanning Electron Microscope†*. Journal of Electronics and Control, 1959. 7(2): p. 97-111.
 - [102] David B. Williams, C.B.C., *Transmission Electron Microscopy: A Textbook for Materials Science* 2009: Springer.
 - [103] Brent Fultz, J.H., *Transmission Electron Microscopy and Diffractometry of Materials* 2009: Springer.
 - [104] Miller, M.K. and E.A. Kenik, *Atom probe tomography: A technique for nanoscale characterization*. Microscopy and Microanalysis, 2004. 10(3): p. 336-341.
 - [105] M.K. Miller, *ATOM PROBE TOMOGRAPHY book chapter*. Handbook of Microscopy for Nanotechnology, 2005. 2005, I., 227-246, DOI: 10.1007/1-4020-8006-9_8.
 - [106] Group, F.A.P.; Available from: <http://www-fim.materials.ox.ac.uk>.
 - [107] Y. Wu, N.J.C., A. Etienne, E. Haney, G. R. Odette, E. Stergar, D. T. Hoelzer, Y.D. Kim, B. D. Wirth and S. A. Maloy, *The Effect of Bulk Oxygen Concentration on the Micro-nanostructure and Strength of a 14Cr Nanostructured Ferritic Alloy*, 2011.
 - [108] Muramatsu, Y., et al., *Gas contamination due to milling atmospheres of mechanical alloying and its effect on impact strength*. Materials Transactions, 2005. 46(3): p. 681-686.
 - [109] Klimiankou, M., R. Lindau, and A. Moslang, *Energy-filtered TEM imaging and EELS study of ODS particles and argon-filled cavities in ferritic-martensitic steels*. Micron, 2005. 36(1): p. 1-8.
 - [110] Chen, Y.L., A.R. Jones, and U. Miller, *Origin of porosity in oxide-dispersion-strengthened alloys produced by mechanical alloying*. Metallurgical and Materials Transactions a-Physical Metallurgy and Materials Science, 2002. 33(8): p. 2713-2718.
 - [111] Herrick, R.S., et al., *DISLOCATION PARTICLE INTERACTIONS IN AN OXIDE DISPERSION STRENGTHENED ALLOY*. Scripta Metallurgica, 1988. 22(12): p. 1879-1884.
 - [112] Hertzberg, R.W., *Deformation and Fracture Mechanics of Engineering Materials Book*. 4th ed 1995.
 - [113] Brailsford, A.D. and P. Wynblatt, *The dependence of oswald ripening kinetics on particle volume fraction*. Acta Metallurgica, 1979. 27(3): p. 489-497.
 - [114] Furukawa, M., et al., *Microhardness measurements and the Hall-Petch relationship in an Al-Mg alloy with submicrometer grain size*. Acta Materialia, 1996. 44(11): p. 4619-4629.
 - [115] Valiev, R.Z., et al., *The Hall-Petch relation in submicro-grained Al-1.5% Mg alloy*. Scripta Metallurgica Et Materialia, 1992. 27(7): p. 855-860.
 - [116] Bowman, R.R., et al., *CORRELATION OF DEFORMATION MECHANISMS WITH THE TENSILE AND COMPRESSIVE BEHAVIOR OF NIAL AND NIAL(ZR) INTERMETALLIC ALLOYS*. Metallurgical Transactions a-Physical Metallurgy and Materials Science, 1992. 23(5): p. 1493-1508.
 - [117] Srinivasan, D., R. Corderman, and R. Subramanian, *Strengthening mechanisms*

- (via hardness analysis) in nanocrystalline NiCr with nanoscaled Y₂O₃ and Al₂O₃ dispersoids. *Materials Science and Engineering a-Structural Materials Properties Microstructure and Processing*, 2006. 416(1-2): p. 211-218.
- [118] William D. Callister, J., *Materials Science and Engineering*. 7th ed 2007.
- [119] CDONNELL, G.F.H.a.B.R.M., *Diffusion in the Intermetallic Compound NiAl*. *phys. stat. sol. (a)* 4, 143 (1971), 1971.